Noname manuscript No.
(will be inserted by the editor)

Auroral processes at the giant planets: energy deposition, emission mechanisms, morphology and spectra

Sarah V. Badman · Graziella Branduardi-Raymont · Marina Galand · Sébastien L.G. Hess · Norbert Krupp · Laurent Lamy · Henrik Melin · Chihiro Tao

Received: date / Accepted: date

S.V. Badman
University of Leicester, UK
Present address: Lancaster University, UK
E-mail: s.badman@lancaster.ac.uk

G. Branduardi-Raymont
UCL/MSSL, UK

M. Galand
Imperial College London, UK

S.L.G. Hess
LATMOS, France

N. Krupp
MPIS, Germany

L. Lamy
Observatoire de Paris, France

H. Melin
University of Leicester, UK

C. Tao
LPP, France
Present address: IRAP, France

Contents

Abstract The ionospheric response to auroral precipitation at the giant planets is reviewed, using models and observations. The emission processes for aurorae at radio, infrared, visible, ultraviolet, and X-ray wavelengths are described, and exemplified using ground- and space-based observations. Comparisons between the emissions at different wavelengths are made, where possible, and interpreted in terms of precipitating particle characteristics or atmospheric conditions. Finally, the spatial distributions and dynamics of the various components of the aurorae (moon footprints, low-latitude, main oval, polar) are related to magnetospheric processes and boundaries, using theory, in situ, and remote observations, with the aim of distinguishing between those related to internally-driven dynamics, and those related to the solar wind interaction.

1 Introduction: Key magnetospheric regions and interactions

The magnetospheres of the outer planets are huge plasma laboratories in space. They are driven by the fast rotation of the planet with its strong internal magnetic field, combined with powerful internal plasma sources (the satellites Io and Europa in the case of Jupiter, and Enceladus at Saturn). Several comprehensive reviews of outer planet magnetospheres and their dynamics have been published (e.g. Dessler 1983; Bagenal et al. 2004; Dougherty et al. 2009) and in this introductory section we only briefly overview the key magnetospheric regions and their dynamics, before describing in detail in the subsequent sections the auroral emissions generated at different wavelengths, and how they are utilised to diagnose the magnetospheric dynamics.

1.1 Jupiter

Our knowledge of the global configuration and dynamics of the Jovian magnetosphere is based on measurements taken onboard spacecraft flying through the Jovian system (Pioneer 10 and 11, Voyager 1 and 2, Ulysses, Cassini, New Horizons) and especially from results of the orbiting spacecraft Galileo.

Figure 1 shows a sketch of the key regions and magnetospheric interactions of the Jovian magnetosphere. Traditionally the magnetosphere is subdivided into the inner,

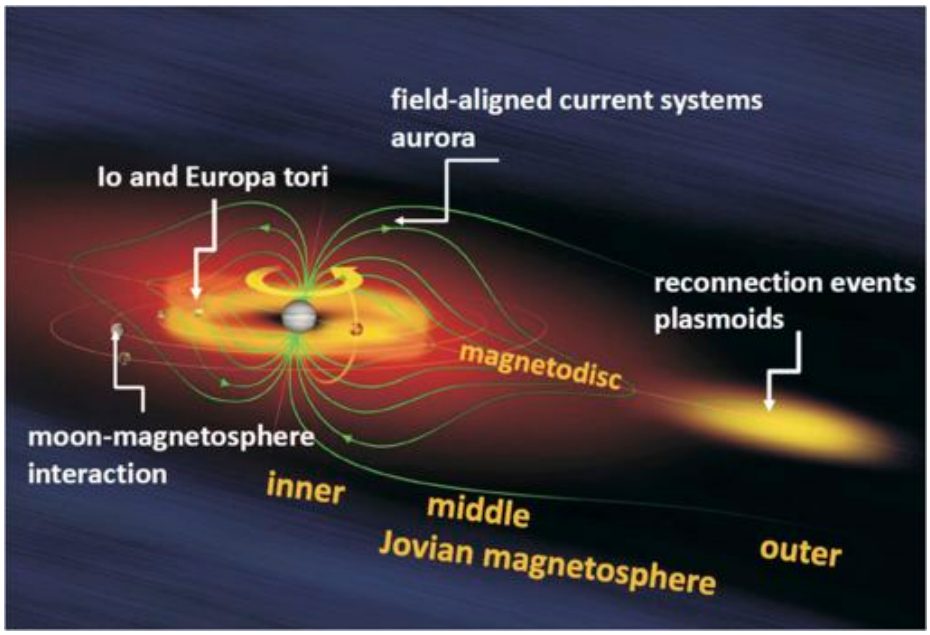

Fig. 1 Sketch of the key magnetospheric regions in the Jovian magnetosphere. Credit: Max Planck Institute for Solar System Research.

middle and outer magnetosphere. In the inner magnetosphere orbits the volcanic moon Io (at 6 R_J radial distance), which is the main source of oxygen and sulphur neutrals in the magnetosphere, and the moon Europa (at 9 R_J radial distance) where hydrogen and possibly oxygen originate. Both moons create a torus along their orbit around the planet in which neutrals are ionized to form plasma tori. While the mass added to the magnetosphere from the moons plays an important role in driving dynamics and auroral emissions throughout the magnetosphere (described below), the moons also have a local interaction with the jovian magnetic field, resulting in auroral footprints at the ionospheric end of the connecting flux tubes. The interaction occurs because the satellites form obstacles to the corotating plasma flow, which is moving faster than their Keplerian orbital velocities. The perturbation of the plasma and field around the moon propagates along the magnetic field as Alfvén waves, interacting with electrons, which finally precipitate into the ionosphere and generate aurora (e.g. Kivelson 2004). At Jupiter the footprints of Io, Europa, and Ganymede have been identified, while the footprint of Callisto is mostly hidden underneath the main oval (Connerney et al. 1993; Clarke et al. 2002). The observed footprints take the form of spots (multiple spots in the cases of Io and Ganymede) and also have trails of enhanced emissions, or 'wakes', behind the footprint itself (e.g. Bonfond et al. 2008; Bonfond et al. 2013).

Due to the centrifugal force of the fast rotating planet, plasma moves radially outward from the tori in the inner magnetosphere. The magnetic field lines frozen in to the plasma in the middle magnetosphere are therefore continuously stretched outward near the equator and deviate significantly from a dipole configuration. Oppositely-directed field lines come close together, and a stable configuration can only be reached through formation of a current sheet between the oppositely-directed fields, and an

associated plasmasheet. An equatorially confined magnetodisc is formed, which wobbles up and down with respect to the equator due to the 9.6° tilt between Jupiter's magnetic dipole axis and the planetary rotation axis. The magnetodisc is relatively thin in the dawn sector (2 R_J half thickness) and thicker on the dusk side (7.6 R_J half thickness) (Khurana et al. 2004).

As the plasma moves outward through the magnetosphere, it also slows. This means that the magnetic field frozen in to the plasma in the magnetodisk is sub-corotating, yet these field lines have their ends fixed in the ionosphere, where collisions between atmospheric neutrals rotating with the planet and ions can occur. The planet therefore supplies angular momentum to the magnetosphere, attempting to spin the field and plasma back up to corotation. The angular momentum is transferred by a field aligned current system, which is directed upward from the ionosphere, radially outward in the equatorial middle magnetosphere (such that the $\mathbf{j} \times \mathbf{B}$ force acts in the direction of planetary rotation), returning downward to the ionosphere at higher latitudes, and closing through an equatorward ionospheric current. The portion of the current directed upward from the ionosphere, carried by down-going electrons, is responsible for Jupiter's main auroral oval (Cowley and Bunce 2001; Hill 2001).

The radial distance where the plasma begins to depart from rigid corotation, i.e. where the ionosphere can no longer impart sufficient angular momentum, seems to be dependent on local time. It is further out in the pre-dawn sector, at 40 R_J, compared to 20–25 R_J in the dusk sector, which may be related to the distribution of mass-loading and loss in the magnetosphere (Vasyliunas 1983; Krupp et al. 2001; Woch et al. 2004). Therefore, while Jupiter's main emission is relatively stable over time, its intensity and location can be affected by the location and magnitude of corotation breakdown in the magnetosphere, which in turn can be affected by, e.g. volcanic activity at Io or solar wind compression of the magnetosphere. These processes are discussed in more detail in Section 3.1.

In the outer magnetosphere the field lines are stretched and sub-corotating. When the current sheet becomes particularly thin, reconnection can occur between oppositely-directed field lines. This ultimately results in the release of a plasmoid downtail and the contraction of the newly-reconnected field line back toward the planet. Reconnection in the magnetotail could occur only on closed, stretched field lines, or continue onto open, lobe field lines (Vasyliunas 1983; Cowley et al. 2003). In situ measurements show that reconnection preferentially occurs at radial distances of 60–80 R_J and its signatures are sometimes observed with a periodicity of 2–3 days (Krupp et al. 1998; Woch et al. 1998; Louarn et al. 1998; McComas and Bagenal 2007; Hill et al. 2009; Vogt et al. 2010). One possible scenario to explain the periodicity, involving a cycle of mass loading and unloading, was first pointed out by Krupp et al. (1998) and Woch et al. (1998). They suggested that, after reconnection, the emptied field lines take approximately a day to snap back radially inwards towards the planet, and azimuthally in the direction of planetary rotation, before the mass-loading cycle starts again. The field lines moving radially inward after reconnection can have auroral signatures in the ionosphere, poleward of the main oval, related to field-aligned currents linking the dipolarised field line to the ionosphere (Grodent et al. 2004; Kasahara et al. 2011).

Even though the solar wind interaction at Jupiter does not play the most important role in terms of dynamics, compared to rotationally-driven dynamics, evidence of solar wind driving and auroral signatures have been identified in the high latitude and outermost regions (see Section 6.1). Currently two basic scenarios are discussed: i) an open magnetosphere where magnetic flux opened during reconnection at the dayside

magnetopause is transported across the the polar region into the magnetotail with a return planetward flow on the dawnside of the tail (Cowley et al. 2003; Badman and Cowley 2007), and ii) a magnetosphere where magnetic flux is opened and closed intermittently in small-scale structures on the flanks of the magnetosphere, via a viscous interaction between heavy, dense plasma inside the magnetosphere and light, tenuous plasma in the solar wind, with a velocity shear between them (Delamere and Bagenal 2010). Support for a solar wind interaction at Jupiter is also reported in MHD simulations by Fukazawa et al. (2010), where periodic plasmoid releases are present in the simulation only occur if the solar wind dynamic pressure is low enough. Corresponding auroral signatures of magnetopause reconnection and an open field region have been identified at Jupiter (e.g. Pallier and Prangé 2001; Cowley et al. 2003), but some mysteries remain, including the origin of dynamic, transient emissions seen in both the UV and IR 'bright polar region', which is thought to map to open, and thus plasma-depleted, field lines.

1.2 Saturn

Saturn's magnetosphere has been visited by the flyby missions Pioneer 11, Voyager 1 and 2, and by Cassini as the first orbiting spacecraft around the ringed planet. Fig. 2 shows a sketch of Saturn's magnetosphere, indicating the key magnetospheric regions and plasma populations.

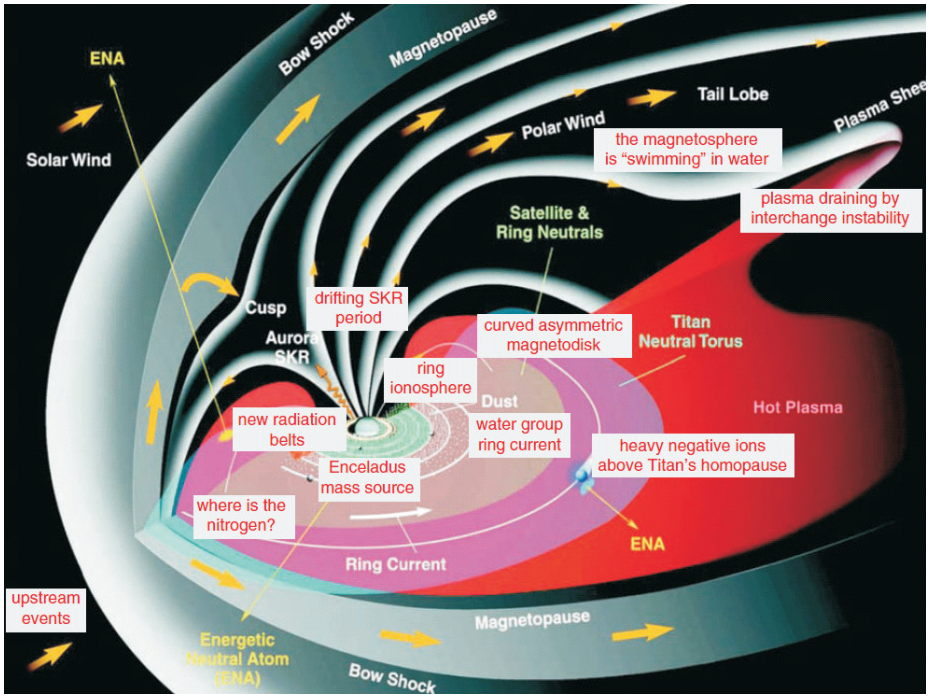

Fig. 2 Sketch of the key magnetospheric regions and plasma populations in the kronian magnetosphere (from Gombosi et al. (2009)).

Saturn also has major sources of neutrals inside the magnetosphere, primarily the moon Enceladus, which releases water ice and dust grains into the kronian magnetosphere through active geysers in the southern polar region, at a rate of up to a few hundred kg s^{-1} (e.g. Hansen et al. 2006). Like the Io-Jupiter interaction, Dougherty et al. (2006) showed that when some of this water is ionised near Enceladus, it perturbs the magnetic field, resulting in a field-aligned current linking the near-moon environment to Saturn's ionosphere. The associated auroral spot has been identified in a few UV images of Saturn's northern ionosphere (Pryor et al. 2011). Titan, orbiting at ~ 20 R_S, was previously thought to be a significant particle source, especially for nitrogen, but has been revealed to be only a minor plasma source for the magnetosphere by Cassini measurements (Smith et al. 2007).

Saturn's magnetosphere is also rotation-dominated and forms an equatorially-stretched asymmetric magnetodisc. Plasma is observed to sub-corotate throughout Saturn's magnetosphere (Wilson et al. 2009; Thomsen et al. 2010), and a relatively faint auroral arc has been identified in the infrared observations of the conjugate latitudes in the ionosphere as the signature of corotation-enforcement currents (Stallard et al. 2010). The main auroral emission lies at higher latitudes, and is driven by field-aligned currents associated with the flow shear between anti-sunward, open and outer magnetospheric field lines, and sub-corotating middle magnetosphere field lines (Cowley et al. 2005; Bunce et al. 2008). Transport processes like interchange motion and injection events are continuously present in the kronian magnetosphere, showing the highly dynamic nature of Saturn's magnetosphere (Mitchell et al. 2009b). Observational studies have linked diffuse auroral enhancements, equatorward of the main oval, with injection or particle scattering events in the magnetodisc (Radioti et al. 2009, 2013b; Grodent et al. 2010).

The kronian magnetosphere is overall rotationally-dominated, however, solar wind parameters do play a role in its dynamics (Mauk et al. 2009). One example is the fact that solar wind compression regions can trigger injection events in the nightside of the kronian magnetosphere, which are observed in particle and auroral data (Clarke et al. 2005; Bunce et al. 2005; Mitchell et al. 2009a). Reconnection events, dipolarisations, and ejected plasmoids have also been identified in Saturn's magnetosphere (Jackman et al. 2011, 2013), but were not found to occur quasi-periodically as in the case of Jupiter. Again, the most poleward auroral emissions seem to reflect these events, indicating their occurrence in the outer magnetosphere (Clarke et al. 2005; Grodent et al. 2005; Jackman et al. 2013).

In the sections below we describe in detail how particles originating in the magnetosphere and solar wind impact on the atmosphere and cause auroral emissions at different wavelengths, and how these emissions can reveal the magnetospheric dynamics, including differences between magnetodisk- and solar wind-driven events.

2 Response of the ionosphere to auroral forcing at the giant planets

Particles, momentum and energy are exchanged between the planetary upper atmosphere and magnetosphere via the ionosphere in the high latitude regions. There is a net momentum transferred from the atmosphere to the magnetosphere, while energy through, for instance particle precipitation, is deposited from the magnetosphere to the atmosphere (e.g. Hill 1979, 2001; Cowley and Bunce 2001). These particles primar-

ily originate from moons (e.g., Io and Europa at Jupiter, and Enceladus at Saturn), and to a lesser extent from the planetary atmosphere and the solar wind (e.g., polar regions at Jupiter). Some of the ions resulting from ionization of the moon's gas torus are neutralized through charge exchange and leave the system; the others are picked up by the planetary magnetic field closely rotating at the planet's rotation rate and flow outward through the planetary magnetosphere (Bagenal and Delamere 2011). The resulting upward currents, flowing from the atmosphere to the magnetosphere, that supply the required angular momentum accelerate the particles, increasing their energy and energy flux (e.g. Ray et al. 2010, 2012b). Particles can also precipitate as a result of wave-particle interactions (e.g. Radioti et al. 2009).

When the energized particles reach the high latitude upper atmosphere, they collide with the atmospheric species, depositing energy through ionization, excitation and dissociation of the neutral gas. This yields the so-called 'auroral emissions' defined as the photo-manifestation of the interaction of energetic, extra-atmospheric particles with an atmosphere (e.g. Bhardwaj and Gladstone 2000; Galand and Chakrabarti 2002; Fox et al. 2008; Slanger et al. 2008). Auroral particle degradation results in an increase in ionospheric densities and electrical conductances (e.g. Millward et al. 2002; Hiraki and Tao 2008; Galand et al. 2011). Ionospheric currents, which allow closure of the magnetospheric current system, are enhanced and induce strong Joule heating of the high-latitude thermosphere (e.g. Miller et al. 2005; Smith et al. 2005; Müller-Wodarg et al. 2012). This high-latitude atmospheric heating is a key player in the energy crisis at the giant planets (e.g. Yelle and Miller 2004). In other words, particle precipitation, which can be traced via auroral emissions, plays a critical role in the thermosphere-ionosphere system and its coupling to the magnetosphere.

2.1 Energy deposition of precipitating auroral particles

2.1.1 Energetic electrons

The incident auroral electron characteristics derived from the spectroscopic analysis of the ultraviolet auroral emissions (see Section 3.1.1) are summarized in Table 1 for the main auroral ovals of Jupiter and Saturn.

2.1.1.1 Models of suprathermal electron transport Auroral, energetic electrons interact with the atmospheric neutrals through elastic scattering and inelastic collisions, the latter including ionization, excitation, dissociation or a combination of them. Ionization yields the production of secondary electrons, which can in their turn interact with the atmosphere. Furthermore, suprathermal electrons interact with the thermal, ionospheric electrons through Coulomb collisions. This yields an increase in the ionospheric electron temperature (e.g. Grodent et al. 2001; Galand et al. 2011).

As a result of the interaction with the atmospheric species, the suprathermal electrons undergo degradation in energy and redistribution in pitch angle, defined as the angle between the electron velocity and the local magnetic field. As the energy loss is a function of the electron energy, and secondary electrons are added towards lower energies, the initial electron energy distribution at the top of the atmosphere changes, as the electrons penetrate deeper in the atmosphere. The calculation of the distribution of electrons in both position and velocity space is required. Three approaches have been

Table 1 Characteristics of the mean energy and energy flux of the auroral electrons incident at the top of the atmosphere over the main auroral ovals of Jupiter and Saturn. These characteristics have been derived from recent analyses of ultraviolet auroral emissions.

Mean electron energy E_{prec} (keV)	Electron energy flux Q_{prec} (mW m^{-2})	Reference
	JUPITER	
30–200 Typically, 75	2–30	Gustin et al. (2004a)
.01 –3 (soft) 15–22 (hard)	-	Ajello et al. (2005)
460 (dawn storm)	90 (dawn storm)	Gustin et al. (2006)
	SATURN	
-	1.9–3.2 (dawn), 4.2–7.7 (pre-noon), 0.3–1.5 (afternoon), <0.4 (dusk), 0.3–0.8 (pre-midnight)	Cowley et al. (2004b)
12±3	7.5 (pre-noon max), 5 (midnight)	Gérard et al. (2004)
1–5, 5–30[a]	-	Gérard et al. (2009)
13–18 (STIS); 10 (Cassini/UVIS/FUV); <15 (FUSE)	0.3–1.4 (STIS)[b]	Gustin et al. (2009)
Typically 10	Typically 1	
-	0.9	Gustin et al. (2012)
≤ 21	-	Gérard et al. (2013)
10–20 (Cassini/UVIS)	$\leq 1-17$	Lamy et al. (2013)

[a] The two sets of values correspond to two different atmospheric models used for the analysis. The energy values quoted correspond to the characteristics energy, which is equal to half the mean energy if the energy distribution is assumed to be Maxwellian. An energy range of 0.3–2 is quoted in Table 1 of Gérard et al. (2013) for the analysis of Gérard et al. (2009), which most likely is a typo error.
[b] Applying a 10 kR – 1mW m^{-2} conversion factor to the total auroral brightness in the H_2 Lyman and Werner bands (e.g., Gustin et al. (2012)).

applied to auroral electrons at Jupiter and Saturn, all assuming steady-state conditions and the guiding center approximation (Rees 1989):

– The 'Continuous Slowing Down Approximation' (CSDA) method assumes that the energy loss is a continuous rather than a discrete process (Gérard and Singh 1982; Singhal et al. 1992; Rego et al. 1994; Prangé et al. 1995; Dalgarno et al. 1999). The variation dE in electron energy per path length ds in an atmosphere composed of species k with neutral density n_k and energy loss L_k is given by:

$$\frac{dE}{ds} = -\Sigma_k n_k(s) L_k(E) \quad (1)$$

The method, simple to implement, requires - in order to be able to integrate Equation 1 - that either the atmospheric composition is independent of altitude (e.g., Dalgarno et al. (1999)) or that atmospheric species have energy losses proportional to each other (e.g., Rego et al. (1994)). The method is limited to high energies where the assumption of a continuous loss is justified and scattering is neglected.

The CSDA method allows the calculation of the profiles in altitude of ionization and excitation rates.

– An alternative method is to utilise transport models based on the explicit, direct solution of the Boltzmann equation, which can use a two-stream approach (up/down) (Waite 1981; Waite et al. 1983; Achilleos et al. 1998; Grodent et al. 2001; Gustin et al. 2009) or multi-stream approach (more than two pitch angles considered) (Kim et al. 1992; Perry et al. 1999; Menager et al. 2010; Galand et al. 2011). The Boltzmann equation expresses the conservation of the number of particles in the phase space, as given by:

$$\frac{df}{dt} + f\nabla_{\underline{v}}.\frac{\underline{F}}{m} = \left(\frac{\delta f}{\delta t}\right)_{coll} + S_{ext} \tag{2}$$

where $f(\underline{r}, \underline{v}, t)$ is the suprathermal electron distribution at position $\underline{r}$, velocity $\underline{v}$ and time t. The second term on the LHS takes into account the effect of any dissipative forces $\underline{F}$. The first term on the RHS represents variation due to collisions and the second term is associated with external sources (e.g., photoelectrons, secondary electrons from an ion beam).
The Boltzmann equation is solved in terms of the suprathermal electron intensity ($I_e = \frac{v^2}{m} f$), which is a measurable quantity. The phase space is usually reduced to three dimensions, path length s along the magnetic field line, kinetic energy E, and cosine μ of the pitch angle θ. Scattering is included. Beside ionization, excitation, and dissociation rates this method allows the calculation of thermal electron heating rates.

– Monte Carlo simulations refer to a stochastic method based on the collision-by-collision algorithm (Hiraki and Tao (2008); Gérard et al. (2009); Tao et al. (2011)). A large number of particles is considered and followed in the simulated atmosphere. The Monte Carlo approach avoids the use of an energy grid, which can be of great interest for problems with electron energies ranging over five orders of magnitude. Its drawback is that it is computationally expensive, since it requires a large number of particles to reduce the statistical noise. At Jupiter and Saturn, only excitation, ionization and dissociation processes have been included; thermal electron heating, which is efficient at low energies (< 1 eV), has not been considered.

Suprathermal electron transport models are driven by the electron intensity at the top of the atmosphere, which is a function of energy and pitch angle. The energy distribution is usually assumed to be Maxwellian (or a combination of several), Gaussian or monoenergetic, though any distribution can be considered. The initial pitch angle distribution is often assumed to be isotropic over the downward hemisphere or field-aligned. Prangé et al. (1995) showed that anisotropy affects the excitation rates and color ratios. Nevertheless, the effect is attenuated when elastic scattering is included (Hiraki and Tao 2008). Anisotropy does not affect significantly the H Ly α spectral profile (Menager et al. 2010). When defining the incident distribution, the energy flux Q_{prec} should be defined over the downward hemisphere, as follows:

$$Q_{prec} = 2\pi \int_{E_{min}}^{E_{max}} dE.\, E \int_0^1 d\mu.\, \mu.\, I_e^{prec}(E, \mu) \tag{3}$$

where $I_e^{prec}(E, \mu)$ is the intensity of the incident electrons. Depending on the magnetic field orientation, the integration over angle can be from 0 to 1, or from 0 to -1 (0 and (-1) wrongly switched in eq. (1) of Galand et al. (2011)). For an isotropic beam,

Equation 3 is reduced to: $Q_{prec} = \pi \int_{E_{min}}^{E_{max}} dE.\, E.\, I_e^{prec}(E)$, while for a field-aligned beam, Equation 3 is two times larger.

Validation of these models at Jupiter and Saturn is performed by ensuring particle and energy conservation. Models have been compared in terms of atmospheric column above the maximum energy deposition altitude (Galand et al. 2011) and of electron production rate (see Section 2.1.1.2). The former shows a 20% agreement between the results of Gustin et al. (2009) and those of Galand et al. (2011) for a pure H_2 atmosphere except around 20 keV. This anomaly has not yet been explained. There is no apparent reason for a sharp change around 20 keV, as seen in the work by Gustin et al. (2009).

Most of the auroral electron energy is lost through collisions with neutrals and about 50% of the total energy input is used to heat the atmosphere (Grodent et al. 2001). The percentage of energy lost through collisions with neutrals increases with the electron energy (Menager et al. 2010; Galand et al. 2011). At Saturn, for 10 keV electrons, 89% of the energy is lost that way with the remaining transferred to thermal electrons (7%) or escaping as a result of collisional scattering (4%). Among the energy lost with neutrals, more than 90% is lost through collisions with H_2 including 50% used for ionizing H_2 and producing H_2^+ (Galand et al. 2011). In addition to auroral emissions produced by the excitation of atmospheric species from the UV to the IR (see Section 3), suprathermal electrons produce Bremstrahlung emissions themselves in the hard X-ray range, as detected in the auroral zones of Jupiter (see Section 4).

2.1.1.2 Electron production rate The electron production rate $P_e(z)$ induced by auroral electrons is derived from the suprathermal electron intensity $I_e(z, E, \mu)$ calculated as a function of altitude z, energy E, and pitch angle μ (see Section 2.1.1.1), as follows:

$$P_e(z) = 2\pi \sum_k n_k(z) \int_{-1}^{1} d\mu \int_{E_{th}}^{E_{max}} dE\, \sigma_k^{ioni}(E) I_e(z, E, \mu) \tag{4}$$

where $n_k(z)$ is the number density of the neutral species k at altitude z and $\sigma_k^{ioni}(E)$ is the total ionization cross section of the neutral species k by electrons of energy E. E_{th} represents the ionization threshold of a single, non-dissociative ionization. Double ionization is not considered here. Volume excitation rates can be calculated in a way similar to Equation 4 except that the ionization cross section is replaced by the excitation cross section. Under solar illumination, photo-ionisation by EUV solar radiation (0.1–100 nm) and electron-impact ionization by photoelectrons and their secondaries (e.g. Kim and Fox 1991; Galand et al. 2009; Menager et al. 2010) occurs.

The electron production rate is proportional to the energy flux Q_{prec} of the incident electrons. The altitude of the peak production decreases with the initial energy of the energetic electrons. The more energetic an electron is, the more collisions are required to have it thermalized. A comparison between electron production rates derived from different models using a triple Maxwellian energy distribution for the incident electrons is shown in Figure 3. There is a very good agreement between the profiles obtained by Grodent et al. (2001) (thick, solid line) and Galand et al. (2011) (dashed line) with less than 7% difference at the peak. There are large differences above the peak altitude between these two profiles and the one by Hiraki and Tao (2008) (dash-dotted line). The reason is most likely due to different altitude profiles used for the thermospheric densities. In Grodent et al. (2001) the neutral density profiles are given

as a function of pressure. A pressure-altitude conversion is required in order to calculate the auroral electron transport on an altitude grid. Galand et al. (2011) derived a conversion between these two quantities assuming hydrostatic equilibrium and using the temperature profile given in Grodent et al. (2001). Hiraki and Tao (2008) used a different altitude-pressure conversion and derived the profile in altitude for Grodent et al. (2001) shown as the thin, solid line in Figure 3. The profile derived by Menager et al. (2010) (dotted line in Figure 3) agrees overall with the profile by Grodent et al. (2001) (thick, solid line) except around 1000 km, and near the peak by a factor larger than 2. It is not clear what the source of discrepancy is.

Hiraki and Tao (2008) successfully compared their electron production profile with the one derived by Rego et al. (1994) for 10 keV electrons. Menager et al. (2010) compared their ion production rates at the peak against those presented by Perry et al. (1999). They found 10% difference for electrons, but larger differences for H^+ (produced from H_2) and hydrocarbon ions.

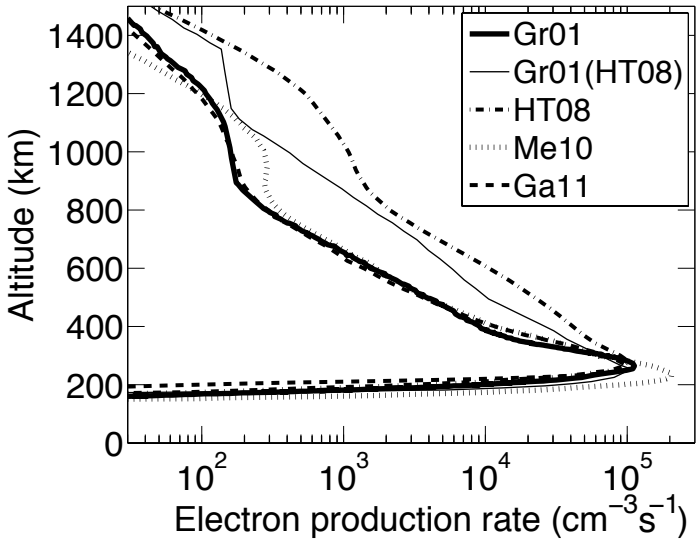

Fig. 3 Comparison of the profile in altitude of the electron production rate at Jupiter between the models of Grodent et al. (2001) [Gr01], Hiraki and Tao (2008) [HT08], Menager et al. (2010) [Me10] and Galand et al. (2011) [Ga11]. The incident electron energy distribution is a triple Maxwellian applied to discrete aurora as defined by Grodent et al. (2001). The thin line annotated Gr01(HT08) corresponds to the electron production rate profile for Grodent et al. (2001) shown in Hiraki and Tao (2008). The reference altitude is taken at the 1-bar level.

2.1.2 Energetic ions

2.1.2.1 Models of suprathermal ion transport Beside protons of planetary or solar origin (e.g. Patterson et al. 2001), sulfur ions from Io's torus and/or oxygen ions from the icy moons (e.g., Europa, Enceladus) are also present in Jupiter's and Saturn's magnetospheres (Lanzerotti et al. 1992; Bagenal and Delamere 2011). Like for electrons, suprathermal ions collide with atmospheric neutrals yielding scattering, ionization,

excitation, and dissociation (or a combination of them). The secondary electrons produced through particle-impact ionization can have enough energy to interact in their turn with atmospheric species. Each type of ion species interacts differently with the atmosphere. For instance, an incident proton beam loses most of its energy through ionization, while an incident oxygen beam does not lose more than 50% in ionization (Ishimoto and Torr 1987).

The energy degradation of ions is complicated by charge-changing reactions. For example, an energetic proton can capture an electron and become an energetic H atom. In its turn, this H atom can interact with the atmospheric species and/or get stripped of its electron and become a proton again:

$$\begin{array}{rl} H^+ + H_2 \rightarrow H + H_2^+ & \text{Capture} \\ H + H_2 \rightarrow H^+ + H_2 + e^- & \text{Stripping} \end{array} \quad (5)$$

Therefore, unlike the case of electrons, more than one charge state needs to be considered: 2 in the case of an incident proton beam (e.g., 0 for H, 1 for H^+); many more in the case of oxygen with stripping collisions potentially producing high charge state ions (e.g., O^{7+} and O^{8+}) (Cravens and Ozak 2012). Furthermore, another complication occurs when a significant part of the incident ion beam is neutralized. As neutral species are not affected by the magnetic field, the neutral beam spreads spatially (in particular latitudinally), which may result in an attenuation of the ion intensity at the centre of the beam (e.g. Lorentzen 2000).

Beside exciting atmospheric neutrals resulting in auroral emissions similar to those produced by electron-induced aurora, ion precipitations have unique signatures distinct from electron precipitations, when the excited species is the energetic ion (or neutral) species itself. For instance, soft X-ray, K-shell emission provides the main evidence that acceleration and precipitation of energetic heavy ions - with energies larger than MeVs - are taking place on Jupiter (Cravens and Ozak 2012); see also Section 4). Doppler-shifted H emissions produced by energetic H atoms are a signature of proton precipitation. While in the N_2-dominated terrestrial atmosphere, such a signature is easily detectable (e.g. Galand and Chakrabarti 2006), it is not the case in an H_2-dominated atmosphere. Suprathermal particles induce strong H emissions with photons undergoing frequency shift. This results in a wide spectral profile around H lines (Prangé et al. 1995; Rego et al. 1999). So far no unambiguous detection of a Doppler-shifted component emitted by the energetic H atoms has been made in the H Ly α spectral profile, though it has been speculated (Prangé et al. 1995). Model predictions have shown that the contribution of the Doppler-shifted wing is decreasing with increasing energies and is expected to be small for incident MeV protons. Therefore, its non-detection thus far does not mean that auroral protons do not contribute to the UV emissions at Jupiter and Saturn (Rego et al. 1999).

Two of the three types of approaches used for modeling suprathermal electron transport and energy degradation (see Section 2.1.1.1) have been applied to suprathermal ions at Jupiter and Saturn (e.g. Ozak et al. 2010):

– CSDA (e.g. Rego et al. 1994; Cravens et al. 1995; Horanyi et al. 1988). The beam is assumed to be in charge equilibrium, which is not always valid (Rego et al. 1994). For a pure H_2 atmosphere, the equilibrium fractions of H and H^+ at energy E are given by:

$$F_H(E) = \frac{\sigma^{10}_{H_2}(E)}{\sigma^{10}_{H_2}(E)+\sigma^{01}_{H_2}(E)}$$
$$F_{H^+}(E) = \frac{\sigma^{01}_{H_2}(E)}{\sigma^{10}_{H_2}(E)+\sigma^{01}_{H_2}(E)} \quad (6)$$

where $\sigma^{10}_{H_2}(E)$ and $\sigma^{01}_{H_2}(E)$ are the electron capture cross section and the electron stripping cross section for H_2, respectively. As the former becomes increasingly dominant towards lower energies, the fraction F_H of H atoms - given by Equation 6a - increases as well. In a gas mixture, the effective equilibrium fraction F is derived from the sum of the equilibrium fraction of each neutral species weighted by its volume mixing ratio.

– Monte Carlo simulations (e.g. Kharchenko et al. 1998, 2006, 2008; Hui et al. 2009, 2010a). Unlike for CSDA, no assumption is made on the charge state fraction, the particle charge state being recorded after each collision. In addition, the spreading of the beam is computed explicitly (when 3D simulations are carried out), although it is computationally demanding. In additions it requires as input the latitudinal width of the incident ion beam, which is poorly constrained at the Earth and is not known at the giant planets.

2.1.2.2 Comparison between electron and ion energy deposition Comparisons between auroral electrons and protons have been carried out in terms of electron production rates and excitation rates (Rego et al. 1994) and of color ratio and H Ly α spectral profiles (Rego et al. 1999). The probability of collisions with neutral species differs between electrons and protons. As a result, for a given mean energy auroral electrons penetrate deeper in the atmosphere compared with protons. Nevertheless electrons and protons are not expected to have similar energies at the top of the atmosphere. Protons are anticipated to be more energetic, which may compensate for this difference in collision probability.

For a given energy flux, incident 10 keV electrons and 300 keV protons produce very similar volume ionization rate profiles in altitude, as illustrated in Figure 4. They deposit energy at a similar altitude and the ionization rate is the same at the peak. Only at high altitudes do auroral electrons have a higher ionization rate than protons, up to 40% at 2000 km. In addition, for both populations the contribution to ionization from secondary electrons is negligible, representing only 1% of the total ionization. By contrast, the excitation rates depend upon the nature of the precipitating particles. For instance, in a proton beam the secondary electrons are the main contributor to the total excitation of H Ly α, while in an electron beam the contributions from primary and secondary electrons are similar (Rego et al. 1994). The dependence in energy of the color ratio between two H_2 emission bands also varies with the nature of the particles. For a given mean energy, electrons penetrate deeper in the atmosphere, which means that the spectral band around 160 nm, which suffers from hydrocarbon absorption, undergoes stronger attenuation than in the case of protons (Rego et al. 1999). Color ratios inform on the altitude of deposition with similar values found for particles depositing their energy at the same altitude. Caution needs to be applied when deriving the initial energy of the particles (see Section 3.1.1). As soft electrons have similar color ratios as hard protons, the presence of protons, even modest, may yield a significant underestimation of the electron mean energy if the incident beam is assumed to be pure electrons. A similar effect has been observed in the auroral regions at Earth (Galand and Lummerzheim 2004).

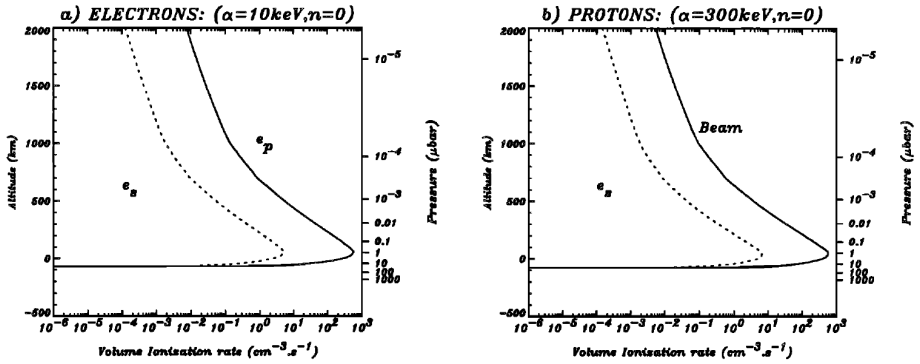

Fig. 4 Profiles in altitude (left axis) and pressure (right axis) of the volume ionization rate - that is, electron production rate profiles, as double ionization is negligible -, due to primary particles (solid line) and secondary electrons (dotted line) in the case of 10 keV electron incident beam (left) and 300 keV proton incident beam. The energy flux of the incident particles is assumed to be the same (From Rego et al. (1994)).

2.2 Ionospheric response to auroral forcing

2.2.1 Electron densities

2.2.1.1 Observations of electron density Profiles in altitude of the electron density are obtained by radio occultations. In this technique the spacecraft is emitting a radio signal which traverses the planetary atmosphere before being received by large radio telescopes on the ground at Earth. As the spacecraft is passing behind the planet as seen from Earth, the signal is refracted by free electrons in the ionosphere. For the outer planets, only measurements at dawn and dusk are possible. The number density of ionospheric electrons is derived from the dimming of the signal. The latest update of the electron density profiles obtained at Jupiter, as measured by Voyager and Galileo and analyzed through a detailed, multi-path technique, is presented by Yelle and Miller (2004) (see Figures 5a and 5b). Most profiles have a peak around 0.5–2$\times 10^{11}$ m^{-3} (or 0.5–2 $\times 10^{5}$ cm^{-3}) at an altitude between 1500 and 2000 km. The Voyager (panel b) and Galileo/0 ingress (G0N) (panel a) profiles with large peak electron densities located at low altitudes occurred at dusk, while Galileo/0 egress (G0X) with a low peak electron density at higher altitudes occurred at dawn. The local-time dependence could be explained by the difference in magnitude and location of the peak (see Section 2.2.1.3 below). However, the Galileo/3 and 4 do not exhibit such a behaviour (Yelle and Miller 2004). The characteristics of the electron density profiles at Jupiter measured mostly at mid-latitudes in the southern hemisphere do not seem to correlate with any obvious geophysical parameters (McConnell et al. 1982; Yelle and Miller 2004).

At Saturn, radio occultations of the ionosphere have provided electron density profiles from Pioneer 11 (Kliore et al. 1980) and the two Voyagers (Lindal et al. 1985), as well as from the Radio Science Sub-System (RSS) onboard Cassini in the near-equatorial regions and at mid- and high latitudes (Nagy et al. 2006; Kliore et al. 2009) (see also (Matcheva and Barrow 2012)). Figure 5c shows average profiles for each of these three regions. Most profiles have peaks between 3×10^2 and 3×10^4cm^{-3}. These values are lower than those at Jupiter, which is located closer to the Sun. The peak

electron density increases with latitude (see Section 2.2.1.4 below). At low latitudes, the peak is found to have higher electron density values at dusk than dawn (see Section 2.2.1.3). No clear dawn-dusk asymmetry is however seen at mid-latitudes (Nagy et al. 2009).

While the overall magnitude of the density profiles is captured by ionospheric models (e.g. Moore et al. 2004, 2006; Galand et al. 2009), gravity waves need to be invoked to explain the highly-structure vertical profiles at Jupiter and Saturn (Barrow and Matcheva 2011; Matcheva and Barrow 2012; Barrow and Matcheva 2013). At low latitudes above the homopause, a surge in water inflow may also contribute to the presence of 'bite-outs' in the profiles observed at Saturn (Moore and Mendillo 2007).

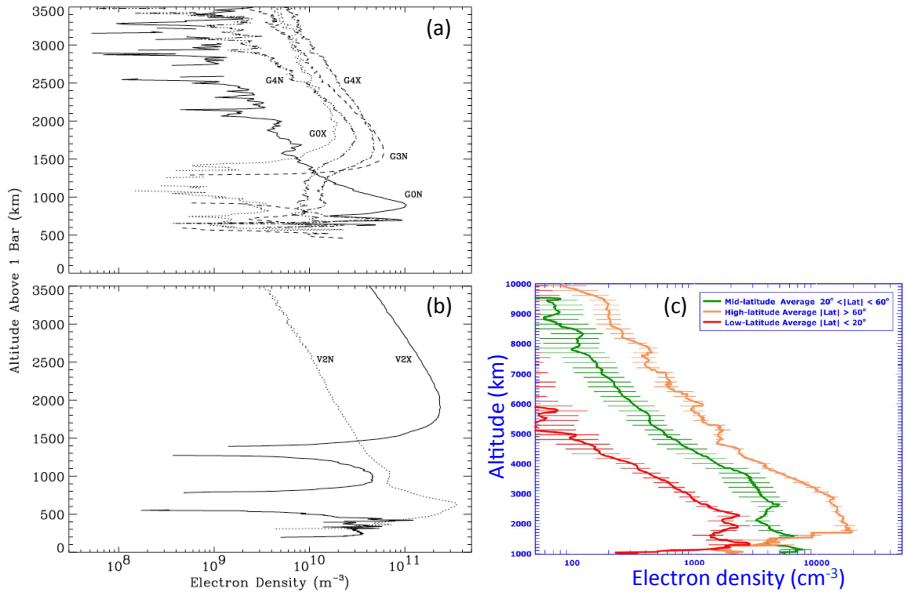

Fig. 5 Left: Electron density profiles in the Jovian ionosphere as measured by Galileo (Panel a, top) over the 23–43°S range and Voyager (Panel b, bottom) over the 50–67°S range (Yelle and Miller 2004). Right (Panel c): Electron density profiles in the Saturn ionosphere, averaged over low- (red), mid- (green) and high- (orange) latitudes from all Cassini occultations (Kliore et al. 2009)

Impulsive radio bursts at Saturn, referred as Saturn Electrostatic Discharges (SEDs), have been detected by the two Voyagers (Warwick et al. 1981, 1982) and the Cassini/Radio and Plasma Wave Science (RPWS) instrument (Gurnett et al. 2005; Fischer et al. 2006, 2007). These discharges are produced by lightning occurring in convective-looking clouds at mid-latitudes (e.g. Dyudina et al. 2010). Peak electron densities are derived from the measurement of the low-frequency cutoff below which the radio waves, which traverse Saturn's ionosphere on their way to the spacecraft, are not detected (Fischer et al. 2011). The diurnal variation of the peak electron density derived from SEDs analysis is discussed in Section 2.2.1.3

At Jupiter, no high frequency radio component - similar to SEDs - above the cutoff frequency of the ionosphere has been detected (e.g. Fischer et al. 2008). This non-

detection has been explained as the result of the strong absorption of the radio waves in Jupiter's lower ionospheric layers (Zarka 1985) and of the decrease of the spectral power of Jovian spherics with increasing frequency (Farrell et al. 1999).

2.2.1.2 Ionospheric models The continuity equation, which expresses the conservation of the number of particles, allows the calculation of the number density of species i:

$$\frac{\partial n_i}{\partial t} + \nabla.\,(n_i \underline{u}_i) = P_i - L_i \tag{7}$$

where $\underline{u}_i$ is the bulk velocity, and P_i and L_i are the production and loss rates, respectively, of species i. XUV solar radiation is the main source of electrons at low and mid latitudes and particle precipitation dominates in the auroral regions. Ions are also produced through chemical reactions, such as charge exchange. Loss rates include ion-neutral reactions and, for molecular ions, ion-electron dissociative recombination (e.g. Kim and Fox 1991; Moses and Bass 2000). Ionospheric models have been developed for the outer planets, as reviewed by Waite et al. (1997) with more recent models proposed for Jupiter (Achilleos et al. 1998; Perry et al. 1999; Grodent et al. 2001; Millward et al. 2002; Tao et al. 2010; Barrow and Matcheva 2011) and Saturn (Moses and Bass 2000; Moore et al. 2004, 2006, 2008, 2010, 2012; Galand et al. 2009, 2011; Tao et al. 2011; Barrow and Matcheva 2013).

The second term in Equation 7 represents transport processes, such as plasma diffusion. It becomes increasingly important with altitude, controlling the upper part of the ionosphere ($\geq$2300 km above the 1 bar level at Saturn (Moore et al. 2004). Neutral winds can also have a significant effect by redistributing the plasma from one region to another. Horizontal winds will move the plasma vertically along the magnetic field lines. Galand et al. (2011) showed that in the auroral regions where the dip angle is large, the main contributor is the vertical component of the thermospheric wind, which decreases the electron density peak magnitude by as much as 75%.

In the lower ionosphere, transport timescales are significantly larger than chemical loss timescales and the photochemical regime dominates. Assuming also steady-state conditions, the continuity equation 7 is thus reduced to:

$$P_i = L_i \tag{8}$$

Under photochemical equilibrium, the H^+ to H_3^+ number density ratio is proportional to the electron density (e.g. Moore et al. 2004). This means that molecular ions will be more abundant at low latitudes where the electron density is reduced compared with high latitudes where it has significantly larger values (see Section 2.2.1.4).

Introducing an effective recombination coefficient $\overline{\alpha}$ defined as the recombination coefficient of individual ion species weighted by their number density, Equation 8 applied to ionospheric electrons becomes:

$$P_e = \overline{\alpha}\; n_e^2 \text{ , that is, } n_e = \sqrt{\frac{P_e}{\overline{\alpha}}} \tag{9}$$

In the absence of (or under limited) solar illumination, P_e is proportional to the energy flux Q_{prec} of the precipitating particles (see Section 2.1.1). Therefore, Equation 9 means that: $n_e \propto (Q_{prec})^{1/2}$ (for constant precipitation over time). This assumes that the photochemical regime dominates, which is fulfilled in the lower ionosphere.

As H and H_2 are the dominant neutral species in this region, H_2^+ and H^+ are the main ions produced through photo-ionization and electron-impact ionization. H_2^+ is

very reactive and quickly interacts with H_2 to become H_3^+. H_3^+ is lost through electron dissociative recombination, which significantly depletes in density during the night (e.g. Kim and Fox 1994, see Section 2.2.1.3).

Early ionospheric models at the giant planets predicted that the long-lived H^+ would be the dominant species and overestimated the peak electron density (McElroy 1973). Loss mechanisms have been introduced in order to match the observed peak electron densities: (1) charge-exchange of H^+ with vibrationally-excited H_2 (e.g. McConnell et al. 1982; Moses and Bass 2000; Moore et al. 2010); (2) forced vertical motion of the plasma (e.g. McConnell et al. 1982; Majeed and McConnell 1991); (3) water inflow especially at Saturn (Connerney and Waite 1984; Majeed and McConnell 1991; Moses and Bass 2000; Moore et al. 2006, see Section 2.2.1.4).

H^+ is efficiently lost when H_2 is in vibrationally-excited levels as follows:

$$H^+ + H_2(\nu \geq 4) \rightarrow H_2^+ + H \tag{10}$$

The reaction rate, k1, for Reaction 10 is now well established with a value of 10^{-9} cm^3 s^{-1} (Krstić 2002; Huestis 2008). In photochemical models usually an effective reaction rate k_1^* is used which is defined as:

$$k_1^* = k_1 \frac{n_{H_2}^{\nu \geq 4}}{n_{H_2}} \tag{11}$$

where n_{H_2} is the total H_2 number density and $n_{H_2}^{\nu \geq 4}$ is the H_2 number density in a vibrationally-excited level $\nu \geq 4$.

Assessing the relative amount of H_2 in vibrational levels of non-LTE origin carries out large uncertainties, which limit the estimate of the electron density (Nagy et al. (2009) and references therein). Estimations have been proposed by Moses and Bass (2000), and more recent updates have been presented by Moore et al. (2010, 2012) in order to best match the Cassini/RSS observations. k_1^* is expected to increase in the auroral regions (e.g. Cravens 1987).

Below the homopause, H^+ efficiently reacts with hydrocarbons (Kim and Fox 1994; Moses and Bass 2000). This loss is twice as fast as that of H_3^+ resulting in the dominance of molecular ions, in particular hydrocarbon and metallic ions, in this region (Moses and Bass 2000; Kim et al. 2001).

2.2.1.3 Diurnal variation Based on radio occultation observations, low-latitude profiles obtained at Saturn exhibit a strong dawn/dusk asymmetry with lower peak electron density observed at dawn, as illustrated in Figure 6a. The presence of water at low latitudes yields a depletion in H^+ and molecular ions become dominant, at least in the late morning up to early afternoon sector (Moore et al. 2006, see also Section 2.2.1.4). At sunrise, the molecular ion density builds up quickly, faster than H^+ density. The loss of H_2^+ producing H_3^+ is faster than that producing H^+ (e.g. Moses and Bass 2000; Galand et al. 2009). At sunset, the molecular ion density decays quickly as a result of electron dissociative recombination.

At mid-latitudes, on the one hand, electron density profiles obtained from radio occultations at Jupiter and at Saturn do not exhibit any clear local-time dependence (see Section 2.2.1.1). This may be due to additional processes (Nagy et al. 2009), such as dynamic effects combined with the less efficient electron-ion recombination in the absence of water (Moore and Mendillo 2007). On the other hand, diurnal variations in the mid-latitude electron density have been obtained at Saturn from the analysis

of SEDs (see Section 2.2.1.1). Very large reductions in the peak electron density from mid-day to mid-night have been inferred, as illustrated in Figure 6b. They extend over more than 2 orders of magnitude for the Voyager era (dotted and dashed lines) and to one order of magnitude for Cassini (dots and dash-dotted line). The peak electron densities are found to exhibit a solar-zenith-angle dependency most pronounced at dawn (Fischer et al. 2011). Even when considering the more moderate Cassini results, photochemical models cannot reproduce the observed diurnal variations using the current best estimates for the production and loss sources (Moore et al. 2012). Most likely the large diurnal variations observed from SEDs are related to the sharp peaks frequently seen in the Cassini/RSS radio occultation measurements and located below the main ionospheric peak (Kliore et al. 2009).

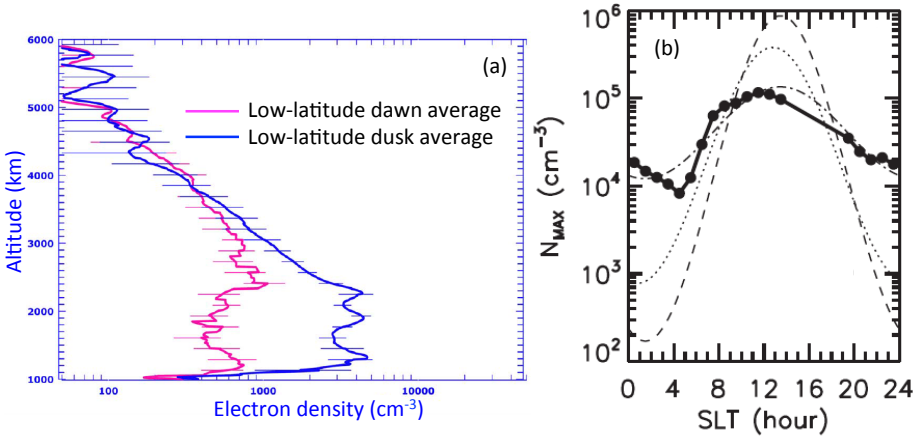

Fig. 6 Left (a): Average electron density profiles obtained by Cassini/RSS at low latitudes at dawn (pink) and dusk (blue) (Kliore et al. 2009); Right (b): Diurnal trend in the peak electron density from Cassini/RPWS SED analysis (Fischer et al. 2011) (dots linked by a thick, solid line). The dash-dotted line represents a fit to the Cassini dataset. The dotted and dashed lines are fits for the Kaiser et al. (1984) and Zarka (1985) diurnal maximum electron density trends from the Voyager era (Moore et al. 2012).

2.2.1.4 Latitudinal distribution While at Jupiter most electron density profiles analyzed in detail have been measured at mid-latitudes (see Section 2.2.1.1), the wealth of radio occultations obtained by Cassini/RSS allows the derivation of the latitudinal behavior in ionospheric properties. With the decrease in solar illumination with latitude, the peak electron density and total electron content (TEC) are expected to decrease with increasing latitude. Kliore et al. (2009) and Moore et al. (2010) showed that the reverse trend is observed, as illustrated in Figure 7. The decrease in TEC from mid latitudes towards the equator is likely due to the inflow of water from the rings and icy moons (Connerney and Waite 1984; Moore et al. 2006, 2010). The solar-driven model (solid lines) reproduces well the Cassini/RSS values (symbols) at low-latitudes when this additional loss process is included (Moore et al. 2006). The addition of water converts H^+ to H_3O^+ via the very short-lived H_2O^+:

$$H^+ + H_2O \rightarrow H_2O^+ + H$$
$$H_2O^+ + H_2O/H_2 \rightarrow H_3O^+ + OH/H \quad (12)$$

As a result in the shift from atomic, long-lived H^+ to molecular, shorter-lived H_3O^+, the electron density is reduced (Connerney and Waite 1984; Moore et al. 2006; Moore and Mendillo 2007; Müller-Wodarg et al. 2012). Moore et al. (2010) obtained a best agreement in latitudinal profiles of TEC between model and observations when imposing for the water flux a Gaussian profile centered on the equator with a peak value of 0.5×10^7 cm^{-2} s^{-1} and a full width half maximum (FWHM) of 23.5° latitude. The bulk of the gaseous water in the Saturnian system is expected to come as a neutral species from the icy moons, especially Enceladus - which replenishes the E ring (e.g. Jurac and Richardson 2005). Some of the water produced at Enceladus is lost to Saturn, mostly in the equatorial region (Fleshman et al. 2012). Though part of the water influx is neutral, there is recent evidence for water ion precipitation at low- and mid-latitudes (O'Donoghue et al. 2013).

At high latitudes, the increase in H_2 ($\nu \geq 4$) (Cravens 1987) results in a more efficient removal of H^+ through charge-exchange with H_2 (see Section 2.2.1.2). Nevertheless this increased loss does not compensate for the additional source in ionization induced by particle precipitation (e.g. Millward et al. 2002; Galand et al. 2011; Tao et al. 2011). As a result large values for the electron densities and TEC are observed (symbols in Figure 7). The main peak in the electron density profile at high latitudes is associated with H^+, replacing H_3^+ lost by electron recombination due to the large electron density. H_3^+ drives the ionospheric peak - at least in the late morning and early afternoon sector - in the absence of particle precipitation (e.g. Galand et al. 2011) and at lower latitudes at solar minimum or in the presence of ring shadowing Moore et al. (2004); Müller-Wodarg et al. (2012).

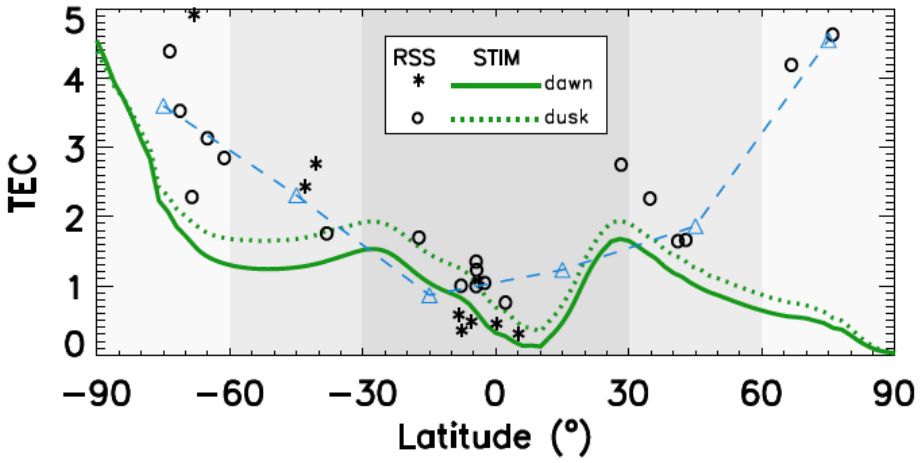

Fig. 7 Latitudinal variation of the total electron content (TEC) from the Cassini/RSS radio occultation observations (Kliore et al. 2009) and from solar-driven model simulations (Moore et al. 2010).

2.2.2 Ionospheric electrical conductances

Electrical, ionospheric conductivities are associated with particle mobility in the direction perpendicular to the planetary magnetic field and parallel (Pedersen) or perpendicular (Hall) to the ionospheric electric field. They have been calculated using ionospheric models applied to Jupiter (e.g. Millward et al. 2002; Hiraki and Tao 2008; Smith and Aylward 2009; Tao et al. 2010) and to Saturn (e.g. Moore et al. 2010; Galand et al. 2011; Ray et al. 2012a; Müller-Wodarg et al. 2012) or derived using Cassini/RSS electron density (Moore et al. 2010). The Pedersen conductivity profiles are strongly peaked in altitude, as illustrated in Figure 8. The Pedersen conducting layer associated with a current carried by ions is located in the region where the ion gyrofrequency is similar to the ion-neutral collision frequency. It corresponds to a region in the lower ionosphere dominated by molecular ions, close to the homopause. The production and mobility of these ion species therefore control the conductances (Millward et al. 2002; Moore et al. 2010; Galand et al. 2011). The Hall conductivity layer, associated with a current carried by electrons, is broader than the Pedersen layer. It is located at lower altitudes below the homopause (e.g. Galand et al. 2011) where the chemistry with hydrocarbons becomes important and complex (e.g. Kim and Fox 1994; Moses and Bass 2000). Despite an auroral forcing at Jupiter stronger than at Saturn, the jovian conductivities have peak magnitudes smaller than the kronian ones (see Figure 8). This is due to the differences in the magnetic field strength between both planets.

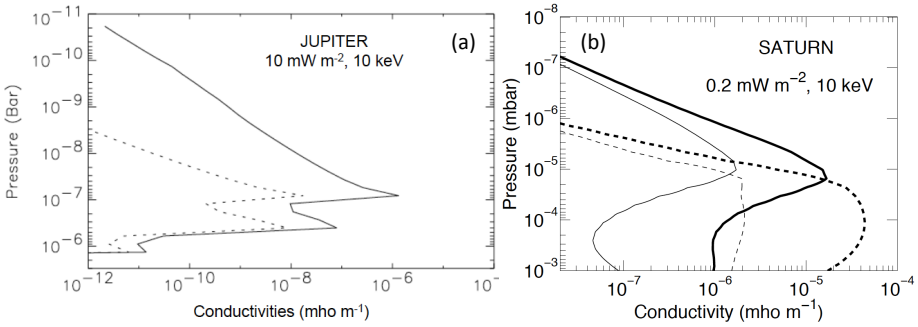

Fig. 8 Ionospheric Pedersen (solid line) and Hall (dashed lines) conductivities profiles as a function of pressure: (left) at Jupiter (Millward et al. 2002) for 10 keV electrons (Q_{prec} = 10 mW m^{-2}); (right) at Saturn for solar illumination only (78°S, equinox, solar minimum) (thin lines) and for solar and auroral 10 keV electrons (Q_{prec} = 0.2 mW m^{-2}) (thick lines) (adapted from Galand et al. (2011)).

Ionospheric conductances - or height-integrated conductivities - are most intense at low and mid-latitudes on the dayside due to solar-induced ionization and in the auroral regions over all local times due to particle precipitation (Moore et al. 2010; Galand et al. 2011; Müller-Wodarg et al. 2012). Outside these regions, the lower ionosphere, where the conductivities peak, is strongly depleted due to the absence of ionisation, though not totally, providing a low-level background conductance.

Table 2 summarizes the different values published in the literature for ionospheric, Pedersen conductances calculated using ionospheric models applied to the auroral oval regions. For a given auroral forcing (10 keV electrons with an energy flux of 1 mW m^{-2}),

Pedersen conductances at Jupiter are two orders of magnitude smaller than the values at Saturn. Ionospheric composition and integration altitude regions for the conductivities are similar at both planets. The difference in conductances comes primarily from the difference in magnetic field strength. Jupiter's magnetic field, the strongest planetary field encountered in the Solar System, is 20 times as strong as Saturn's. The conductances are dependent on the magnetic field strength through the angular gyrofrequency. If the magnetic field of Saturn is multiplied by a factor 20, the conductances are found to decrease by a factor 150 to 200 (Galand et al. 2011).

Nevertheless auroral forcing is not the same at Jupiter and at Saturn. The initial energy and energy flux of the auroral electrons is higher at Jupiter, as illustrated in Table 1. Typical values for the auroral electron characteristics are highlighted in bold in Table 2 and yield Pedersen conductance values in the 1.5–2 mho range at Jupiter and in the 10–15 mho range at Saturn (see Table 2). These jovian values are supported by estimations from field-aligned potential models - using parameterized Pedersen conductance relations: they spread from 0.7 to 1.5 mho (Smith and Aylward 2009; Tao et al. 2009; Ray et al. 2010). Therefore, difference in auroral forcing reduces the difference in conductances between Jupiter and Saturn down to one order of magnitude. At Jupiter, for 10 keV electrons with an energy flux of 10 mW m^{-2}, Millward et al. (2002) found a value for the Pedersen conductance of 0.12 mho, while Hiraki and Tao (2008) derived a value of 0.5 mho (see Table 2). Differences may be associated with differences in the induced location of the Pedersen conductive layer, in the set of ion species considered ($[H_2^+, H_3^+]$ versus $[H_2^+, H_3^+, H^+]$) and assumptions made (photochemical equilibrium versus transport included). Bougher et al. (2005) derived conductance values more than an order magnitude larger than those obtained by Millward et al. (2002) for 10 keV and 100 keV (see Table 2). Though the mean energy of the particle is 22 keV (for the bulk population) this does not explain the large difference. Differences in magnetic field models may be the reason.

As for background, solar-driven Pedersen conductance values, Tao et al. (2009) computed values of the order of 0.01 mho in the auroral regions of Jupiter, reaching 0.11 mho on the dayside at low jovian latitudes. At Saturn, they are of the order of 0.5 mho over the auroral main oval (Galand et al. 2011) increasing to a few mho at 60° latitude (Ray et al. 2012a). Over the whole range of latitudes (which does not include the main ovals) Moore et al. (2010) assessed Pedersen conductances from Cassini/RSS observations and obtained values as high as 8 mho when the full altitude profiles with sharp, narrow peaks in the low ionosphere are included. However, when considering only the topside ionosphere above 1200 km, solely driven by solar illumination, the Pedersen conductances are reduced to values below 1.5 mho.

Ionospheric conductances vary with the initial energy of the particles. Auroral electrons with low (high) energies penetrate above (below) the conductivity layer and are therefore not as effective to increase conductances. At Jupiter, Millward et al. (2002) found that 60 keV electrons, which deposit their energy near the homopause, are the most effective at enhancing electrical conductances. For larger energies, the induced electron density derived by Millward et al. (2002) decreases: as hydrocarbons are neglected in the model, the major ion is H_3^+, which is quickly destroyed through dissociative recombination. Hiraki and Tao (2008) also found that for a given energy flux Pedersen conductance increases with the initial electron energy. They derived a $(E_{prec})^{1.65}$ dependence with saturation around 300 keV, which corresponds to the upper limit of their model validity range. Furthermore, the Pedersen conductance depends on the pitch angle θ of the incident electrons. Hiraki and Tao (2008) found that the

Table 2 Pedersen conductance Σ_P calculated using energy deposition and ionospheric models and presented as a function of the ionization source (Sun, auroral electrons) over the main auroral oval. The characteristics of the auroral electrons are given in terms of the initial mean energy and energy flux. Typical values for the auroral characteristics (see Table 1) and the associated conductance are shown in bold.

Energy source E_{prec} (keV), Q_{prec} (mW m^{-2})	Pedersen conductance Σ_P (mho)	Reference [atmospheric model]
	JUPITER	
Electrons [10, 1]	0.04	Millward et al. (2002)
Electrons [10, 10]	0.12	[3D GCM]
Electrons [10, 100]	0.62	
Electrons [60, 10]	**1.75**	
Electrons [22, 100]+[3,10]+	9 (NH)[a]	Bougher et al. (2005)
Electrons [0.1, 0.5]	12.5 (SH)[a]	[3D GCM]
Electrons [1, 1]	0.008	Hiraki and Tao (2008)
Electrons [10, 10]	0.5	[1D ionospheric model]
	SATURN	
Solar only (Main oval: noon, 78°, equinox, solar minimum)	0.7	Galand et al. (2011) [1D ionospheric model
Solar + **Electrons [10, 1]**	**11.5**	using 3D neutral output]
Solar + Electrons [10, 0.2]	5	
Solar + Electrons [2, 0.2]	10	

[a] NH and SH stands for northern hemisphere and southern hemisphere, respectively.

conductance decreases by as much as 40% with increasing θ, as electrons with larger pitch angles do not penetrate as deep, further away from the conductance layer. At Saturn, Galand et al. (2011) found that auroral electrons with mean energy of 2–3 keV are the most effective at maximizing the Pedersen conductance, while the electron mean energy needs to be increased by more than 20 keV to maximize the Hall conductance. At very low energies (less than a few 100 eV) the contribution by auroral particles was found to be so low - as they only reach very high altitudes - that conductances are driven by solar illumination (Galand et al. 2011).

In presence of intense, hard aurora (energy flux $Q_{prec} > 0.04$ mW m^{-2} (at Saturn) and mean energy $E_{prec} \geq 10$ keV), the electron density closely follows the energy flux Q_{prec} of the auroral electrons (Millward et al. 2002; Moore et al. 2010; Galand et al. 2011; Müller-Wodarg et al. 2012): $\Sigma \propto (Q_{prec})^{1/2}$. It is not surprising as the conductances are roughly proportional to the main ion density, that is, approximatively to n_e. In addition, $n_e \propto (Q_{prec})^{1/2}$, at least in the region where conductivities peak (see Section 2.2.1.2). Millward et al. (2002) found the following dependence for the Pedersen and Hall conductances (in mho) induced by 10 keV electrons at Jupiter:

$$\begin{aligned} \log_{10}\Sigma_P &= \alpha_P \log_{10} Q_{prec} + \beta_P [\log_{10} Q_{prec}]^{1/2} + \gamma_P \\ \log_{10}\Sigma_H &= \alpha_H \log_{10} Q_{prec} + \beta_H [\log_{10} Q_{prec}]^{1/2} + \gamma_H \end{aligned} \tag{13}$$

where Q_{prec} is given in mW m^{-2}, $\alpha_P = 0.437$, $\beta_P = 0.089$, and $\gamma_P = -1.438$ and $\alpha_H = 0.244$, $\beta_H = 0.121$, and $\gamma_H = -3.118$.

When the energy Q_{prec} varies with local time Lamy et al. (2009); Badman et al. (2012b) the response of the ionosphere needs to be taken into account through a time

shift. Galand et al. (2011) found the following dependence for the Pedersen and Hall conductances (in mho) induced by 10 keV electrons at Saturn:

$$\begin{aligned} \Sigma_P(t) &= 11.5[Q_{prec}(t - \Delta t_P)]^{1/2} \\ \Sigma_H(t) &= 24.7[Q_{prec}(t - \Delta t_H)]^{1/2} \end{aligned} \tag{14}$$

where Q_{prec} is given in mW m^{-2}, and Δt_P and Δt_H are 10 min 12 s and 4 min 26 s (Earth minutes), respectively. The shift is a function of the energy of the incident particles, increasing significantly for smaller energies, which correspond to auroral electrons reaching higher altitudes where the ionospheric response is slower (e.g. Millward et al. 2002). Finally, the dependence of the ionospheric conductances has also been proposed in terms of field-aligned current (FAC) by Nichols and Cowley (2004) and Ray et al. (2010) (based on the ionospheric modeling by Millward et al. (2002)) and by Hiraki and Tao (2008); Tao et al. (2010). Such models allow feedback of the ionospheric conductance on the FAC.

Ionospheric conductances depend indirectly on the ionospheric electric field present in the auroral regions. When the latter is increased, Joule heating is enhanced resulting in an increase in temperatures in the upper atmosphere. The enhancement in thermospheric temperature with electric field depends on the ionospheric conductivities, that is, on the auroral electron energy flux. The heating of the upper atmosphere yields its expansion. This means that conductances are calculated over a larger vertical integral, resulting in an enhancement of their values (Müller-Wodarg et al. 2012). For instance, for 10 keV electrons with an energy flux Q_{prec} of 1.2 mW m^{-2}, when the electric field strength is increased from 80 mV m^{-1} to 100 mV m^{-1}, the thermospheric temperatures increase from 450 K to 850 K (by a factor of $\sim$1.9) and the Pedersen conductance is enhanced by 50%. This increase in conductance with the electric field depends on the electron energy flux, increasing with Q_{prec}.

Effective ionospheric conductances have been introduced in order to take into account, in current models (e.g. Nichols and Cowley 2004), the rotational slippage of the neutral atmosphere from rigid corotation due to ion-neutral frictional drag (Huang and Hill 1989; Bunce et al. 2003). The effective Pedersen conductance is defined as (Cowley et al. 2004a):

$$\Sigma_P^* = (1 - k)\Sigma_P \tag{15}$$

with the parameter k defined as:

$$k = \frac{\Omega - \omega_n}{\Omega - \omega_i} \tag{16}$$

where Ω is the planetary angular velocity, ω_n is the angular velocity of the neutral atmosphere, and ω_i is the angular velocity of the plasma. General Circulation Models (GCMs) calculate the 'true' ionospheric conductances (e.g. Millward et al. 2002; Galand et al. 2011; Müller-Wodarg et al. 2012). They include ion-neutral drag and associated neutral dynamics and can therefore be used for assessing the parameter k. At Jupiter, the derived values of k are around 0.5 (Cowley et al. 2004a) ranging from 0.3 to 0.8 throughout the whole outer regions (Millward et al. 2005; Smith et al. 2005). Millward et al. (2005) showed that the parameter k increases when the incident electron energy increases, while it decreases when the equatorward auroral voltage is enhanced. Tao et al. (2009) found regions where the slippage can yield a height-dependent k_z parameter larger than 1: this corresponds to a region where the neutral wind velocity

is larger than the ion drift velocity in the planetary rotation frame caused by Coriolis forces and viscosity. For regions where $k_z < 1$, they derived values for k between 0.25 and 0.35 over the 63–73° latitude region. Finally, Smith and Aylward (2009) found negative values of k in the ionospheric regions mapping to magnetospheric radii inside of 20 R_J as a result of super-rotation of the neutrals.

At Saturn, Smith and Aylward (2008) derived values between 0 and 0.6 at high latitudes with a mean value of 0.4 over the auroral oval, very close to the value of 0.5 derived by Galand et al. (2011). Smith and Aylward (2008) also found that the k-parameter becomes negative at 25° co-latitude at a result of super-rotation of the neutrals in this region.

2.3 Auroral emission processes

Figure 9 outlines the sequence of processes which occur after auroral particles precipitate into the H_2-dominant atmosphere leading to the radiation of UV, VIS and IR emissions.

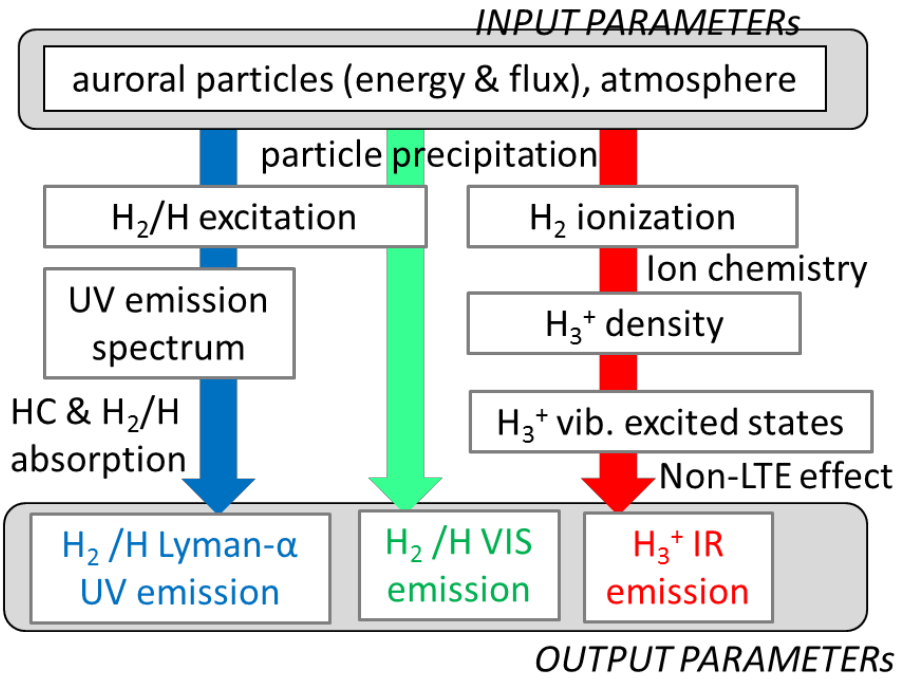

Fig. 9 Flowchart of emission processes after auroral particle precipitation into the H_2-dominated atmosphere.

2.3.1 UV emission processes: production and radiation transfer

UV photons are emitted from electron-excited molecules and/or atoms when they de-excite to their ground states. Jupiter and Saturn's UV emissions mainly consist of H Lyman α and H_2 Lyman and Werner bands excited by precipitating electron impacts. The excitation rates to the B and C states are directly related to the strength of the H_2 Lyman and Werner bands, respectively. The effect of the quenching of B and C states is small (Gérard and Singh 1982). The emission intensity of the transition band from the upper v' to the lower v'' state, $I^W_{v',v''}$, in the Werner system is given by

$$I^W_{v',v''} = I_c q^{X\to C}_{v',0} A^{C\to X}_{v'v''} / \Sigma_{v''} A_{v'v''} \tag{17}$$

where I_c is the total intensity of the C state; $q^{X\to C}_{v',0}$ represents the Frank-Condon factors for the excitation rate of the C state into the v' level; $A^{C\to X}_{v'v''}$ is the Einstein coefficient for the transition from v' to v''. The fraction $A^{C\to X}_{v'v''}/\Sigma_{v''}A_{v'v''}$ corresponds to the branching ratio for the line. The emission intensity of a $v' \to v''$ transition band in the Lyman system is also given by the total intensity of the B state with a contribution from the E and F states of 25% (Gérard and Singh 1982). Transitions from other excited states of H_2 (B', B", D, D') also contribute to EUV emission in the wavelength range 80–120 nm (Gustin et al. 2004b). Lyman α is also estimated to contribute $< 10\%$ of the total UV emissions (Perry et al. 1999).

UV auroral emissions at wavelengths < 130 nm and < 120 nm are absorbed and modified by hydrocarbon molecules and H_2, respectively. The spectrum after absorption depends on the optical depth and is a function of the absorption cross section and the column density of the absorber above the emission region as follows:

$$I_{\text{after},\lambda} = I_{\text{before},\lambda} \exp(-\tau_\lambda), \quad \tau_\lambda = \int \sigma_\lambda N_z ds, \tag{18}$$

where $I_{\text{before},\lambda}$ is the spectrum before absorption, τ_λ is the optical depth, σ_λ and N_z are the absorption cross section and density of absorber, respectively, and ds is taken along the path of the emitted photon. Synthetic H_2 spectra before and after H_2 self-absorption are shown in Figures 10a and b, respectively. The absorption cross section of hydrocarbons depends on wavelength as shown for methane by the black line in Figure 10c. The blue and green lines in Figure 10c show combined H Lyman α and H_2 spectra before and after absorption by methane.

2.3.2 Infrared emission processes: production and non-LTE effects

Auroral electron precipitation is the dominant ionization source in the high latitudes in addition to the solar EUV in the dayside. These ionization processes stimulate ion chemistry in the ionosphere. The major chemical reactions are depicted in Figure 11.

H_3^+ is one of the important species for IR emission from Jupiter and Saturn. Emission from H_3^+ is not a direct result of particle precipitation, but is a chemical product formed via the ionisation of molecular hydrogen as shown in Figure 11. It is formed via this very efficient and exothermic process:

$$H_2 + H_2^+ \to H_3^+ + H \tag{19}$$

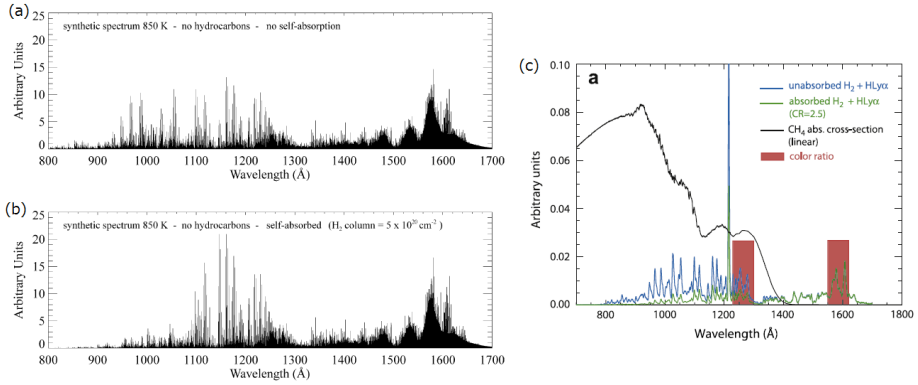

Fig. 10 Estimated spectrum (a) before and (b) after the H_2 self-absorption due to a H_2 column density of 5×10^{20} cm^{-2}, and (c) H Lyman-α and H_2 spectrum before (blue) and after (green) absorption by hydrocarbons for the case when the intensity ratio I(1550–1620 Å)/I(1230-1300 Å) = 2.5. The absorption cross section of the main absorber, methane, is shown by the black line. The blue line is a laboratory spectrum obtained from impact of 100 eV electrons on H_2 gas at 300 K, simulating an intrinsic non-absorbed auroral emission spectrum. (From Gustin et al. (2004b, 2013).)

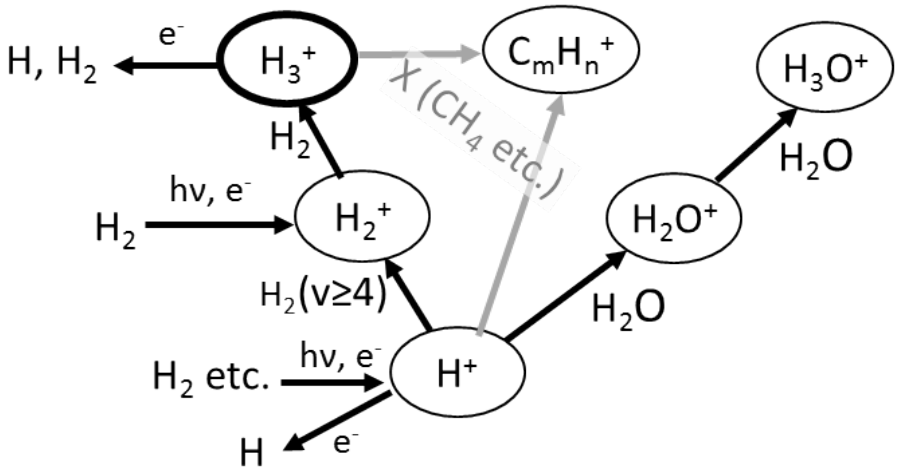

Fig. 11 Ion chemistry in the ionospheres of Jupiter and Saturn showing the main reactions described in the text.

which means that in an environment rich in molecular hydrogen, such as the upper atmosphere of a gas giant, the production of H_3^+ is a tracer of energy injected into the system. Molecular hydrogen can also be produced via more novel paths:

$$H^+ + H_2(v \geq 4) \rightarrow H_2^+ + H \tag{20}$$

followed by Reaction 19 that forms H_3^+. The life-time of H^+ is longer than that of H_3^+ by a factor of 10-100 (Kim and Fox 1994). Unfortunately, the mixing ratio of

$H_2/H_2(\nu \geq 4)$ is unconstrained by three orders of magnitude (Majeed and McConnell 1991) so how effective Reaction 20 is to shorten the life-time of H^+ is unclear.

Generally, H_3^+ is lost by these reactions:

$$H_3^+ + e^- \rightarrow H_2 + H \tag{21}$$

$$H_3^+ + e^- \rightarrow H + H + H \tag{22}$$

$$H_3^+ + X \rightarrow HX + + H_2 \tag{23}$$

where Reaction 23 is extremely efficient if X is a species with more protons than H_2 (Flower 1990). Since the thermosphere of Jupiter is mostly H and H_2, Reaction 23 is only important at very low altitudes, where hydrocarbons very efficiently quench any population of H_3^+. Above the homopause, the loss of H_3^+ is mainly governed by Reactions 21 and 22, and the H_3^+ life-time becomes a function of electron density. At the auroral latitudes, the life-time of H_3^+ is about 10 s, whereas it is about 10^3 s at lower latitudes (Achilleos et al. 1998). At Saturn, auroral life-times are about 500 s (Melin et al. 2011).

H_3^+ is excited vibrationally following collisions with background H_2 under high thermospheric temperature. The population of these vibrationally excited states is determined by the balance between collisional excitation/de-excitation and radiation transitions, i.e., IR radiation. This IR radiation effect, combined with a decrease of the H_2 density, i.e., a decrease in collisional excitation, at high altitudes produces a deviation in the excited population from the local thermal equilibrium (LTE) or Boltzmann distribution. This reduces the IR emission intensity, an effect which is estimated to be significant for Jupiter (Melin et al. 2005). The reduction ratio of the H_3^+ density, $\eta(z) = n_{H_3^+,non-LTE}/n_{H_3^+,LTE}$, is a function of H_2 density and the temperature as shown in Figure 12 (after Tao et al. 2011). As the temperature, i.e., the efficiency of the IR emission, increases and/or as the H_2 density decreases, this reduction (the non-LTE effect) becomes large. The non-LTE effect must therefore be considered when analysing IR spectra, and can be exploited to determine the incident electron energy, by considering the relationship between electron penetration depth and H_2 density (Tao et al. 2012).

Using the H_3^+ ion density, $N_{H_3^+}$, the LTE fraction η, and the atmospheric temperature T, the IR emission strength is estimated as follows,

$$I_{IR}(\omega_{if}, z) = N_{H_3^+}\eta(z)g(2J+1)hc\omega_{if}A_{if}exp(-E_f/k_BT)/Q(T) \tag{24}$$

where, e.g., for the fundamental line, I_{IR} is the emission intensity; $\omega_{if} = 2529.5$ cm^{-1} is the wavenumber; $g = 4$ is the nuclear spin weight; $J = 1$ is the rotational quantum number of the upper level of transition; h is the Planck constant; c is the velocity of light; $A_{if} = 129$ s^{-1} is the Einstein coefficient; $E_f = 2616.5$ cm^{-1} is the energy of the upper level of the transition; k_B is the Boltzmann constant; $Q = \Sigma_i(2J+1)g_i exp(-E_i/k_BT)$ is the partition function.

2.3.3 Jupiter-Saturn and IR-UV Comparison

Tao et al. (2011) have developed a model of how the above UV and IR emissions respond to different auroral electron energy and flux, and the background atmospheric temperature. This model accounts for UV absorption by hydrocarbons, ion chemistry,

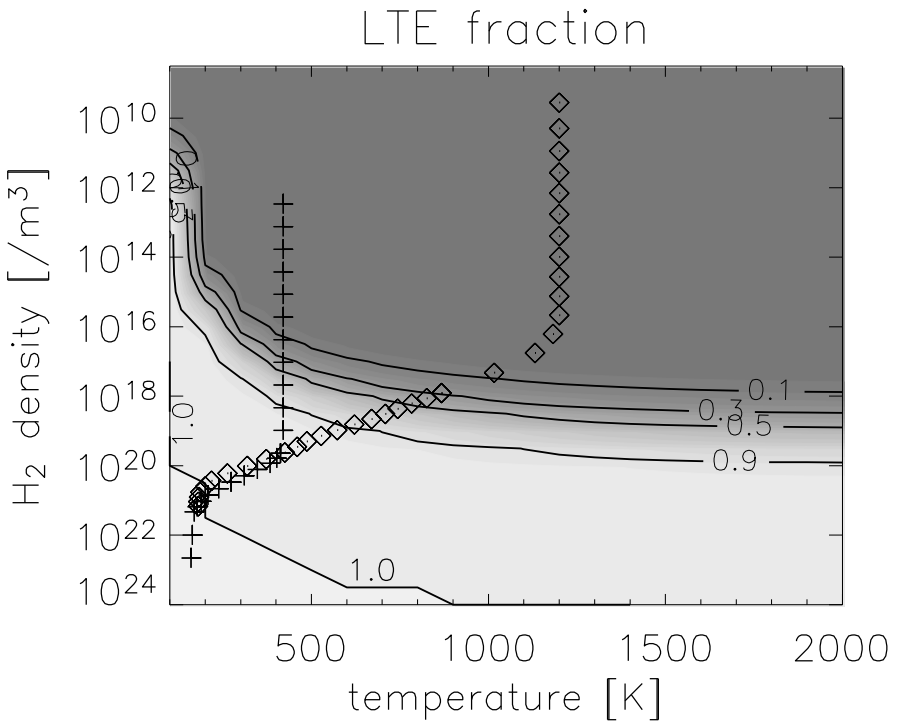

Fig. 12 Contour maps of LTE fraction as a function of temperature and H_2 density. Parameters for Jupiter's and Saturn's atmosphere are shown by diamonds and pluses, respectively.

and H_3^+ non-LTE effects. Ionization and excitation profiles for auroral electrons at Jupiter and Saturn derived from the model are shown in Figures 13a and b, respectively. These can be compared with profiles given in Figures 3 and 4. As remarked in Section 2.1.1.2, higher energy electrons reach lower altitudes in the atmosphere before depositing their full energy.

The modelled dependences of altitude-integrated values of UV and IR emissions on electron energy ϵ_0, flux f_0, and exospheric temperature T_{ex} for Jupiter are shown by the diamonds and crosses in Figure 14. The same is shown for Saturn in Figure 15. The emission intensities are normalized to the conditions $\epsilon_0 = 10$ keV, $f_0 = 0.15$ μA m^{-2}, and $T_{ex} = 1200$ K for Jupiter and the same ϵ_0 and f_0 with $T_{ex} = 420$ K for Saturn. The normalized emission intensities of UV (lines in 117–174 nm range) and IR (Q(0,1-) line) are 38 kR , and 33 μW m^{-2} str^{-1} for Jupiter, and 37 kR and 0.80 μW m^{-2} str^{-1} for Saturn. Note that H_2O was included in the model by Tao et al. (2011) but not here for Saturn's high latitude regions.

The different dependence of emission rates on electron energy and temperature between the Jupiter and Saturn models can be summarized as two main points: (1) the temperature-dependence of IR emissions for Saturn covers three orders of magnitude (Figure 15c), which is much larger than that for Jupiter (one order of magnitude, Figure 14c), and (2) the electron energy dependence of IR emission for Saturn (Fig-

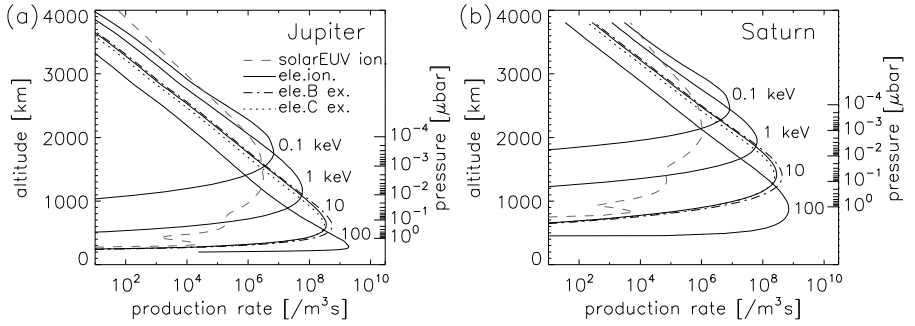

Fig. 13 Altitude profiles of ionization and excitation rates caused by auroral electrons (black lines) and solar EUV (grey lines) at (a) Jupiter and (b) Saturn. Ionization rates caused by auroral electrons increase with increasing electron initial energy, where energies of 0.1, 1, 10, and 100 keV with a flux of 0.15 μA m^{-2} have been shown. Excitation rates for B and C states caused by 10 keV electrons are shown by the dot-dashed and dotted lines, respectively. The dashed grey lines show the sum of production rates (H_2^+; H^+, and hydrocarbon ions) due to solar EUV.

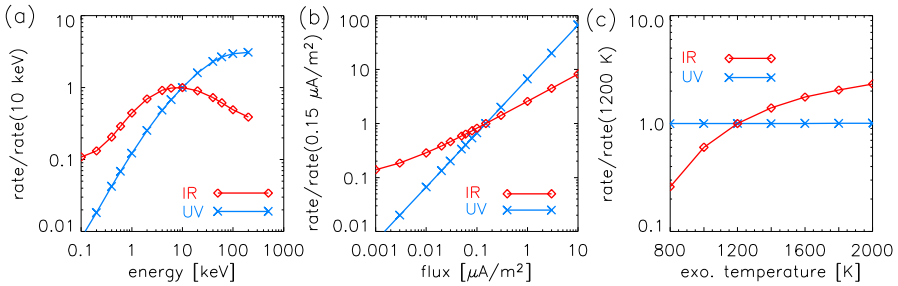

Fig. 14 Jupiter UV (blue line with crosses) and IR (red line with diamonds) dependences on (a) electron energy, (b) electron flux, and (c) temperature, after Tao et al. (2011).

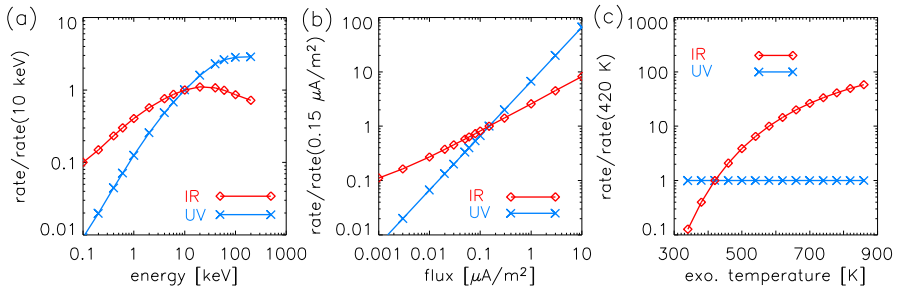

Fig. 15 Saturn UV (blue line with crosses) and IR (red line with diamonds) dependences on (a) electron energy, (b) electron flux, and (c) temperature, after Tao et al. (2011) but excluding the effects of H_2O.

ure 15a) has a shallower slope in the energy range of 0.5–5 keV than that for Jupiter (Figure 14a).

To explain the first of these differences, Figure 16 shows the dependence of Jovian emission intensities across the same temperature range as initially considered for Saturn in Figure 15c, i.e. 300–820 K. The jovian H_3^+ emission intensity now shows a large IR variation comparable to that of Saturn (Figure 15c). To address the second difference, the electron energy dependence, Figure 16b shows the dependence of Saturn's emission intensities on electron energy for a high temperature case. This profile now has a steeper slope in the range 0.5–5 keV. Therefore the differences between Saturn and Jupiter in both the rate of variation with temperature and the electron energy dependence of the IR emission are due to the lower prevailing temperature at Saturn.

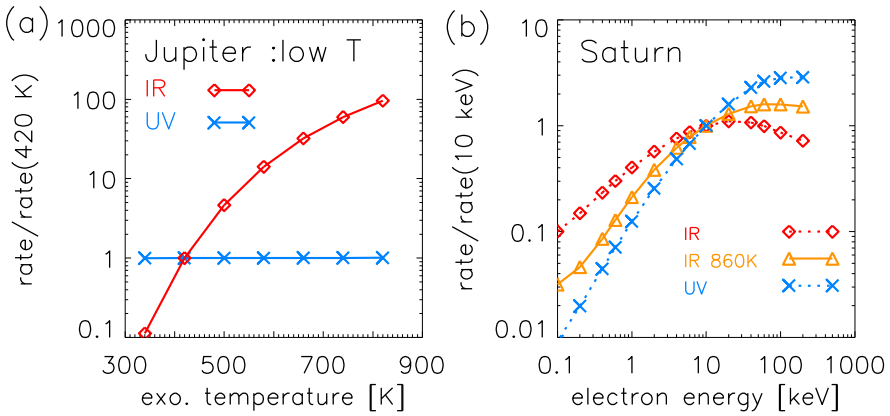

Fig. 16 Test of UV/IR dependence on (a) low temperature at Jupiter and (b) electron energy at Saturn with an exospheric temperature of 860 K.

2.3.4 Time Variation

Figure 17 shows the processes from auroral electron precipitation to UV and IR emissions with their characteristic time scales, estimated by the above model. The UV aurora at Jupiter and Saturn is directly related to excitation by auroral electrons that impact molecular H_2, occurring over a time scale of 10^{-2} s. The IR auroral emission involves several time scales: while the auroral ionization process and IR transitions occur over $< 10^2$ s, the time scale for ion chemistry is much longer at 10^2–10^4 s. Associated atmospheric phenomena such as temperature variations and circulation are effective over time scales of $> 10^4$ s. Tao et al. (2013) demonstrated the implications of these different timescales on the UV and IR emissions. They found that for events with a timescale of ~ 100 s, ion chemistry, which is present in the IR emission process but not the UV, could result in the production of different features between the two wavelength ranges. They also applied these results to observations of the jovian polar UV flashes identified by Bonfond et al. (2011) and the Io footprint aurora (Clarke et al. 2004) and showed that whether the IR intensity varies in correlation with the UV or not depends on the number flux of the auroral electrons and their characteristic energy. Section 3.4 summarises the comparison between observed UV and IR emissions.

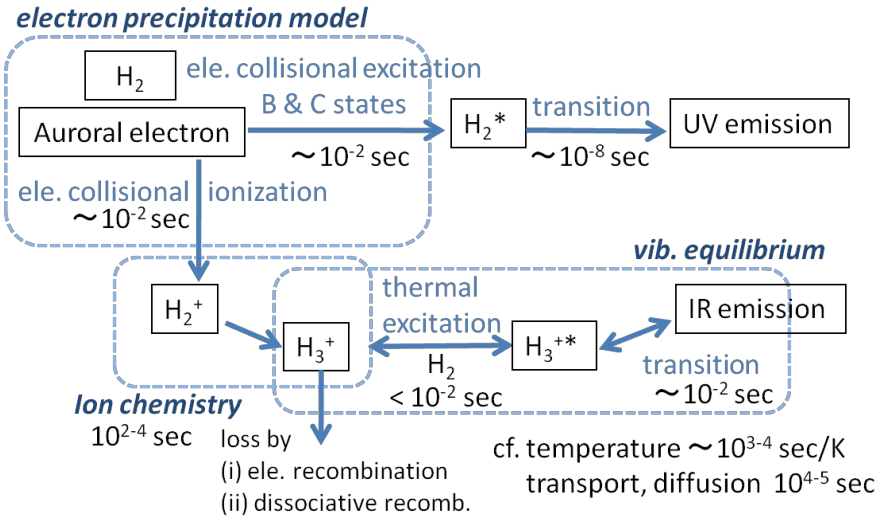

Fig. 17 Flowchart of UV and IR auroral emissions with the timescale for each process.

2.4 Future Developments

Auroral particle energy deposition and transport models are critical for the assessment of the ionospheric state and the derivation of the auroral electron initial energy (and energy flux in the presence of ions) from UV analysis. A careful comparison between such models using clear and detailed information for input parameters, such as neutral profiles in altitude and incident electron intensity in energy and angle, should be carried out. Different methods adopted, such as Monte Carlo versus multi-stream, have been validated at Earth (e.g. Solomon 1993, 2001). There is therefore no reason, intrinsic to the methods adopted, to justify differences sometimes found between electron production rates induced by a given initial electron distribution in a given atmospheric model. Beside a careful comparison between suprathermal electron models, the contribution of energetic ions should be re-assessed, especially in the return current regions, and compared to the contribution from energetic electrons using realistic values for incident particle populations.

The estimate of the electron density by ionospheric models, critical for calculating ionospheric conductances, is limited by the large uncertainties in the k_1^* effective reaction rate. Detailed calculations of the amount of H_2 vibrational ($v \geq 4$), especially in the auroral regions, are required using the latest thermospheric density estimates and reaction rates. The k_1^* effective reaction rate is expected to change with (at least) season, latitude, and local time. Other limiting factors of the electron density assessment include: (1) the exact amount of water influx, which has significant effect at Saturn at low latitudes (Kliore et al. 2009; Moore et al. 2010), but whose contribution is not well known at Jupiter; and (2) the effect of dynamics, which could be large in the auroral regions (e.g. Smith and Aylward 2009; Tao et al. 2009; Galand et al. 2011; Müller-Wodarg et al. 2012). In addition, it seems highly relevant to try to characterize the properties and identify the origin of the sharp, narrow electron density peaks seen

in Cassini/RSS profiles and most likely responsible for the diurnal distribution derived from SED analysis.

It is critical to improve the assessment of the ionospheric conductances, as they control the current density that flows through the ionosphere closing the global magnetospheric current system and strongly influence the Joule heating of the thermosphere in the auroral regions. To this aim we need to improve the estimate of input parameters (e.g., k_1^*, water influx, ionospheric electric field), which drive the ionospheric models and influence the assessment of the conductances. This requires detailed modeling efforts (e.g., of H_2 ($v \geq 4$)) combined with the analysis of a multi-instrumental dataset, including estimates from electron density (through radio occultations and SEDs (see Section 2.2.1.1), H_3^+ density and temperature (from IR spectroscopic observations (see Section 3.3)), thermospheric densities and temperature (from UV occultations, Yelle and Miller 2004; Nagy et al. 2009), particle characteristics (from UV and X-ray spectroscopic observations (see Sections 3.1.1 and 4)) and, in the near future through Juno at Jupiter, in situ particle and field measurements). As illustrated in Moore et al. (2010) and Müller-Wodarg et al. (2012), such information combined with self-consistent upper atmospheric models can be used to reduce the parameter space and improve our assessment of the ionospheric state, better constrain its drivers, and improve our understanding of the magnetosphere-ionosphere-thermosphere coupled system.

Such studies need to be carried out not only under steady-state auroral forcing but also for time variable auroral forcing, and considering the different timescales for different processes. While energy seems to be trapped at high latitudes for an imposed day-to-day variability (I. Müller-Wodarg, personal communication, 2012), higher frequency forcing as attested by auroral observations, from the X-rays and UV to the IR, may alter this picture and the system response at a global scale. Auroral emission models like that described above typically deal with a localised region including detailed collision processes. Therefore, the horizontal distributions (in longitude and latitude) of UV emission and IR spectra, which are affected by magnetospheric and thermospheric dynamics, are beyond the auroral emission model alone. In order to understand the relation between these auroral characteristics and their energy source using a modeling approach, coupling multiple models is essential, e.g., combining an auroral emission model with an atmospheric model to know the temperature variation and energy budget, and/or with a magnetosphere-ionosphere coupling model, a magnetosphere global model, or a magnetosphere chemical model to know where and when auroral electrons are energized and where H_2O precipitates. Finally, the use of low latitude observation- or model-based atmospheres results in discrepancies with auroral observations at high latitudes. Observation-model comparisons based on recent observations are also required to improve the atmosphere model at high altitudes as proposed by Gérard et al. (2009).

3 Ground- and space-based observations of UV and IR aurora

The largest outstanding gap in our understanding of the upper atmosphere of the gas giants is that they are all much hotter than solar input alone can produce. This 'missing' energy is very large: the temperatures observed in the thermosphere are several hundreds of Kelvin hotter than models can produce. The auroral process, whereby energetic particles impact the upper atmosphere at the intersection of magnetic field lines and the planetary atmosphere, is capable of injecting much energy, mainly in the

form of Joule heating, into very localized regions on the planet. Therefore, the auroral process becomes a powerful source of energy for the upper atmosphere, heating it several hundreds of Kelvin above the temperature that solar heating alone can provide. It is not currently understood how the energy injected into the auroral regions could be redistributed – there is even evidence that injecting energy at the poles has the effect of cooling the equator (Smith et al. 2007). In this section we discuss how remote sensing of the ultraviolet and infrared aurora can help us understand this energy transfer.

3.1 UV observations

The UV aurorae can be divided into three regions by their characteristics: moon footprint aurora, main auroral emission, and high latitude ('polar') aurora.

Auroral footprints of the satellites Io, Europa, and Ganymede on Jupiter, and Enceladus on Saturn have been detected. The variation in the separation distance of the multiple Io footprint emissions (Bonfond et al. 2008), their intensity (Bonfond et al. 2012), tail length (Hill and Vasyliūnas 2002), and appearance and disappearance of the Enceladus footprint aurora (Pryor et al. 2011) have been attributed to variations in the plasma environments.

The main auroral emission is rather stable and encircles the magnetic poles. For Jupiter, the main emission surrounds a dark polar dawn region, while several features broaden in the dusk region (see Section 6.1.1.2, Grodent et al. 2003b). The main emission intensity decreases in the noon sector (Radioti et al. 2008b). Intense 'storms' of emission have been reported along the dawn main oval (Gustin et al. 2006).

An enhancement in the emission intensity of the Io plasma torus, observed in May 2007 (Yoneda et al. 2009), has been correlated with the following auroral behaviour: i) a shift to lower latitude of the main auroral oval and a lesser shift of the Ganymede footprint, ii) an increase in the main oval intensity, iii) a decrease in the Io footprint auroral intensity (Bonfond et al. 2012), and iv) a decrease in the (HOM) radio emission (Yoneda et al. 2013). An enhancement in the outward transport of heavy flux tubes, possibly caused by an increase in Ios volcanic activity, and their replacement by inward-moving hot, rare flux tubes (interchange) is suggested to decrease the plasma density around Io and the footprint aurora intensity (Bonfond et al. 2012; Hess et al. 2013). It is also proposed that movement of the main oval to lower latitude, also identified by comparing images from 2000 and 2005, could be caused by shrinking of the plasma corotation region in the middle magnetosphere, or enhancement of the azimuthal current which modifies the magnetic field mapping region, which could be caused by an increase in the mass outflow rate, or solar wind compression, as predicted by models (e.g. Hill 2001; Nichols and Cowley 2003, 2004; Grodent et al. 2008; Tao et al. 2010; Nichols 2011; Ray et al. 2012b). An external solar wind effect is also suggested for UV intensity variations (e.g. Clarke et al. 2009; Nichols et al. 2009b, see also Delamere et al. in this volume).

At Saturn, the observed shape of the main oval varies dynamically from a circle to a spiral shape (Clarke et al. 2005). The position of the centre of the auroral oval oscillates at a period close to that of planetary rotation (Nichols et al. 2010), while the intensity of radio, infrared (H_3^+) and UV (H, H_2) emissions are modulated by the magnetospheric rotation periods separately in the northern and southern hemispheres (Sandel et al. 1982; Nichols et al. 2010; Badman et al. 2012b; Carbary 2013). Saturn's main auroral emission also demonstrates a significant local time asymmetry, being

generally more intense in the dawn-to-noon sector (Trauger et al. 1998; Lamy et al. 2009; Badman et al. 2012b; Carbary 2012). This asymmetry is related to the solar wind interaction with the outer magnetosphere, via a stronger flow shear between the solar wind flow and rotating magnetospheric plasma (anti-sunward v. sunward) on the dawnside than on the duskside (both anti-sunward).

At high latitudes, more local and shorter-time variations are often observed both for Jupiter and Saturn. At Jupiter the high latitude auroral emissions vary on timescales from several seconds (Waite et al. 2001; Bonfond et al. 2011) to a few days (Radioti et al. 2008a) in addition to persistent distributions characterized by dark or variably-bright regions (Grodent et al. 2003b) and sun-aligned arcs (Nichols et al. 2009a). At Saturn, the main emission sometimes intensifies and broadens toward high latitudes associated with solar wind compressions (Clarke et al. 2005) and small bifurcations have been reported close to the main aurora, and associated with the solar wind interaction (Radioti et al. 2011a; Badman et al. 2013).

3.1.1 UV color ratio studies

Absorption of UV emission by hydrocarbons depends on wavelength with a large effect on short wavelengths < 130 nm, as shown in Figure 10. The UV color ratio, defined as the ratio of the intensity of a waveband unabsorbed by hydrocarbons (e.g. 155–162 nm) to that of an absorbed waveband (e.g. 123–130 nm), informs us how much hydrocarbon exists above the emission altitudes. Since the hydrocarbons exist at low altitudes, increases in the hydrocarbon column are an indicator of either enhanced penetration depth, and thus energy of the auroral primary particles, or of increases in the high-altitude hydrocarbon content caused by modification of the local atmosphere (e.g. Livengood and Moos 1990; Harris et al. 1996; Gérard et al. 2002, 2003; Gustin et al. 2004a).

The northern and southern aurora observed by the International Ultraviolet Explore (IUE) spacecraft showed that the attenuation by hydrocarbons varies in phase with intensity (Livengood and Moos 1990). Hubble Space Telescope (HST) observations also show a positive correlation between the energy flux deduced from the auroral brightness and the mean electron energy from the color ratio (Gustin et al. 2004a). Compared with their emission model, the electron energy producing the main emission lies between $\sim 30 - 200$ keV, with a large enhancement around 08 LT possibly due to the occurrence of dawn storms. The energy flux varies between $2 - 30$ mW m^{-2}. The observed relationship between the auroral electron energy fluxes and the electron energies in the main oval is compatible with that expected from Knight's theory of field-aligned currents (Knight 1973), taking source plasma parameters at the magnetospheric equator well within the observed range.

In addition, fitting of UV spectra can be used to determine the absorption by H_2, where the H_2 column density is also related to the auroral electron energy (e.g. Wolven and Feldman 1998; Gustin et al. 2009).

Colour ratio studies have also been performed for Saturn's H_2 aurora and reveal primary electron energies of 10–20 keV (Gustin et al. 2009; Lamy et al. 2013).

3.2 Visible emission

Although intense reflection of solar radiation has so far prevented the detection of visible (VIS) emission on the dayside, nightside visible aurorae have been detected by Galileo at Jupiter (Vasavada et al. 1999; Ingersoll et al. 1998) and Cassini at Saturn (Kurth et al. 2009). At Jupiter, observations of the northern, nightside main emission and Io footprint made at visible wavelengths by Galileo showed they lined up well with their locations observed in the UV by HST on the dayside (Grodent et al. 2008). The visible aurora morphology changes with local time: from a multiple branch, latitudinally distributed pattern post-dusk to a single narrow arc before dawn. The power emitted at VIS wavelengths is 2–3 orders less than those at the UV/IR wavelengths. Detailed analysis of Saturn's visible auroral emissions has yet to be published.

3.3 Infrared emission from H_3^+

We focus here on auroral IR emission, generated by transitions between rotational and/or vibrational states of H_2 and H_3^+ molecules. Some of the emission lines are at wavelengths that can be observed through the Earth's atmospheric window, i.e., around 2.1, 3.4 and 3.9 micron, by ground-based telescope facilities. Recently the Visual and Infrared Mapping Spectrometer (VIMS, Brown et al. (2004)) instrument on Cassini has provided high spatial resolution observations of Saturn's IR aurora.

The observed IR emissions show both similarities and differences with the UV emissions in their spatial distribution. The IR emissions are also divided into the three characteristic regions: the moon footprint aurora, the main auroral emission, and high latitude aurorae. The Jovian IR main aurora and high latitude emission have both longitudinal and local time (LT) fixed features (Satoh and Connerney 1999). Baron et al. (1996) identified a positive correlation between Jupiter's spatially-unresolved IR auroral intensity and the solar wind dynamic pressure. Large-scale polar brightenings and multiple arc bifurcations have also been observed in Saturn's polar infrared emission, reflecting the solar wind interaction (Stallard et al. 2008; Badman et al. 2011a, 2012a). Interestingly, the Io footprint was first observed in the infrared by Connerney et al. (1993) and remains the only moon footprint to have been observed at wavelengths outside the ultraviolet.

Observations of emissions from H_3^+ have probed the ionospheres of Jupiter, Saturn, and Uranus for over two decades. The parameters that can be derived from either imaging or spectral observations depend on the spectral resolution, wavelength coverage, and the signal-to-noise ratio (SNR). The parameters that can be derived are as follows:

1. The intensity of the observed H_3^+ emission reveals the morphology of the auroral deposition, which directly relates to where particle precipitation is sourced from in the magnetosphere (e.g. Connerney et al. 1998; Bunce et al. 2008; Badman et al. 2011b; O'Donoghue et al. 2013).
2. The H_3^+ temperature, which, when observed from environments in Local Thermal Equilibrium (LTE), is equal to the temperature of the surrounding neutrals (e.g. Stallard et al. 2002; Melin et al. 2007; O'Donoghue et al. 2014). The observed temperature stems from the energy that is injected into the upper atmosphere mainly via Joule heating (Achilleos et al. 1998; Bougher et al. 2005; Tao et al.

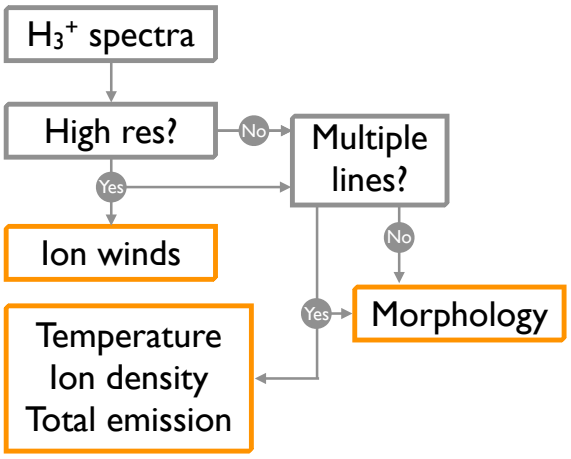

Fig. 18 A flowchart of the parameters that can be derived from H_3^+ spectral observations, which is a function of spectral resolution, wavelength coverage, and signal-to-nose.

2009; Müller-Wodarg et al. 2006). Whilst the gas giants are generally thought to be in a state of *quasi*-LTE (Miller et al. 1990), this assumptions breaks down in the upper thermosphere of Jupiter (Melin et al. 2005), where higher ro-vibrational states are populated below the expected Boltzmann distributions, relative to lower states. Without accounting for this underpopulation, one may derive temperatures that are an under-estimation of the actual thermosphere temperature, weighted towards lower altitudes.

3. The ionospheric column integrated H_3^+ density, which is directly related to the conductivity, or the ability to drive currents through the upper atmosphere. As H_3^+ is formed via the ionization of molecular hydrogen, the number of ions present in the auroral ionosphere is a function of the particle precipitation energy and flux (Tao et al. 2011).
4. The total energy emitted by H_3^+ over all wavelengths (Lam et al. 1997; Stallard et al. 1999; Lamy et al. 2013). This is energy lost to the atmosphere via radiation to space, which has an overall cooling effect (Miller et al. 2010). This process becomes more effective as the temperature increases; at Jupiter, H_3^+ is said to behave as an effective thermostat, removing the atmosphere's ability to absorb any short-term injections of energy.
5. The line-of-sight ionospheric velocities derived from high resolution observations with $R = \lambda/\Delta\lambda > 25,000$ (e.g. Stallard et al. 2001, 2007b,2007a). The ionosphere is the conduit for vast magnetosphere-ionosphere coupling currents at Jupiter and Saturn, and is subjected to $\mathbf{j}\times\mathbf{B}$ forces to which the neutral atmosphere is oblivious. By measuring these ion winds, we are indirectly measuring the angular velocity of the regions in the magnetosphere to and from which the ionospheric currents flow, assuming perfect coupling.

The flow-chart in Figure 18 summarizes the spectral requirements needed to obtain these parameters. More recently, Tao et al. (2012) suggested that by comparing the intensity of different H_3^+ spectral lines, the flux and energy of the particle precipitation could be derived. Whilst this requires large SNRs, these developments have the poten-

tial to enable observations of H_3^+ to provide a near complete view of the energy terms of the upper atmosphere, without the need for simultaneous ultraviolet and infrared observations. As noted below, however, infrared observations are not sensitive to short term auroral variability, due to the relatively long life-time of the H_3^+ ion.

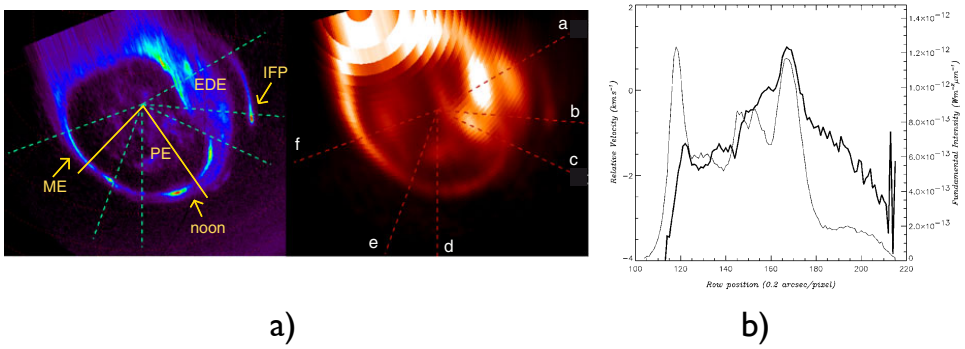

Fig. 19 a) Simultaneous ultraviolet H and H_2 and infrared H_3^+ images of Jupiter's northern aurora from Radioti et al. (2013b) obtained in 2004. There are many similarities, but also significant differences, mainly in the polar emissions. b) An example of the intensity (light) and velocity (bold) profiles of H_3^+ from 1998 observations of Jupiter's northern auroral oval from Stallard et al. (2001). This represents a cut through the oval, approximately connecting *f* and *a* in a). The ionospheric plasma exhibits a strong lag from co-rotation.

Jupiter is the giant planet closest to us and it has the strongest planetary magnetic field in our solar system. Consequently, it is the brightest source of H_3^+ in the night sky. Since the molecular ion was detected for the first time outside the laboratory by Drossart et al. (1989), there has been a plethora of both imaging and spectral studies, addressing a range of magnetospheric, ionospheric, and thermospheric questions. Here, we highlight a handful of studies that showcase the versatility of H_3^+ as a tool to study giant planets in general, and Jupiter in particular.

The ratio of emission line intensities reflects the temperature, which has been measured as high as ∼1000 K at high latitudes (e.g., Stallard et al. 2001) and up to several hundred K at low-to-middle latitudes (Lam et al. 1997). Lam et al. (1997) analyzed medium resolution H_3^+ spectra obtained with CGS4 on the United Kingdom Infrared Telescope (UKIRT), covering a full rotation of the planet, thus deriving the H_3^+ temperature and density as a function of longitude. This provided a map of the noon ionosphere for all longitudes, showing that the temperature difference between the equator (which is cooler) and the auroral region is only a couple of hundreds of Kelvin. This highlights the complexity of the 'energy crisis' – in order to heat the entire atmosphere, this heating needs to be present at all latitudes.

The observed Doppler shift of the emission lines reveals the line-of-sight velocity of ion and neutral winds in the upper atmospheres of the giant planets. At Jupiter, the ion velocity reaches up to 3 km s^{-1} in the direction opposite to planetary rotation (Rego et al. 1999; Stallard et al. 2001), with spatial distributions associated with the emission intensity (Stallard et al. 2003). Raynaud et al. (2004) observed a H_3^+ 'hot-spot' on Jupiter's northern aurora using the Fourier Transform Spectrometer (FTS) mounted on the Canada France Hawaii Telescope (CFHT) in the 2 μm region. This

region had a temperature 250 K higher than the rest of the auroral region, which had an average temperature of ∼1150 K. Using the same data, Chaufray et al. (2011) were able to simultaneously derive, for the first time, the H_3^+ ion velocity and the neutral H_2 velocity, showing that the 'hot-spot' had an ion velocity of 3.1±0.4 kms^{-1}, whereas the neutral atmosphere rotated with an upper limit velocity of 1 km s^{-1}. The intensity (thin) and velocity (bold) profiles can be seen in Figure 19b, showing regions of corotation (steep gradients), sub-corotation (shallow gradients), and stagnation (flat). These latter regions are regions connecting directly to the solar-wind, whereas the former two connect to regions within the magnetosphere.

Using narrowband IRTF NSFCAM images of H_3^+ emission, including emission from the Io footprint aurora, Connerney et al. (1998) constrained the existing magnetic field models of Jupiter, adding important constraints to the morphology of the magnetic field at magnetic latitudes equatorward of the main auroral oval. This kind of imaging requires filters that are very narrow, and there are only three tuned to H_3^+ emission in existence today, all at the NASA IRTF.

Whilst limited by SNR and low spatial resolution, the techniques employed here highlight the versatility of the 2 μm region, observing through the telluric K window. In general, the telluric L and L' water absorption window between 3.4 and 4.1 μm offers brighter H_3^+ Q-branch transition (higher SNR), and less absorption.

Analysis of Cassini VIMS observations that were obtained during the Jupiter flyby at the end of 2000 by Stallard et al., [manuscript in preparation], revealed that the nightside (dusk to midnight) ionosphere was severely depleted in H_3^+, showing none of the mid- to low latitude emission observed by Rego et al. (2000) on the dayside at local noon. This absence indicates that there may not be a soft low-latitude component of particle precipitation away from the aurora.

At Saturn, IR spectral observations reveal anti-corotational convection (Stallard et al. 2007b) and a change in ionospheric velocities related to solar wind compression of the magnetosphere (Stallard et al. 2012b). Measurements of the temperature of the thermosphere vary significantly over time between ∼ 400–600 K (Melin et al. 2007; Melin et al. 2011; Stallard et al. 2012c; O'Donoghue et al. 2014).

3.4 Simultaneous infrared and ultraviolet auroral observations

By analyzing observations obtained in two or more wavelength bands that are both spatially overlapping and temporally simultaneous, it is possible to get a more complete view of the auroral processes. Because it has been very difficult to coordinate these multi-spectral campaigns of ground- and space-based observations, there are currently very few examples and many studies rely on statistical or average comparisons.

3.4.1 UV and IR altitude profiles

Grodent et al. (2001) developed a one dimensional model which couples a two-stream electron transport of electron energy deposition with a thermal conduction of Jupiter's atmosphere. The electron spectrum required is constrained by comparing the temperature predicted by the model with the observations. The characteristic energy varies from 100 eV for high altitude heating to 22 keV, while other non-particle heat sources are also required to balance the hydrocarbon cooling. This auroral electron spectrum

produces UV emission with its peak at ∼200 km above the one bar pressure level, which is lower than the IR emission peak altitude ∼350 km (Clarke et al. 2004).

Limb imaging observations and comparison with spectroscopy of UV auroral emission provides a unique restriction for the high latitude atmosphere and auroral electron energy (Gérard et al. 2009). This study showed that the emission peak of Saturn's nightside is located 900–1300 km above the 1-bar level. In order to be coincident with the results given by the FUV and EUV spectra, a temperature enhancement is indicated compared to the low-latitudes. Comparing observations with the auroral profiles estimated by an auroral electron precipitation model that assumes a modified atmosphere profile, the characteristic energy of the precipitated electrons is found to be 5–30 keV.

The altitude profile of IR emission observed by Cassini shows the peak altitude lies at $\sim 1155 \pm 25$ km, almost the same as that of the UV, while the emission profile seems narrower in height than the UV profiles (Stallard et al. 2012a). This is explained by the large contribution to UV emission at higher altitude by Lyman α. Ambiguity in the H_2 profile assumed in the model study leads to a broader estimate of IR emission across altitudes.

3.4.2 Morphology and Time variability

Clarke et al. (2004) presented the first study of simultaneous infrared and ultraviolet observations of Jupiter, comparing HST and ground based images. Having applied a 'best guess' de-convolution to the ground-based observations to remove the blurring effect of the Earth's atmosphere, they were able to compare images of auroral emissions in the two wavelength bands. They showed that on global scales, the morphology of the emission of H_2 and H_3^+ from the main oval is remarkably similar. There were, however, differences in the emission pole-ward of the main oval, regions connected to the solar wind (Vogt et al. 2011). Additionally the H_3^+ limb emission was brighter than predicted by a simple cosine function, likely to be the result of the bulk of the emission in the two wavelengths being produced at different altitudes.

Radioti et al. (2013a) analyzed the simultaneous Clarke et al. (2004) observations in greater detail and found that most of the main emission features (main oval, dark polar region, equator-ward emission, and the Io footprint), where all co-located in the infrared and the ultraviolet. However, polar emissions were not co-located in the two wavelengths. These emissions can be variable in the ultraviolet on time-scales of 2-3 minutes (Bonfond et al. 2011), which is much too short to be observed in the H_3^+ emission as discussed in Section 2.3.4. The excitation of H and H_2 by electron precipitation produces an almost instantaneous emission response, and the UV emission traces the instantaneous injection of energy into the thermosphere. The IR picture is somewhat different. Because H_3^+ is formed via chemical reactions via the ionization of molecular hydrogen, and subsequently thermalizes to the surrounding neutral atmosphere, there is both a lag in response to precipitation and a life-time associated with the ion. The life-time is governed by the electron density, and is therefore a strong function of altitude. This means that H_3^+ does not respond to particle precipitation in the same manner as H and H_2 does in the ultraviolet. Given that H_3^+ life-times at Jupiter are 4 to 40 seconds (Radioti et al. 2013a) and up to 10 minutes at Saturn (Melin et al. 2011), the emitting ions can be subjected to significant horizontal transport within the thermosphere, and thus create a more diffuse view of the precipitation morphology (Tao et al. 2013; Radioti et al. 2013a). More relevant, however, is the fact that H_3^+ emissions will map the ion life-time average of the particle precipitation morphology.

This stands in stark contrast to the ultraviolet, which represents an instantaneous view of the magnetospheric injection of energy.

Additionally, without a knowledge of the temperature variability of the thermosphere across the polar cap, it is difficult to disentangle the relationship between H_3^+ temperature and density, both of which drive intensity. Whilst hydrocarbons can feasibly be upwelled by energetic particle precipitation – destroying H_3^+ – such an event could also act to increase the temperature, thus offsetting the decrease in intensity produced by the lost of ionospheric ions.

Using Cassini VIMS and UVIS data, Melin et al. (2011) analyzed simultaneous observations of Saturn's southern aurora, showing that over very small spatial scales, there can be significant differences between H, H_2, and H_3^+ emissions outside the main oval. This can be seen in Figure 20. The broadness of H Lyman α is the result of multiple scattering within the thermosphere, whilst H_3^+ displays the same morphology as H_2 in the main oval.

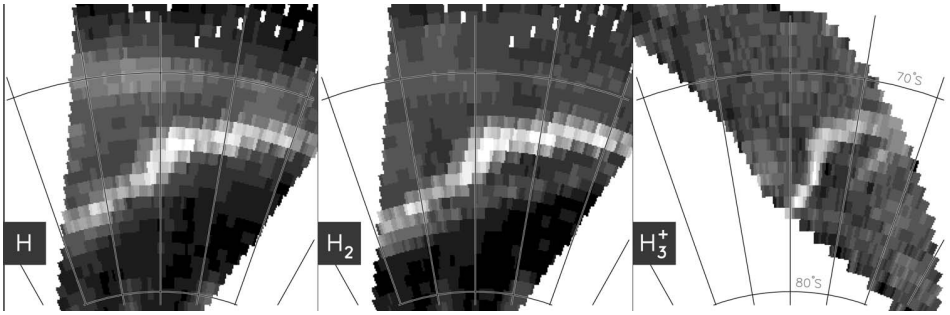

Fig. 20 The simultaneous H, H_2 (both in the ultraviolet), and H_3^+ (infrared) observations of Saturn's southern aurora of Melin et al. (2011), obtained with Cassini VIMS and UVIS. Whilst only a subset of these field-of-views are temporally simultaneous, there are significant differences between all three species.

Lamy et al. (2013) combined Cassini observations of Saturn's southern aurorae at radio, infrared, and ultraviolet wavelengths, while simultaneously monitoring the energetic neutral atom (ENA) intensification, which represents ion injections in the middle magnetosphere. These observations revealed three atmospheric auroral source regions: a main oval co-located with the bulk of the Saturn Kilometric Radiation (SKR) emission and lower intensity emissions poleward and equatorward of this. Sub-corotating features exist along the main oval, while overall the intensity is modulated in local time at the southern magnetospheric rotation period. The polar emissions from H_3^+ were more intense relative to the main oval than either of the UV emissions from H or H_2, but as the temperature was found to be approximately constant across the whole auroral region, this is likely attributed to different electron energies or fluxes rather than a hot polar spot.

These studies, which combine observations from multiple instruments, have shown that orbiting space-based platforms provide excellent platforms from which to perform multispectral studies, revealing the conditions in both the magnetosphere (dynamics and electron energies and fluxes) and the atmosphere (temperatures and densities).

4 X-ray views of the outer planets

X-rays have become very relevant in the context of solar system observations more recently than other spectral bands, and mostly since the turn of the millennium, thanks to the high spatial resolution and the large collecting area of the Chandra and XMM-Newton observatories respectively. Planets, moons and comets have been detected and in some cases have been studied in detail. The significance of the Charge eXchange (CX) process has been realised (e.g. Dennerl 2010; Dennerl et al. 2012), with Solar Wind CX (SWCX) being responsible for the soft X-ray emission in many cases (Mars, Venus, Earth). Below is a review of what we have learnt so far about the X-ray emissions of Jupiter and Saturn, focusing on their aurorae, as well as a look at the many issues opened up by the discoveries, at the many questions still awaiting answers, ending up with some considerations about the other gas giants and future directions.

4.1 Jupiter

4.1.1 First detection and early observations

The first X-ray detection of Jupiter takes us back to the Einstein Observatory: the planet was detected by the Imaging Proportional Counter (IPC) in 1979 and the High Resolution Imager (HRI) in 1981 (Metzger et al. 1983), and already then it was proposed that the emission may be related to energetic ion precipitation. Similarly good fits to the IPC spectra were obtained by a combination of line emission (oxygen, O, and in lower measure sulphur, S) and by electron bremsstrahlung. The luminosity of both aurorae combined (clearly distinguished in the HRI image, see Figure 21) was estimated to be 4 GW (in the energy band 0.15–3 keV). The conclusion was that the electron input power would be too low and the spectral shape too soft for the X-ray emission to be explained by electron bremsstrahlung, and that it was more likely that heavy ion precipitation be the cause of the X-ray aurora (with the X-ray power being produced mostly in the O lines and 40 times less in S). Gehrels and Stone (1983) envisaged a scenario where O and S ions diffuse outward from the Io plasma torus to the middle magnetosphere, where they are accelerated, and then diffuse inward towards the planet. The ions are then scattered into the loss cone and ultimately precipitate into the upper atmosphere, where they slow and undergo radiative transitions - although the transitions were not yet attributed to CX. Waite et al. (1988) expanded this picture to include the results of IUE observations and suggested that, while ions are at the origin of the soft X-ray emission, 10–30 keV electrons are responsible for most of the UV emission, by the excitation of atmospheric hydrogen molecules.

ROSAT observations in the early 1990s confirmed this general picture (Waite et al. 1994). Of particular interest is the brightening of the X-ray aurora observed in the event of comet Shoemaker-Levy 9's plunge into Jupiter (see Figure 22, Waite et al. 1995) possibly triggered by the impact itself or by comet fragments and dust transiting in the inner magnetosphere. Attention was also paid to the equatorial emission apparent in the ROSAT observations (Waite et al. 1997), which was then attributed to ion precipitation as well.

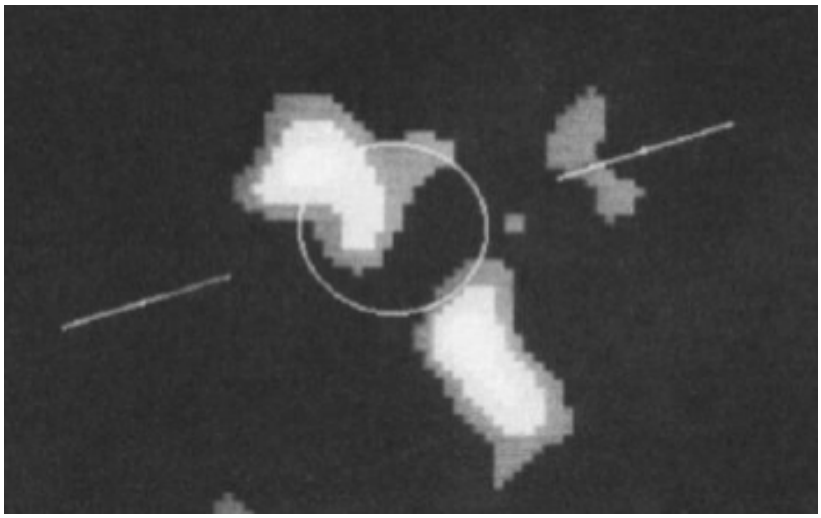

Fig. 21 Einstein Observatory HRI (0.15–3 keV) image of Jupiter, clearly displaying the well separated emissions of the aurorae. The circle outlines the planets disk, and the equatorial plane is indicated by the two linear segments (from Metzger et al. (1983)).

4.1.2 X-ray emission processes

Cravens et al. (1995) were first to explain Jupiter's auroral soft X-ray emissions by Charge Transfer (or CX) of highly charged O ions, while Horanyi et al. (1988) had initially explained the auroral UV emissions by CX of lower charge states of O. A thorough review of the CX process is presented in Dennerl (2010). The process had been studied since the dawn of atomic physics, but was recognized as a very efficient mechanism of X-ray production only when invoked by Cravens (1997) to explain cometary X-ray emission. Basically, energetic highly charged ions (such as O^{7+} or O^{8+}) acquire an electron in the encounter with a neutral atom or a molecule, are left in an excited state and subsequently decay with the emission of characteristic soft X-ray lines (see the cartoon in Figure 23, from Dennerl 2009). This process is now known to be ubiquitous in the universe, and is observed in our solar system, the local interstellar medium, supernova remnants, star forming regions, and starburst galaxies (see the review by Raymond 2012). Within the confines of the solar system SWCX is known to be responsible for the exospheric X-ray emissions of Venus and Mars (Dennerl 2008; Dennerl et al. 2006), and of our own Earth (e.g. Carter et al. 2010). In the case of the soft X-ray emission from Jupiter's aurorae, the origin of the ions has been matter of debate for some time, and currently a magnetospheric origin (i.e. from Io's volcanoes) is preferred, on spectroscopic grounds, over one from the solar wind (see Section 4.1.3).

In addition to CX, a variety of other processes are known to produce X-ray emission from planets and their moons. Recently electron bremsstrahlung has indeed been discovered in the spectra of Jupiters aurorae, at energies (> 2 keV) where CX is no longer the dominant emission mechanism (see Section 4.1.3). Line emission, following electron

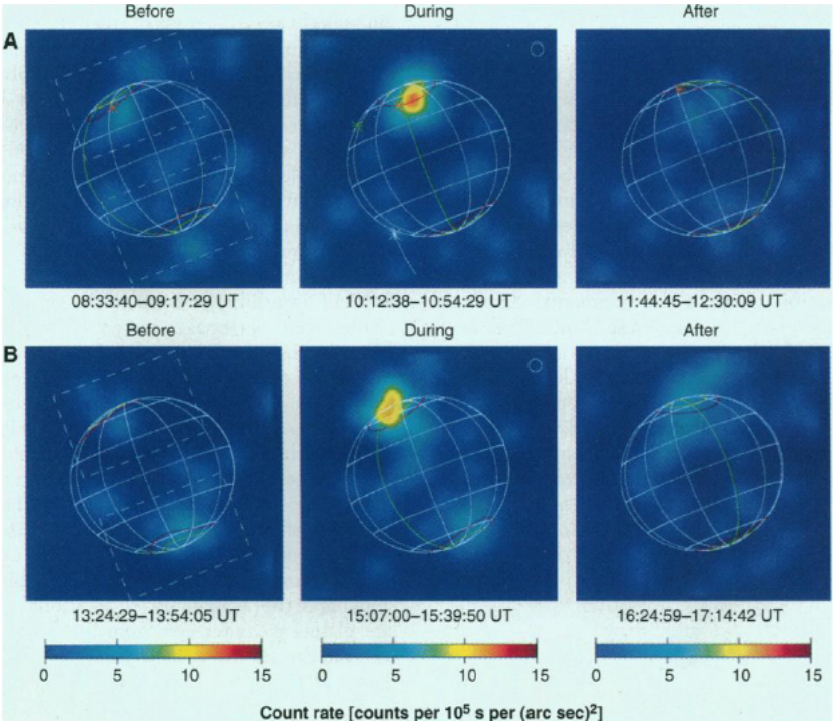

Fig. 22 ROSAT HRI images of Jupiter taken before, during and after the impacts of fragments K (top) and P2 (bottom) of comet Shoemaker-Levy 9 in July 1994. Brightenings of the Northern aurora are clearly seen during the impacts. The latitude-longitude grids show the planets orientation at the mid-point of each exposure (from Waite et al. (1995)).

collisions, is observed, e.g. in the Earth's atmosphere. Elastic and fluorescent scattering of solar X-rays takes place in planetary atmospheres (and on moon surfaces), in such a way that the planetary disks are seen to mirror the solar X-ray variability, on short timescales and over the solar cycle (e.g. Bhardwaj et al. 2005b; Branduardi-Raymont et al. 2010).

4.1.3 Chandra and XMM-Newton reveal spatial, spectral and temporal details

The first observations of Jupiter by Chandra in 2000 (Gladstone et al. 2002) returned very surprising results. While the ions producing X-rays by CX were originally thought to originate in the inner magnetosphere (i.e. Io), polar projections of the Chandra High Resolution Camera (HRC) X-ray photons indicate that the bright spot of auroral emission magnetically maps out to some 30 R_J (Figure 24). This ignited the debate about where the ions are really coming from: inner or outer magnetosphere, Io (thus O and S ions) or solar wind (rich in carbon, C, ions)? Detailed modeling of the two options has been carried out by Cravens et al. (2003). For both scenarios, solar wind and magnetospheric origins, the ions need to undergo acceleration by electric potentials

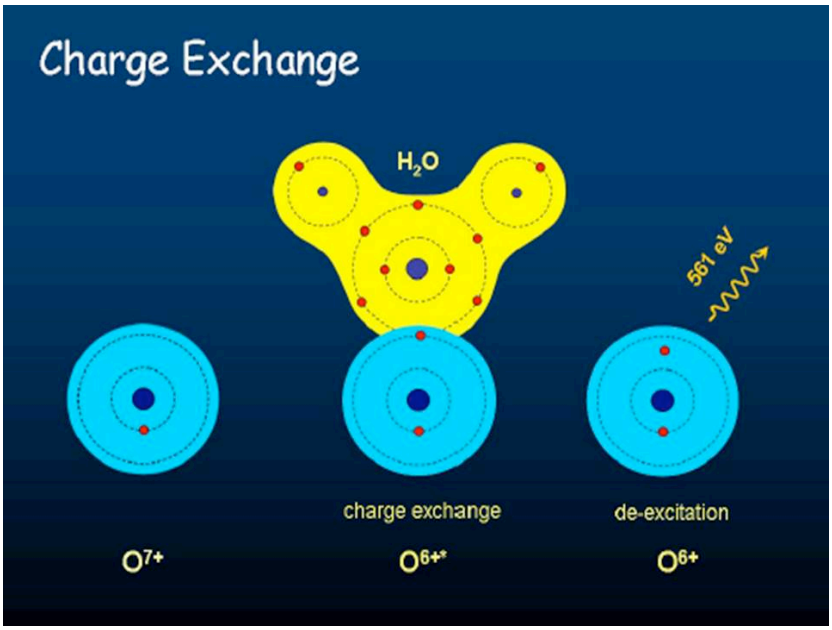

Fig. 23 Cartoon illustrating the CX process in the case of an O^{7+} ion from the solar wind encountering a water molecule of a cometary coma, acquiring an electron, being left in an excited state and emitting an X-ray line (from Dennerl (2009)).

of at least 200 kV for the former, and 8 MV for the latter, in order to be stripped to high charge states, so as to produce sufficient X-ray flux to match the observations.

Even more surprisingly, Gladstone et al. (2002) reported that the flux in the bright spot was pulsating at a period of $\sim$ 45 min (Figure 25), with no correlations to e.g. Cassini upstream solar wind and energetic particle data at the time, although radio bursts, and associated electron bursts, of similar periodicity had been detected in 1992 during the Ulysses fly-by (MacDowall et al. 1993). Such strict periodicity has never again been observed in Jupiter's X-ray aurorae, although chaotic variability, with power peaks in the 20–70 min range, was detected by Chandra in 2003 (Elsner et al. 2005). This change in the character of the variability, from organised to chaotic, may be explained by particle acceleration driven by pulsed reconnection at the dayside magnetopause between magnetospheric and magnetosheath field lines, as suggested by Bunce et al. (2004). The average potentials predicted in their case of solar wind 'fast flow', with high density, high field conditions, are of the order of 100 kV and 5 MV for electrons and ions, respectively.

Further simultaneous Chandra and HST STIS observations in 2003 revealed the interesting occurrence of a strong FUV flare in the north auroral region, temporally coincident with (and spatially adjacent to) a highly significant X-ray brightening (Elsner et al. 2005). This was taken to support the scenario where electrons and ions are simultaneously accelerated in the magnetosphere by strong field-aligned electric fields.

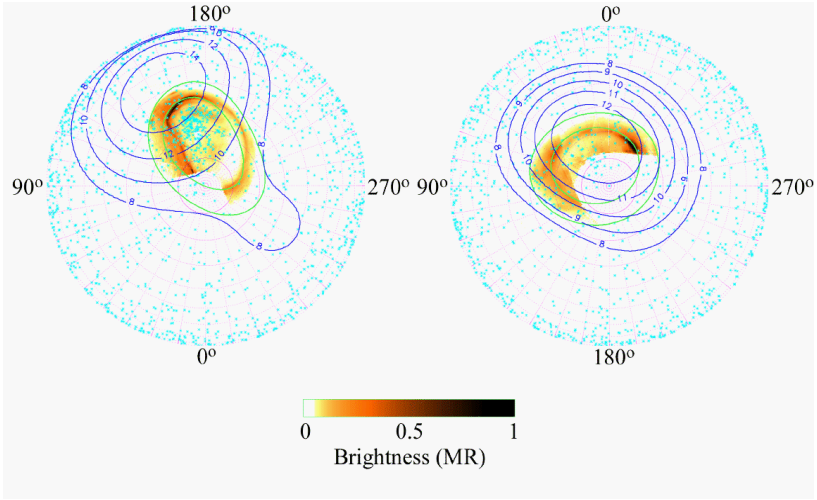

Fig. 24 Polar projections of the X-ray events (light blue dots) observed by the Chandra High Resolution Camera, superposed on the simultaneous UV images (orange) from HST STIS. The green ovals show the footprints of the magnetic lines that map out to 6 and 30 RJ. Clearly most of the Northern aurora X-rays are located well inside the UV oval (from Gladstone et al. (2002)).

The large collecting area of the XMM-Newton telescopes allows the construction of spectral maps of Jupiter's X-ray emission in narrow energy bands and data obtained in 2003 brought about more surprises (Branduardi-Raymont et al. 2007a). First, the spectral maps clearly display the planets different X-ray morphology, dependent on the emission process involved. Those at the top of Figure 26 show (left) CX emission concentrated in the aurorae (using the OVII band centred at 0.57 keV), and (right) scattered solar X-rays (bands centred on the Fe lines around 0.73 and 0.83 keV, typical of solar flares). Unexpected was the detection of auroral emission at higher energies (bottom panels) because CX lines are not present above $\sim$ 2 keV, and at these energies the scattered disk emission has also died off. The spectra extracted for the two auroral regions and the low latitude disk are shown in Figure 27. Below 2 keV the aurorae display the presence of the strong OVII line and evidence for other CX line emission at lower energies, while above $\sim$ 2 keV the spectrum is a featureless continuum, consistent with electron bremsstrahlung. Interestingly, the bremsstrahlung component varied significantly in both flux and spectral shape between the two halves of the XMM-Newton observation, made in late November 2003. This coincided with a period of enhanced solar activity (the 'Halloween storm') when changes in solar wind dynamic pressure may have affected plasma acceleration in the Jovian magnetosphere. The ion CX line emission did not change at the time, possibly because of the much higher level of accelerating potentials required (Bunce et al. 2004).

The soft X-ray spectrum is well modeled by a combination of oxygen emission lines (OVII being the strongest) superposed on a bremsstrahlung continuum which is likely to represent the contribution of more CX line transitions below $\sim$ 0.5 keV. One such

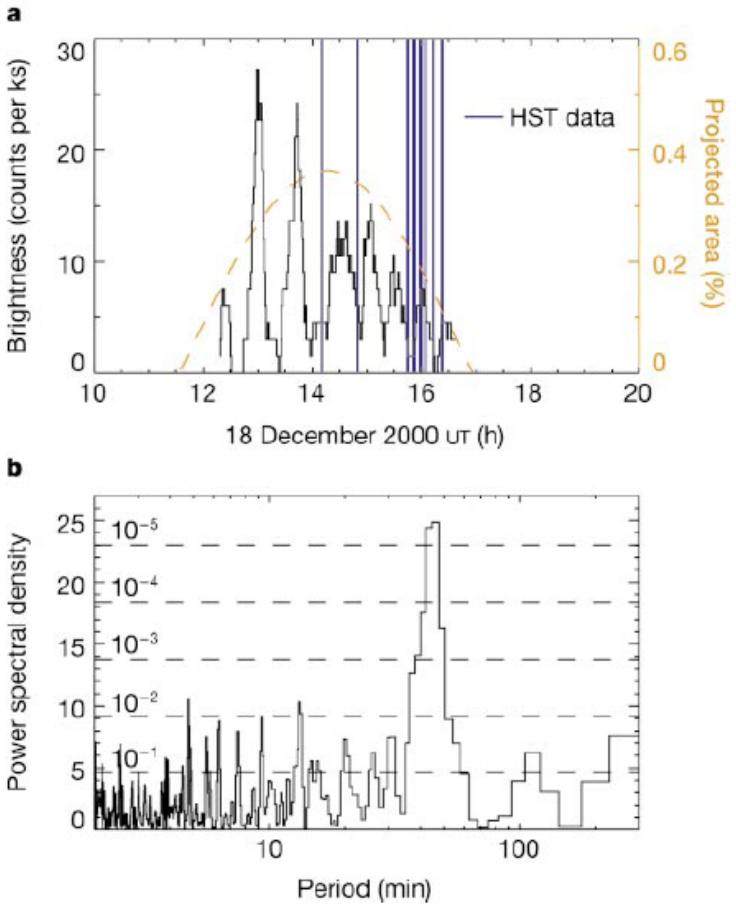

Fig. 25 Light curve (top) and power spectrum (bottom) of the X-ray events from Jupiter's Northern auroral 'hot spot. The $\sim$ 45 min periodicity is clearly seen in the light curve and identified by the peak in the power spectrum (from Gladstone et al. (2002)).

line is resolved at $\sim$ 0.32 keV, however, its attribution to C or S is uncertain because of the relatively large error on the fitted energy, although analysis of all the 2003 XMM-Newton datasets combined suggests a more likely interpretation as SXI (0.32 keV) or SXII (0.34 keV) rather than CVI (0.37 keV) (Branduardi-Raymont et al. 2007a). A preference for S over C line emission (and thus for a magnetospheric origin of the CX ions) is also indicated by Chandra Advanced CCD Imaging Spectrometer (ACIS) data (Hui et al. 2009, 2010a). However, a definitive conclusion on the origin of the ions has not been made. The Reflection Grating Spectrometer, which could easily resolve the S and C lines, does not have enough sensitivity at these energies to detect the lines above the noise. Through its high spectral resolving power, however, it is possible to measure

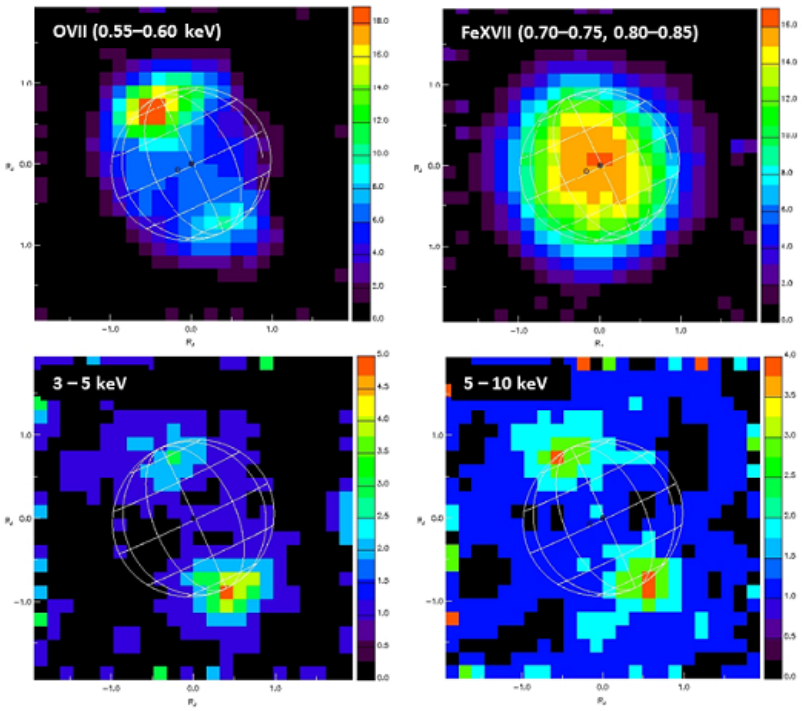

Fig. 26 Jupiter's differing morphology in narrow band X-ray spectral maps centred on the auroral CX OVII line (top left), on the Fe lines characteristic of solar flares (top right), and in higher energy bands where only the auroral emission is visible (XMM-Newton European Photon Imaging Camera data, from Branduardi-Raymont et al. (2007a)).

the Doppler broadening of the CX OVII line, which gives an indication of the velocities and energies of the O ions. These are found to be of the order of 5000 km s^{-1}, or a few MeV, close to the levels predicted by Cravens et al. (2003) and Bunce et al. (2004). During the 2003 Chandra and XMM-Newton observations Jupiter's auroral power was measured to range between 0.4–0.7 GW (in the energy band 0.2–2 keV) and 40–90 MW (2–7 keV) (Branduardi-Raymont et al. 2007a).

The shape and flux level of the bremsstrahlung spectrum, dominating above 2 keV, in the XMM-Newton spectra from the 'quiet' part of the 2003 observation are in remarkable agreement with predictions by Singhal et al. (1992) for electron energies of few tens of keV (Branduardi-Raymont et al. 2007a). For completeness it is worth mentioning that the spectrum from the low latitude disk (see Figure 27) is well represented by an optically thin coronal model with a temperature of $\sim$ 0.4 keV, which confirms the idea that the X-rays originate from scattered solar emission (see also Branduardi-Raymont et al. (2007b)).

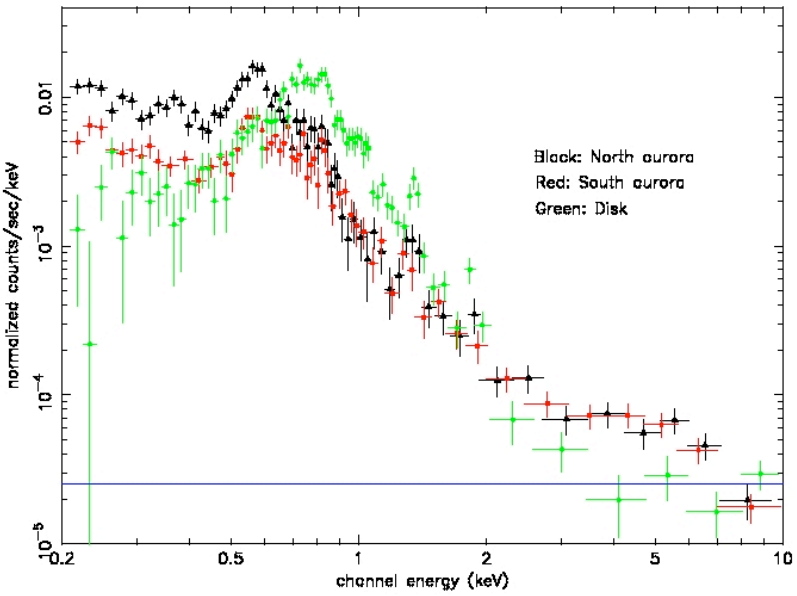

Fig. 27 XMM-Newton spectra of Jupiter's North and South aurorae, and of the low latitude disk: the OVII CX emission line at 0.57 keV is very prominent in the auroral spectra; the disk emission is harder and has the characteristics of an optically thin coronal spectrum; the electron bremsstrahlung component of the aurorae dominates above $\sim$ 2 keV (from Branduardi-Raymont et al. (2007a)).

4.1.4 Auroral morphology in simultaneous Chandra and HST STIS observations

The great value of truly simultaneous observations in different energy bands was demonstrated by a study of the different morphology of the jovian X-ray and FUV auroral emissions (Branduardi-Raymont et al. 2008). Figure 28 shows the superposition of X-ray events detected by Chandra ACIS (each small green dot corresponds to a $<$ 2 keV photon, and each big dot to a photon of $>$ 2 keV energy) over the FUV emission (in orange) detected in simultaneous HST STIS observations. Note that the exposure time for the FUV image shown was 100 s while the X-ray photons shown were accumulated over approximately one jovian rotation. Clearly the $>$ 2 keV X-rays (from electron bremsstrahlung) fall coincident with the bright auroral oval and regions of enhanced FUV emission, while those of $<$ 2 keV energy (ionic CX) fall inside the oval (as we knew already from the HRC, which maps them out to $>$ 30 R_J away from the planet). Given that the FUV emission is expected to originate from excitation of atmospheric H_2 molecules and H atoms by 10–100 keV electrons, it is natural to make the connection that the same electron population is responsible for both the hard X-ray and FUV emissions. Also, the fluxes in the two bands are in line with this picture, being within a factor of 10 of the ratio of 10^{-5} predicted by Singhal et al. (1992).

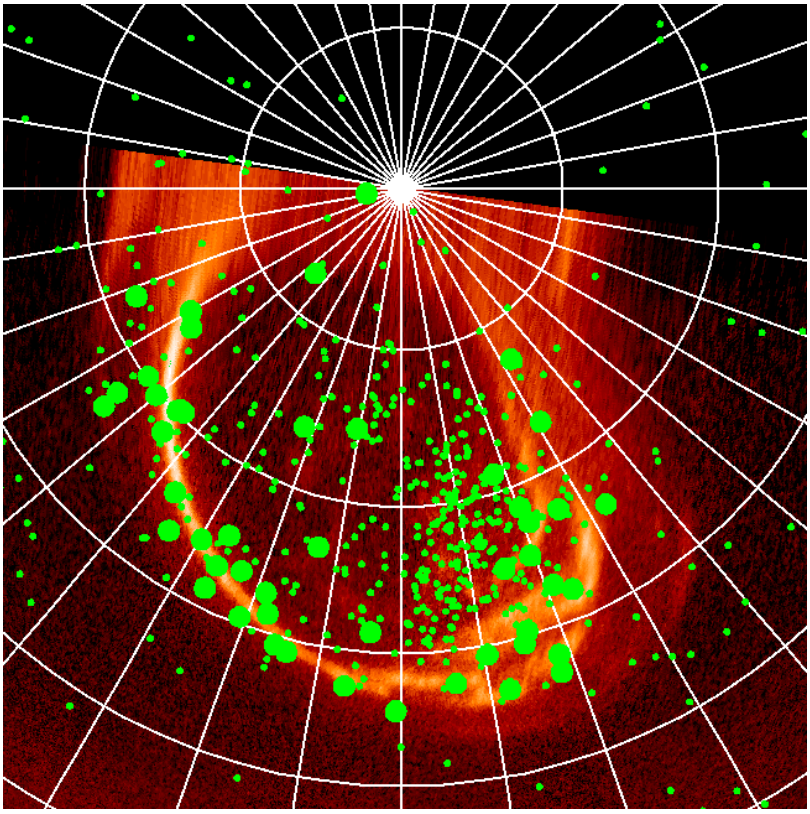

Fig. 28 Superposition of Chandra ACIS X-ray events (large green dots: > 2 keV; small green dots: < 2 keV) on the FUV emission (orange) observed with HST STIS. The footprints of the hard X-rays, expected to be of electron bremsstrahlung origin, coincide with the auroral oval and bright FUV features, indicating that the same electrons are most likely to produce both, X-ray and FUV emissions (from Branduardi-Raymont et al. (2008)).

4.1.5 The Galilean satellites, the Io Plasma Torus and Jupiter's radiation belts

The detection by Chandra of Jupiter's Galilean satellites Io, Europa and possibly Ganymede (Elsner et al. 2002) has been interpreted, on flux grounds, as evidence for fluorescence scattering on their surfaces of energetic H, O and S ions, probably originating from the Io Plasma Torus (IPT). The X-ray emission of the IPT itself, also clearly detected by Chandra, is made up of a very soft continuum, a large fraction of which could be due to non-thermal electron bremsstrahlung, and a single spectral feature, a line at ~ 0.57 keV; the origin of this is unclear because neither fluorescence of solar X-rays nor CX can produce the observed flux.

Finally, diffuse hard (1–5 keV) X-ray emission from around Jupiter, reported recently on the basis of a deep Suzaku observation (Ezoe et al. 2010), has been attributed to non-thermal electrons in the radiation belts and the IPT. However, synchrotron and

bremsstrahlung processes cannot explain it on energetic and spectral grounds, and the energetic electron density required to produce the X-rays by inverse Compton scattering of solar photons is an order of magnitude larger than that estimated from an empirical model of the charge particle distribution around Jupiter (assuming the emission is truly diffuse and not the integrated emission of background sources).

4.1.6 Open questions

While in the last decade of Chandra and XMM-Newton observations we have learnt a great amount about the X-ray properties of the Jovian system, many questions have also been raised, as it always happens when we open a new exploration window on the Universe.

Despite the spectral evidence in favour of a magnetospheric origin of the ions undergoing CX and producing the soft X-rays in Jupiter's aurorae, it is worth considering whether there is still a role for SWCX, and if so, what fraction of the emission may be due to it. On the one hand, while mentioning that SWCX may contribute, Cravens et al. (2003) point out that, in this case, bright UV proton auroral emission would also be expected, but is not seen, thus excluding a pure SWCX scenario. On the other hand, since the ion fluxes in the outer magnetosphere are insufficient to explain the observed auroral X-ray emission, another ion source (possibly the solar wind) may be contributing. If the $\sim$ 45 min periodicity observed by Chandra is an analogue of the quasi-periodic radio bursts reported by MacDowall et al. (1993), the phenomenon may be under solar wind control, as the bursts were reported to be. Bunce et al. (2004) suggest that pulsed reconnection phenomena should be more intense under high density solar wind conditions, when the magnetosphere is compressed, so this could be used as evidence for the ions origin. Alternatively, Cravens et al. (2003) note that if the pulsations have a 'particle bounce' origin this would imply a magnetospheric scenario, unrelated to the solar wind. The rare occurrence of the pulsations may hold a clue and if a new detection were to be made, correlation with the solar wind conditions at the time would add decisive information. Could the ions be precipitating directly from the solar wind? The X-ray hot spot location (Gladstone et al. 2002) lying in the vicinity of the Jovian cusps would support this possibility, although acceleration is still required to explain the X-ray fluxes observed. How do the timescales of ion and electron precipitation compare? Only further simultaneous studies of the UV and X-ray emissions can help to take this further.

An opportunity to advance this quest is offered by the JAXA Sprint-A mission, launched in September 2013 with the Hisaki EUV spectrograph on-board, and dedicated to the study of the tenuous plasma surrounding planets in our solar system. The primary target is Jupiter, and the emission from the IPT in particular. The aim is to explore the possible links between the IPT emission distribution, the strength and character of Jupiter's auroral emissions and the conditions of the solar wind. Concurrently with the Hisaki observations, a large multi-wavelength campaign, including X-ray observations, has been organised to gather important diagnostic data on the complex array of physical processes that operate in Jupiter's environment. Some answers may well come from this endeavour, for example, examination of the energetics of the particles in the IPT should help establish what mechanism leads to its OVII line emission.

Other questions, still wide open, concern the comparison between north and south X-ray aurorae in flux, temporal variability and spectrum, and also Io and its footprint:

is there an X-ray equivalent, which has not yet been detected? Finally, given the known presence of a magnetosphere and auroral emissions associated with Ganymede, one can also speculate whether there may be a magnetospheric component in the X-ray emissions of the Galilean moons. Only more sensitive and higher duty cycle observations will be able to shed light on this. However, the difficulty of realizing them with an Earth orbiting X-ray observatory leads to the conclusion that a much more effective option is to have X-ray observations in situ at the planets, incorporating X-ray instrumentation in future planetary missions.

4.2 Saturn

4.2.1 Disk X-ray emission under solar control: No X-ray aurorae?

By analogy with Jupiter, X-ray aurorae powered by CX could also be expected on Saturn, yet none have been observed so far. The disk and polar cap have similar coronal-type spectra ($kT \sim 0.5$ keV averaged over the years) and the disk flux variability strictly correlates with that of solar X-rays, demonstrating that the planet's X-ray emission is controlled by the Sun (Bhardwaj et al. 2005a; Branduardi-Raymont et al. 2010). This is clearly illustrated by Figure 29, which compares the view of Saturn in two Chandra observations separated by about a week; the planet was brighter by a factor of 3 during the first observation, coincident (after correction for light travel times) with a strong flare going off on the Sun (Bhardwaj et al. 2005a).

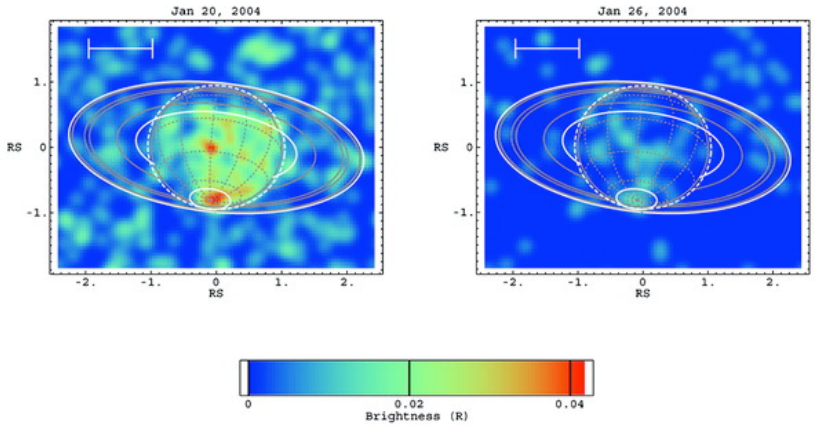

Fig. 29 Chandra images of Saturn taken one week apart in Jan 2004, showing how the disk X-ray emission was brighter in the first observation, at the time when X-rays from a strong solar flare reached the planet. The enhancement at the south pole shows the same spectral character of the rest of the planet's disk and is not evidence of an X-ray aurora (from Bhardwaj et al. (2005a)).

UV and radio brightenings of Saturn's aurora have been found to correlate with the arrival of solar wind shocks at the planet (Clarke et al. 2009), suggesting that solar wind ions may also have a role in producing X-ray aurorae by CX. In this case, as shown by Cravens (2000), the emitted power is proportional to both the density and speed of the solar wind, thus the passage of a solar wind shock at the planet may produce an X-ray auroral brightening. Theoretical estimates of Saturn's auroral fluxes (Hui et al. 2010b) for un-accelerated solar wind ions are within a factor of a few of the sensitivity of current instrumentation, although acceleration of the ions in the planet's magnetic field would raise these estimates. Chandra observations were obtained in 2011 (Branduardi-Raymont et al. 2013), triggered by the expected arrival of solar wind shocks that had been propagated from measurements at 1 AU using the 1-D MHD code mSWiM (Zieger and Hansen 2008). Variability in Saturn's X-ray emission was observed, but once again it was due to a flare in the solar X-rays scattered by the planet's atmosphere. Stringent upper limits of 2 MW (photon energies of 0.3–2 keV) and 17 MW (2–8 keV) were derived on Saturn's auroral emissions, excluding the presence of accelerating potentials down to $\sim$ 10 kV. Upper limits of 4 MW were also set on X-rays from each of Titan and Enceladus.

A by-product of these triggered Chandra observations was also a validation of the solar wind propagation technique. At the time, Cassini was crossing Saturn's magnetopause and bow shock as identified in the Cassini magnetometer and electron data. The standoff distances of the boundaries inferred from the in situ measurements were compared with those derived from the propagations. Measurements and propagations were matched by shifting the propagations by +1.9 days, which is consistent in magnitude and direction with the shifts established by Clarke et al. (2009). During the period covered by the 2011 Chandra observations Cassini radio data (RPWS) also showed a strong enhancement, indicating a compression of the magnetosphere (Branduardi-Raymont et al. 2013).

4.2.2 X-rays from Saturn's rings

Chandra has also revealed X-ray emission from Saturn's rings. The spectrum is dominated by a single line centred at 0.53 keV, indicative of atomic O Kα fluorescence, most likely the result of excitation of the oxygen trapped in the icy water particles making up the rings. Bhardwaj et al. (2005c) suggested that this may be due to solar X-ray illumination, however, the apparent lack of correlation with solar activity over the years may point to an alternative explanation, such as electron injections linked to the planet's thunderstorms (Branduardi-Raymont et al. 2010). More observations at high angular resolution (only Chandra can spatially separate ring from disk emission) are needed to search systematically for correlations with solar activity and/or planetary seasons.

4.2.3 Open questions

The X-ray exploration of Saturn, and thus our understanding of its workings, is clearly less advanced than that of Jupiter. Is there really no X-ray aurora on Saturn? The conclusion from the searches made so far is that much more dramatic solar wind enhancements than those used to trigger the Chandra observations in 2011 may be needed if we are to make a detection, and/or much more sensitive instrumentation. Could an

alternative ion source, internal to the kronian system, e.g. Enceladus, contribute an element of CX? Are Titan, as it moves in and out of the solar wind, and Enceladus, with its active cryo-volcanoes, X-ray sources, and by which mechanism? Their environment and physical conditions would be favourable to ionic CX, particle precipitation and fluorescence. Is there a link between the emissions from Saturn and its rings? These are all fascinating issues, which unfortunately are most likely to remain unsolved until we take a major step up in our experimental capability.

4.3 Uranus and Neptune

Detection of X-ray aurorae at Uranus and Neptune is hampered by their vast distances and by the conditions of their environments. By making a comparison with Jupiter and assuming a simple scaling law for the planetary parameters most relevant to X-ray auroral production, such as dipole magnetic moment and magnetospheric particle density, it is clear that any emissions would be well below detectability with current instrumentation, unless some other physical factor were to provide an unexpected contribution. For example, the very large tilt angle (59°) between the magnetic dipole and rotation axes of Uranus, and the 30% offset of the dipole from the centre of the planet, with the consequent order of magnitude difference in surface magnetic field between day- and night-side, might have the effect of enhancing the auroral power above that expected from the simple extrapolation (Branduardi-Raymont et al. 2010).

4.4 Conclusions

With XMM-Newton and Chandra, planetary science has acquired a new observing regime which has revealed many unexpected sides of our solar system, and has led to many new questions. Planetary X-ray astronomy has come of age, and now unexpected discoveries must be turned into fully understood physics. Real progress can only be made by recognizing the high potential of X-ray observing, and by offering X-ray instrumentation the same platform as more traditional wavebands have enjoyed for decades, that which allows in situ measurements. This will bring about higher sensitivity and spatial resolution, together with the improved spectral resolving power of the most modern imaging devices. Recent developments in lightweight optics show that a low-requirement (mass, power, data rates) X-ray telescope for planetary exploration is a feasible proposition. It would also work in great synergy with in situ UV and particle instrumentation, contributing to establish the dynamics and energetics of the particles populating planetary environments, and would validate and test the consistency of models developed from more 'traditional' measurement techniques. On the other hand, remote global X-ray observations at much higher sensitivity and spectral resolving power than afforded by XMM-Newton and Chandra are now forthcoming following ESA's recent selection of the science theme 'The Hot and Energetic Universe' for its next large mission, which would be addressed by the proposed Athena mission. The non-dispersive character of the planned cryogenic spectrometer will enable Jupiter's auroral and scattered solar emissions, as well as the Io Plasma Torus, to be individually mapped spatially and spectrally at high resolution. The search for auroral X-ray emissions on Saturn, as well as attempts to detect Uranus and Neptune, will be pushed

to much fainter flux limits than currently possible. X-ray spectra of the Galilean satellites, and (speculatively) Saturn's moons, will enable the search for magnetospheric emission components, as well as allowing surface composition analysis by fluorescence.

5 Jupiter and Saturn magnetospheric dynamics: a diagnosis from radio emissions

In this section, we will characterise the spectral and spatial properties of jovian and kronian auroral radio emissions and detail the rich diagnosis they bring on internally-driven (magnetodisc, planet-satellite interactions) compared to externally-driven (solar wind) magnetospheric dynamics.

5.1 Spectral and spatial properties of auroral radio emissions

5.1.1 Historical context

All the explored magnetized planets are powerful radio sources at frequencies ranging from a few kHz to a few tens of MHz (Figure 30). Among these, only the decametric emission (DAM) of Jupiter, the frequency of which exceeds the terrestrial ionospheric cutoff (∼10 MHz), can be observed from the ground. Jovian DAM emissions were first detected in 1955 (Burke and Franklin 1955), while the terrestrial kilometric radiation (TKR) was later discovered by observations from space in the 1960s, and investigated in detail by numerous in situ auroral orbiters in the following decades (such as Freja, Viking, FAST). The exploration of the solar system by the Voyager (1980s) and Ulysses (1990s) spacecraft, completed by that of the jovian magnetosphere with Galileo (2000s), later revealed hectometric (HOM) and kilometric (KOM) components of emissions at Jupiter, and kilometric emissions at Saturn (SKR), Uranus (UKR) and Neptune (NKR). The reader is referred to post-Galileo comparative reviews for more information (Zarka 1998, 2004, and refs therein).

Hereafter, we focus on radio emissions radiated by the auroral regions and planet-moon flux tubes of Jupiter and Saturn's magnetospheres, which are the brightest radio emitters of the solar system. These emissions reduce to free-space electromagnetic waves propagating on extraordinary (X) and ordinary (O) modes. We therefore exclude other types of emissions such as low frequency continuum, trapped Z-mode or whistler-mode radiation (narrowband emissions, auroral hiss), electrostatic waves or atmospheric emissions (lightning).

5.1.2 Properties of radiated waves

Jupiter and Saturn display characteristic remote properties, more generally common to all auroral planetary radio emissions, which can be summarised as:

- very intense non-thermal radiation (∼10^{11} W radiated by Jupiter, ∼10^9 W by Saturn), predominantly in the X mode;
- instantaneous emission at $f \sim f_{ce}$ (f_{ce} is the electron gyrofrequency);
- sources along high latitude magnetic field lines, hosting energetic (keV) electrons, and co-located with atmospheric aurorae, where $f_{pe} << f_{ce}$ (f_{pe} is the electron plasma frequency);

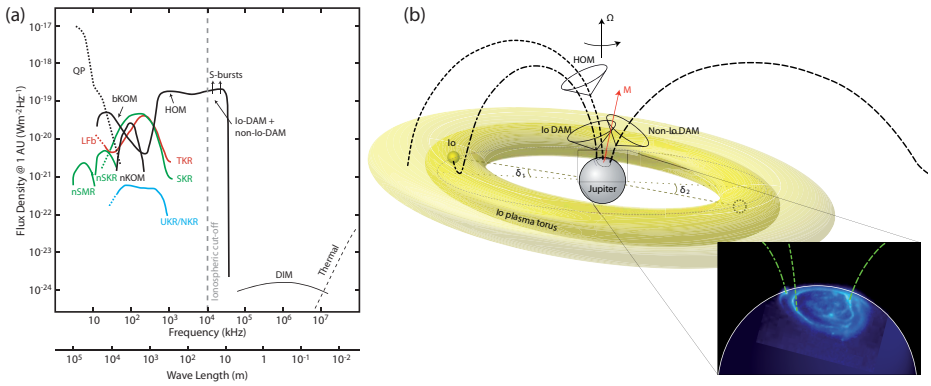

Fig. 30 (a) Average spectra of known planetary radio emissions, adapted from Cecconi (2010). (b) Expected locus of jovian radio sources, adapted from Cecconi et al. (2012).

– 100% circular or elliptical polarization (the sign of which indicates the magnetic hemisphere of origin);
– very anisotropic beaming (thin conical sheet) leading to strong visibility effects;
– sensitivity to magnetospheric dynamics at relevant timescales (e.g. planetary rotation, orbit of moons, solar wind activity).

In situ measurements within the terrestrial auroral regions led to the identification of the Cyclotron Maser Instability (CMI) as the driver of the TKR emission (Wu and Lee 1979; Wu 1985; Treumann 2000, 2006, and refs therein). This mechanism operates in regions where $f_{pe} << f_{ce}$ as a resonant wave-particle interaction between non-maxwellian electrons gyrating around magnetic field lines and a background of radio waves. These are amplified close to f_{ce} at the expense of the electron (perpendicular) energy. This free energy may come from loss-cone, ring or shell electron distributions, which all yield positive growth rates (Roux et al. 1993; Louarn and Le Quéau 1996; Delory et al. 1998; Ergun et al. 2000), with slightly different wave properties in terms of emission frequency (above/below f_{ce}) or emission angle relative to the magnetic field (*i.e.* the wave beaming). Efficient amplification additionally requires the size of the source region to exceed several times the wavelength. The local conversion efficiency from the total (perpendicular) electron free energy to X mode wave energy can reach ∼1% (Benson and Calvert 1979).

As Jupiter and Saturn auroral radio waves display remote properties consistent with CMI, this mechanism was postulated to be a universal generation process common to all magnetized planets (Zarka 1992). This hypothesis could recently be validated for Saturn with Cassini in situ measurements within the SKR source region (Lamy et al. 2010; Mutel et al. 2010; Schippers et al. 2011; Menietti et al. 2011), yielding a 1% (2% peak) electron-to-wave energy conversion efficiency (Lamy et al. 2011). The JUNO mission will specifically investigate this and other properties of the jovian auroral regions in the coming decade.

5.1.3 Diagnosis

The understanding of the generation mechanism and the subsequent remote properties of radiated waves provide a powerful diagnosis of the nature and the dynamics of the

underlying coupling between the solar wind, the magnetosphere, the moons, and the ionosphere at the origin of these emissions.

Spectral and spatial properties are intrinsically related because the emission frequency f is limited by the electron gyrofrequency f_{ce}, itself linearly proportional to the magnetic field. The emission frequency f therefore directly indicates the altitude of the source above the ionosphere. This allows one to instantaneously locate the radio sources and to track possible motions throughout the auroral regions. The detected emission also indicates a source region fulfilling CMI requirements with $f_{pe} << f_{ce}$ and energetic electrons whose distribution is unstable (shell, ring, loss cone). The main advantage of radio observations relies on the capability for long-term, quasi-continuous, remote measurements at high spectral and temporal resolution. The Poynting flux, organized in time-frequency (dynamic) spectra, provides essential information on the auroral activity. Beyond pioneering analysis of the most obvious variations (rotational or moon-induced modulation, solar wind forcing), a refined interpretation of dynamic spectra, focused on shorter sub-structures, has been the subject of recent modeling studies.

In parallel, higher level observables, such as the wave polarization (Stokes parameters), and/or the position of radio sources, can be retrieved with sophisticated instrumentation and data processing techniques, either space-based (goniopolarimetry, Cecconi 2010) or ground-based (LOFAR phased array). The wave polarization reveals several important parameters: the sense of circular polarization depends on the hemisphere of origin, while the quantitative degree of polarization depends on the magneto-ionic propagation mode and the degree of wave-plasma coupling along the ray path. The position of radio sources enables one to perform radio imaging and to map active field lines in real time.

The use of such observables to investigate the jovian and kronian magnetospheric dynamics are illustrated through several examples below.

5.2 Jupiter

Jupiter's auroral radio emissions are divided between Io (the most intense) and non-Io emissions, regularly observed from the ground above 10 MHz since the 1950s, and at low frequencies from space with Voyager/Ulysses/Galileo, or more recently with Cassini and STEREO. All these emissions are strongly modulated at the planet rotation period (9 h 55 min), as a result of the magnetic dipole tilt.

5.2.1 Io-Jupiter: the case for moon-planet interactions

The Io-Jupiter interaction is due to the motion of Io relative to the jovian magnetic field, which generates an electric current closing in the jovian ionosphere (Neubauer 1980). This electrodynamic coupling was the first discovered and is the most powerful case of satellite-magnetosphere interactions. It thus stands as the archetype of such interactions (4 cases confirmed so far: Io, Europa, Ganymede and Enceladus), and, by a small extension, rapidly moving interacting regions (Hess et al. 2011a). The most prominent feature of the Io-related radio emissions is their well-defined arc shape observed in the time-frequency plane at timescales of hours. Sub-structures include the well known jovian S-bursts at timescales of milliseconds.

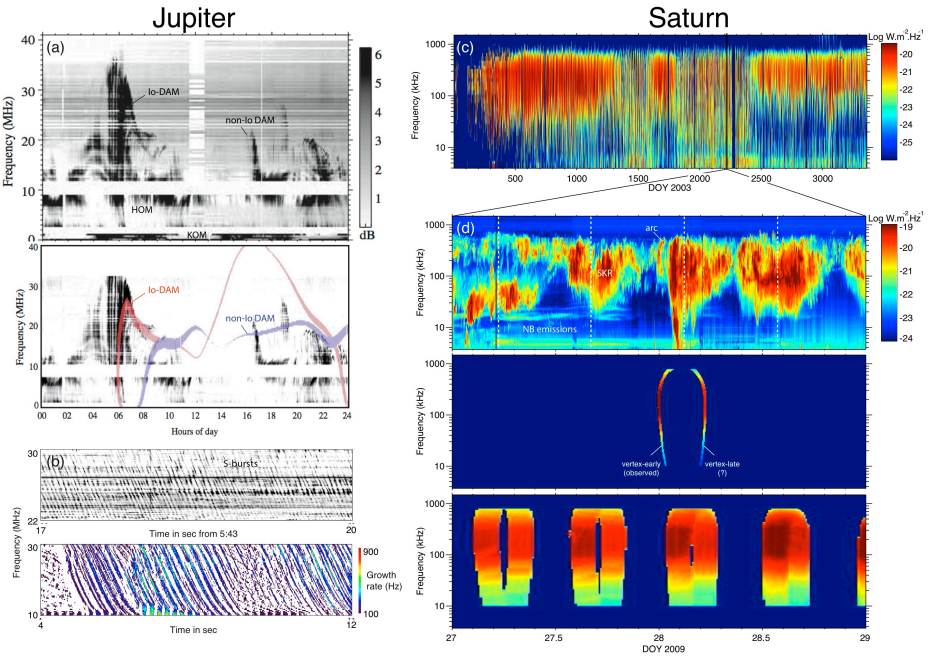

Fig. 31 Observed and modelled radio emissions of (left) Jupiter and (right) Saturn. (a) Voyager 2/PRA observations of the jovian auroral radio emissions on 16 July 1979 (top) and simulations of Io and non-Io DAM arcs (bottom), adapted from (Cecconi et al. 2012). (b) Nançay/NDA observations of jovian S-bursts over a few seconds of april 1995 (top) and associated simulations (bottom), adapted from (Hess et al. 2009). (c) Cassini/RPWS observations of SKR from 2003 to 2012, adapted from (Kimura et al. 2013). (d) Cassini/RPWS observations of SKR from 27 to 28 January (top panel) and simulations of the rotational modulation (middle panel) and of a sub-corotating arc (bottom panel), adapted from Lamy et al. (2013).

5.2.1.1 Radio arcs Arc-shaped emissions are primarily due to the small spatial size of the interaction region (i.e. Io). A more extended interaction region would generate a continuous suite of arcs and form a continuum of radio emission. The arc shape is then a direct consequence of the anisotropy of the emission pattern of individual radio sources, which is a thin ($\sim 1^\circ$ wide) conical sheet with a wide opening angle relative to the magnetic field vector. The source is detected only when the observer crosses the cone sheet, so it can be seen at most twice by a fixed observer as the source rotates with the planet, even though it emits continuously. The time delay between these two observations depends on the cone opening angle and on the observer's motion relative to the source.

Although the arc shape was explained a long time ago, its use as a diagnostic of the interaction parameters is quite recent. Hess et al. (2008) computed the theoretical opening of the emission cone and showed that, apart from the altitude, it mostly depended on (1) the electron distribution function, (2) the emitting electron energy and (3) the plasma parameters determining the refraction index (Ray and Hess 2008; Mottez et al. 2010). The morphology of radio arcs permits the diagnosis of the current system powering the emission, as different current systems lead to different beamings. Shell driven emission with nearly constant emission angles are obtained in auroral cavities for steady-state systems, whereas loss-cone driven CMI with an emission angle

rapidly decreasing close to the planet are obtained for transient currents (Mottez et al. 2010).

The Io-related current system is Alfvénic (Crary 1997; Hess et al. 2008; Hess et al. 2010), in accordance with our knowledge of the Io-Jupiter interaction (Neubauer 1980). A numerical model called ExPRES (Hess et al. 2008) has been developed for extended simulation studies. It takes into account both the physical parameters of the interaction, to compute the beaming angle, and the geometry of an observation, to ultimately compute simulated dynamic spectra of the emissions. The fit of the simulated dynamic spectra to observational data allowed Hess et al. (2010) to measure the variation of the electron energy with Io's System III longitude.

5.2.1.2 Fine structures Fine structures, called millisecond or short (S-)bursts, are very common. They have a short duration ($\sim$ 10 ms at a given frequency) and drift in frequency with time. The emission frequency is close to f_{ce}, and thus relates to the source altitude, therefore this drift is the result of the source motion along magnetic field lines.

Zarka et al. (1996) and Hess et al. (2007) measured the drift rate versus frequency and showed that the source motion was generally consistent with the adiabatic motion of electrons moving away from Jupiter, which allows one to measure the emitting electron energy from the measurements of the drift rate. These authors showed that the electrons have an energy between 2 and 5 keV which appears to vary as a function of Io's system III longitude.

Hess et al. (2007) also detected localized jumps of the electron kinetic energy, interpreted as a localized electron acceleration due to localized electric potential drops. Hess et al. (2009) showed that these potential drops are actually moving away at the local ion acoustic velocity, and thus are probably solitary ion acoustic waves.

Finally, Hess et al. (2007) simulated dynamic spectra of the radio emissions induced by electrons accelerated by periodic Alfvén waves (see Figure 31b). These are similar to the observed dynamic spectra of the S-bursts, validating Alfvén waves as the primary source of electron acceleration in the Io-Jupiter interaction.

5.2.2 Non-Io emissions and rotational dynamics

The origin of most of the non-Io emissions often remains a mystery as only the narrow-band kilometric (nKOM) emission sources have been clearly identified as being plasma wave generated on the borders of the Io plasma torus (Reiner et al. 1993b).

Direction-finding studies using Ulysses observations (Reiner et al. 1993a; Ladreiter et al. 1994) concluded that part of the hectometric (HOM) emissions occurs along field lines mapping to regions between 4 and 10 R_J, i.e. in the extended Io torus. In the decameter range, Panchenko et al. (2013) observed radio arcs resembling Io's in sub-corotation with the same period as that observed by Steffl et al. (2006) in the torus, and interpreted as the beating of the System III (internal) and IV (torus perturbations) periods. The beating originates from a peak of the hot electron population density near 290° of longitude (Steffl et al. 2008) caused by an Io-like interaction powered by empty flux tubes moving inward in the torus (Hess et al. 2011a). The Io-like decameter arcs observed by Panchenko et al. (2013) could be related to an Io-like interaction powered by the interchange instability in the torus and the HOM emissions located by Ulysses may be their lower frequency counterpart.

The dynamic spectra of the Jovian emissions often exhibit slowly drifting bands in which the background emissions are alternately enhanced and dimmed. These bands (so-called modulation lanes) are due to flux tubes with densities differing from their environment and acting as a diffracting grating (Imai et al. 1997). Io-related (localized) background emissions permit one to locate the position of these flux tubes in a region between the orbits of Amalthea and Europa (Arkhypov and Rucker 2007). Refraction undergone in the equatorial torus is responsible for attenuated lanes in the HOM range (Gurnett et al. 1998; Menietti et al. 2003).

Intense non-Io arcs have also been observed in the Jovian magnetosphere by STEREO (Lamy et al. 2012) and simultaneously by the Nançay decametric array, Cassini, and Galileo (Hess et al. submitted). Their corotation rate, close to $\sim 100\%$, indicates that their source is in the inner or middle magnetosphere, although their intensity seems to be modulated by the solar wind conditions.

Less structured emissions exist for which the decametric emissions mostly originate from the dusk side (from the Voyager 1 flyby Barrow 1981; Hess et al. 2012), and extend deeply into the hectometric and kilometric ranges (e.g. Cassini observations in Hess et al. submitted). The low sub-corotation rates of these radio sources (down to 50%) indicates that the interaction powering these emissions occurs in the outer magnetosphere. UV and infrared observations show that the poleward (probably solar wind related) aurorae are also mostly emitted on the dusk side, thus the latter radio emissions may also be caused by the magnetosphere-solar wind interaction (Grodent et al. 2003b). Quasi-periodic kilometric bursts are also observed pulsating with a quasi-period of about 40 minutes. Their origin seems to be among the most poleward of all radio emissions (Kimura et al. 2011).

5.2.3 Solar wind control

Jupiter's outer magnetosphere is sensitive to variations of the solar wind dynamic pressure (e.g. Smith et al. 1978), but the relation between Jupiter auroral emissions and the solar wind pressure is complex and only some of the radio components are sensitive to it. Several observations have shown that auroral emissions are enhanced during times of higher solar wind pressure (Barrow 1978; Zarka and Genova 1983; Genova et al. 1987) or are triggered by interplanetary shocks (Barrow 1979; Terasawa et al. 1978; Prangé et al. 1996, 2004; Gurnett et al. 2002; Clarke et al. 2009).

Hess et al. (2013) compared Nançay observations of non-Io emissions to solar wind parameters (magnetic field, velocity and density) propagated from Earth to Jupiter. They found that fast reverse shocks generated dawn and dusk radio emissions, whereas forward shocks generate emissions from dusk only which may later move toward the dawn side. A multi-spacecraft study of the Jovian radio emissions during Cassini's approach to the planet (Hess et al. submitted) confirmed those results and additionally showed that the corotation rate of these radio source (usually about 50%) increased to more than 80% for strong magnetospheric compressions.

5.3 Saturn

Saturn's kilometric radiation, discovered during the Voyager flyby of Saturn in 1980 (Kaiser et al. 1980, 1984), has been observed by only two spacecraft since then, Ulysses in the 1990s and Cassini, in orbit since mid-2004. Further details on SKR average

properties can be found in Kaiser et al. (1984); Lamy et al. (2008b) and refs therein. These observations revealed that SKR is subject to significant variations at various timescales.

5.3.1 Rotational dynamics

5.3.1.1 Rotational modulation The most obvious SKR temporal variation is its strong, regular, rotational modulation at ∼11h, which reveals the prominent role of the fast planetary rotation on magnetospheric dynamics. The modulation of northern SKR discovered by Voyager was interpreted as the result of strobe-like intense flashes emitted by radio sources fixed in local time (Desch and Kaiser 1981; Kaiser et al. 1981). The dawnside location of the latter was indirectly inferred from visibility considerations (Galopeau et al. 1995, and refs therein). Similarly to other planets, this radio period was taken as a direct measurement of the inner rotation period. However, in the absence of any measurable tilt between the magnetic and rotation axis, the origin of the modulation itself remained unexplained.

Further distant observations by Ulysses surprisingly revealed that the SKR period, measured alternately from the southern and northern hemispheres, varies with time, at a level of ∼1% over several years (Galopeau and Lecacheux 2000). This result definitely precluded the observed radio period from providing the internal rotation rate, and raised the additional question of the origin of a period varying over long timescales.

The quasi-continuous observations by Cassini since 2004, equipped with a sophisticated radio experiment, brought a set of important results to light. Thanks to long-term time series, Zarka et al. (2007) identified weekly modulations of the southern SKR period during the pre-orbit insertion interval (subject to little visibility effect). A positive correlation with variations of the solar wind speed suggested an external control of the period's variation. Investigating yearly variations, Gurnett et al. (2009, 2010b, and refs therein) showed that SKR is modulated at (slightly) different periods in southern and northern hemispheres, both varying by ∼1% over years and reaching each other after the equinox of 2009. The existence and the variation of SKR periods was proposed to result from a seasonal forcing of the magnetosphere-ionosphere coupling at the origin of these radio emissions. Further insights were provided by higher level observables. Statistical studies of the position of SKR sources (Cecconi et al. 2009; Lamy et al. 2009) showed (i) that they lie on magnetic field lines colocated with the atmospheric auroral oval, with a strong local time variation of their intensity maximising at dawn (Lamy et al. 2009), and (ii) that the southern modulation is produced by an active region, extended in longitude, and rotating at the southern SKR period (Lamy 2011). The latter result, supported by an independent analysis of phases built from radio and magnetic field data (Andrews et al. 2011) and validated by another independent modeling study (Lamy et al. 2013), changed the simple strobe-like picture derived from Voyager to an intrinsic search-light phenomenon, which displays strobe-like characteristics when the observer is in view of the most intense, dawnside sources. This feature is consistent with the ubiquitous search-light modulation of various other magnetospheric observables at both SKR periods (modulation of particles and magnetic field, oscillations of magnetospheric boundaries and the auroral oval). The sum of these observations is proposed to result from two co-existing field-aligned current (FAC) systems, rotating at southern and northern radio periods (see e.g. Andrews et al. 2010). The ultimate driver of these FAC systems, though, is still unknown.

5.3.1.2 Source regions in sub-corotation At timescales shorter than the ∼11h periods (referred to as the 'rigid' corotation period), SKR dynamic spectra often display arcs lasting for a few minutes to a few hours, either vertex-early and/or vertex-late shaped, similar to jovian DAM arcs (Boischot et al. 1981; Thieman and Goldstein 1981). These structures, together with signal disappearance close to the planet, were quantitatively modeled as the result of visibility effects owing to the relative motion of radio sources with respect to the observer (Lamy et al. 2008a). More precisely, the correct modeling required oblique beaming angles with a steep decrease at high frequency, and active field lines moving in sub-corotation (here 90%).

Oblique beaming angles were theoretically obtained by assuming loss cone-driven CMI with 20 keV electrons. However, while the observed SKR beaming is indeed oblique with a decrease at high frequency, it is significantly variable (Cecconi et al. 2009; Lamy et al. 2009), although whether it varies with time, source position, and/or with wave direction is an open question. In addition, in situ measurements revealed shell distributions with 6–9 keV electrons within the SKR source region (Lamy et al. 2010; Schippers et al. 2011), shown to be an efficient CMI-driver able to produce the observed SKR intensities (Mutel et al. 2010). A possible way to account for oblique and variable beaming from shell-driven (quasi-perpendicular) emission relies on refraction close and far from the source.

Atmospheric auroral sources in sub-corotation have long been observed along the main auroral oval. Therefore, as the bulk of SKR is emitted on field lines co-located with the main oval, it is not surprising to observe sub-corotating sources at radio and optical wavelengths, as illustrated with recent simultaneous observations of a single auroral hot spot moving at 65% of corotation (Lamy et al. 2013). The range of sub-corotating velocities additionally matches the velocity of the ambient cold plasma populating auroral field lines (Thomsen et al. 2010). The co-existence of rotational and sub-corotational dynamics on adjacent field lines, likely relating to the intrinsic nature of the rotating FAC systems, remains to be further investigated.

5.3.2 Longer-term variations

SKR also exhibits variations on timescales longer than a planetary rotation, ranging from days to years.

Since Voyager, the solar wind has been known to be a key ingredient for driving SKR emissions, the most striking evidence of which was revealed by the sudden drop off of SKR intensity when Saturn was immersed in Jupiter's magnetotail for several intervals in 1981 (Desch 1983). Precisely, the level of SKR emission was found to be highly correlated with the solar wind dynamic (ram) pressure (Desch and Rucker 1983, 1985), later confirmed by Cassini (Rucker et al. 2008), rather than with the geometry of the magnetic field, which controls Earth substorms. Such a correspondence was tracked with long-term time series from approximately fixed spacecraft locations, which limits the visibility effects discussed in Section 5.3.1.2 above. This property was related to acceleration processes specific to Saturn, most efficient on the dawn sector, such as the Kelvin-Helmholtz instability on the flank of the magnetopause (Galopeau et al. 1995), field-aligned currents initiated by the shear between open and closed field lines (Cowley et al. 2004b), or the shear of swept back closed field lines (Southwood and Kivelson 2009).

The effect of interplanetary shocks on auroral emissions was recently investigated in more detail with coordinated observations (Kurth et al. 2005; Badman et al. 2008;

Clarke et al. 2009). These authors showed an overall brightening of the SKR spectrum lasting for several planetary rotations, matching a dawnside intensification of the auroral oval, and with a characteristic extension toward low frequencies. Importantly, the southern SKR phase was shown to be unaltered by solar wind compressions. Investigating such auroral intensifications from the magnetotail, Jackman et al. (2009, 2010) showed that SKR low frequency extensions coincide with plasmoid ejections.

Most recently, Kimura et al. (2013) investigated very long-term variations of northern and southern SKR spectra, separated by polarization, spanning six years of measurements. This study confirms the prominent role of solar wind pressure over one solar cycle, and additionally identifies a seasonal dependence of the SKR activity, maximising in summer.

5.4 Summary

Observations at radio wavelengths, either acquired from the ground (high temporal and spectral sampling, interferometry) or from space-based probes (observations below 10 MHz, goniopolarimetry), have provided a wealth of information on the auroral processes at work in the magnetospheres of Jupiter and Saturn. Following the first analyses of radio emission flux, spectra, and time-variability, recent developments include accurate modeling of CMI-driven radiation, and the study of higher level observables (wave polarization, the source location). Such analyses have been illustrated with a few examples of internally-driven processes at Jupiter (Io and non-Io DAM visibility, millisecond S-bursts) and Saturn (rotational and sub-corotational modulation, seasonal effects) and compared to externally-driven processes (solar wind influences). The diagnosis provided by low frequency radio observations is not only of interest for the further study of giant planet magnetospheres (with JUNO and JUICE), but also more generally for all planetary and possible exoplanetary radio sources (Zarka 2007), with LOFAR, Bepi-Colombo and future missions toward the outer heliosphere.

6 Auroral signatures of magnetospheric dynamics and boundaries at Jupiter and Saturn

In this section the interpretation of auroral emissions in terms of magnetospheric dynamics is described, focussing in particular on the signatures of open-closed field line boundaries as evidence of the solar wind interaction, and their differences from magnetodisk-related processes and emissions.

The concept of an ‘open’ magnetosphere was first described for the terrestrial magnetosphere by Dungey (1963). He described how dayside planetary magnetic field lines can become open to the solar wind via magnetic reconnection with the interplanetary field at the magnetopause. The open field lines are then dragged anti-sunward by the magnetosheath flow to form the magnetotail lobes. The lobe field lines drift to the tail current sheet where reconnection occurs again to close the field lines. The newly-closed field lines are accelerated back toward the planet and circulate around to the dayside to complete the ‘Dungey cycle’ of flux circulation. The disconnected portion of open flux is lost downtail. Cowley et al. (2003) and Cowley et al. (2004b) have applied this concept to the rapidly-rotating magnetospheres of Jupiter and Saturn to illustrate the nature of plasma flow in different regions of the magnetospheres (see also Delamere

et al., this issue). In addition to the Dungey-cycle model of flux circulation, it has been proposed that the open field regions in the magnetospheres of Jupiter and Saturn could be maintained by viscous processes at the boundaries allowing for flux and plasma exchange, such as reconnection within Kelvin-Helmholtz vortices on the dusk flank (Delamere and Bagenal 2010; Desroche et al. 2013).

The characteristics of the open field region are mainly defined by the change in plasma population, i.e., the loss of previously-trapped magnetospheric plasma and entry of magnetosheath plasma, and the anti-sunward convection of the open field lines. In contrast, as explained in Section 1, the magnetodisk regions of the giant planet magnetospheres are characterised by a trapped, warm plasma population, including heavy ions originating from the moons, sub- or co-rotating with the planet. In this section we focus on the auroral signatures of open and closed field regions, and their boundaries, as these can be remotely monitored and provide a more global picture than the restricted spatial sampling of an in situ spacecraft.

6.1 Open-closed boundaries in Jupiter's magnetosphere

The extent of an open field region and the existence of a Dungey-cycle in Jupiter's magnetosphere have been debated because of the large size of the magnetosphere, and hence long transport times (Cowley et al. 2003; Badman and Cowley 2007; McComas and Bagenal 2007; Cowley et al. 2008; Delamere and Bagenal 2010). Although, as mentioned above, the processes leading to the replenishment of open flux have not been conclusively identified (i.e. large-scale Dungey-cycle circulation versus localised viscous interactions), in situ plasma measurements and remote sensing of ionospheric flows have indicated the presence of a persistent open field region, as discussed below.

6.1.1 Evidence for an open field region

6.1.1.1 In situ measurements Ulysses was, so far, the only spacecraft to sample Jupiter's high latitude region. It reached latitudes of $\sim 45^\circ$ during its encounter in Feb 1992. Simpson et al. (1992) identified a region of Jupiter's magnetosphere analogous to the Earth's polar cap, where the fluxes of MeV particles decreased, indicating their loss to the interplanetary medium. Supporting evidence was provided by a decrease of the proton/helium abundance ratio to values typical of interplanetary space, disappearance of the anisotropy in the corotational direction for ∼MeV protons, disappearance of the hot magnetospheric electrons, the detection of auroral hiss, and anti-sunward ion flow (Bame et al. 1992; Simpson et al. 1992; Stone et al. 1992; Cowley et al. 1993). The field-aligned current detected at the boundary as a perturbation in the magnetic field had only a weak signature (~ 1 nT) implying that the ionospheric conductivity at the magnetic footprint of the spacecraft was low (Cowley et al. 1993). However, the size and dynamics of this polar cap region could not be determined by the single spacecraft encounter.

Measurements of the magnetic field in the dawnside magnetotail lobes by Voyager showed they exhibit very low fluctuations compared to the plasma sheet, consistent with the extremely low electron densities detected ($< 10^{-5}$ cm^{-3}) (Gurnett et al. 1980; Acuña et al. 1983).

6.1.1.2 Auroral observations Jupiter's main auroral ovals have been shown to be generated by currents associated with the breakdown of corotation at 20–30 R_J at the inner edge of the equatorial middle magnetosphere (Cowley and Bunce 2001; Hill 2001). However, it is not yet certain which of the various auroral features seen at higher latitudes maps to the open lobes or their boundary in the ionosphere. Figure 32 illustrates the dark (yellow contour), swirl (red contour), and active (green contour) regions of the jovian northern UV polar aurora (Grodent et al. 2003b). The light purple circle indicates the projected location of the slit used to obtain the data shown in the right hand panel. This is the slit used at NASA IRTF to observe the infrared H_3^+ intensity and line-of-sight velocities (as described in Section 3.3), shown in the lower right panel. Stallard et al. (2003) and Cowley et al. (2003) suggested that the dark polar region (DPR), which was held fixed relative to the planetary rotation, could be the footprint of the open field lines. However, as shown in Figure 32 there is significant UV 'swirl' emission at 0–200 kR above background in this region, which requires collisions with electrons with energies greater than the H_2 ionization energy, 15.4 eV. It is not clear how the required fluxes and energies of electrons would be present on supposedly open, plasma-depleted field lines, particularly as Cowley et al. (2003) suggested this would be a region of downward current, i.e. upward-moving electrons.

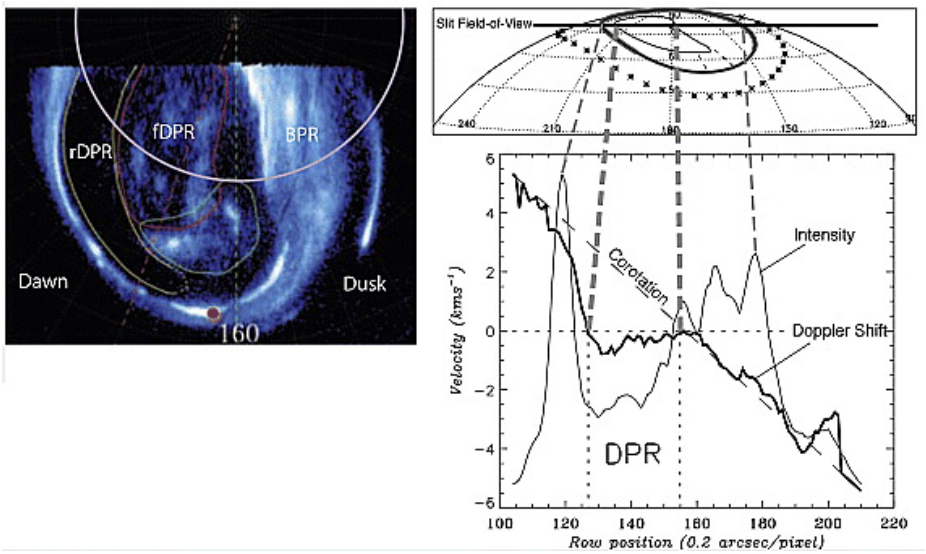

Fig. 32 (left) Polar projection of the northern UV auroral region showing the shape and position of the dark region (yellow contour), the swirl region (red contour), and the active region (green contour) as they appear at CML = 160° (marked with a vertical green dashed line). Longitude 180° is highlighted with a red dashed line. The red dot locates the magnetic footprint of Ganymede (VIP4 model) as the orbital longitude of the satellite matches the CML and therefore indicates the direction of magnetic noon at 15 R_J(Grodent et al. 2003b). The purple circle is latitude 74°, the projected location of the slit field of view of the data on the right. (top right) Viewing geometry and (bottom right) Doppler shifted H_3^+ IR emission profile from Stallard et al. (2003), showing the stagnated flows in the dark polar region (DPR). This DPR corresponds to the swirl region on the UV image on the left. Both images illustrate the dawn-dusk asymmetry of the polar auroral emission intensity. From Delamere and Bagenal (2010).

Vogt et al. (2011) attempted to address this issue by applying a flux equivalency mapping between Jupiter's equatorial magnetosphere and the ionosphere. They considered any region mapping beyond the magnetopause or beyond 150 R_J downtail to be open flux, and found that corresponded to a region of approximately 40° longitude by 20° latitude in the ionosphere. The amount of open flux was estimated to be ∼ 700 GWb in each hemisphere, in agreement with estimates based on the size of the magnetotail lobes and the average field strength (Acuña et al. 1983; Joy et al. 2002). In terms of the observed auroral features, Vogt et al. (2011) estimated that the active, swirl, and part of the dark regions all mapped to open field lines (see Figure 32), but the question remains as to what could produce the swirl emission on open field lines.

Pallier and Prangé (2001) and Pallier and Prangé (2004) determined a reference main oval from UV observations and scaled it to higher latitudes in a search for a persistent open-closed field line boundary aurora. They identified an arc of aurora in the northern hemisphere, surrounding a dark area of radius ∼ 10°, as a possible signature of the open-closed boundary. They also identified diffuse spots near local noon as signatures of the magnetospheric cusps in both the northern and southern hemispheres (labelled 4 in Figure 33). The color ratio (see Section 2.1.2.2 and 3.1.1) of these spots was particularly large, leading to an estimate of the characteristic electron energy (assuming a pure electron beam) of ∼ 200 keV, at the upper end of the range of values usually measured for different components of the aurora (Gustin et al. 2004a).

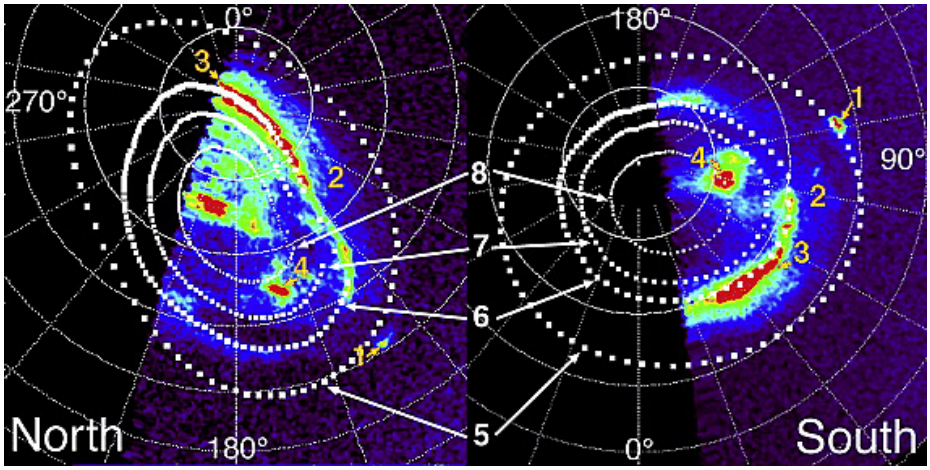

Fig. 33 Two consecutive color-coded polar projected maps of Jupiter's aurora on 15 August 1999 using HST-STIS (1180–1530 *Å* FWHM). Dark blue: the faint solar reflected flux, light blue-green: moderate emissions including (2) the 'low-latitude belt', and red: brightest auroral features, (1) Io footprint, (3) main oval, (4) conjugate polar cusps. The dotted curve on top of (3) is the Pallier-Prangé (PP) reference main oval. (7, 8) are the PP derived inner reference ovals, and (5) is the VIP4 model Io footprint. From Pallier and Prangé (2004).

6.1.2 Auroral signatures of reconnection at the open-closed boundary

In addition to the search for a persistent auroral signature of the open-closed boundary and cusps, other more transient features, possibly associated with reconnection events,

have been identified. Waite et al. (2001) showed a localised flare in the UV aurora reaching 37 MR (total H_2 and H emission) on a timescale of $\sim$ 70 s. Bonfond et al. (2011) identified intensifications in the UV polar emission with a 2 min periodicity. They magnetically mapped the location of these flares to the vicinity of the dayside magnetopause, and pointed out that their periodicity is similar to that identified for flux transfer events, which are bursts of reconnection with the interplanetary magnetic field (Walker and Russell 1985).

Signatures of Dungey-cycle tail reconnection, i.e. the closure of open magnetic field lines, have not been identified in Jupiter's aurora. Small spots have been observed inside the dawn arc of the main aurora in both UV and IR images, and related to Vasyliunas-cycle tail reconnection, which involves reconfiguration of closed field lines (Grodent et al. 2004; Radioti et al. 2008a, 2011b).

6.1.3 Comparison to magnetodisk-related emissions

In addition to the polar aurorae described above, at least some of which are related to the solar wind interaction, features have been identified at latitudes lower than Jupiter's main oval. The most obvious of these are the spots and downstream tails associated with the moons Io, Europa, and Ganymede (Connerney et al. 1993; Clarke et al. 2002). The moons orbit at radial distances of 5.9, 9.4, and 15.1 R_J and their auroral footprints provide valuable constraints for magnetic field models which seek to map magnetic field lines between the magnetosphere and the ionosphere (e.g. Connerney et al. 1998; Grodent et al. 2008; Hess et al. 2011b). The variability of the main oval and moon footprints attributed to increased mass-loading and hot plasma injection was described in Section 3.1.

One further auroral feature related to magnetodisk processes is the variable emission located equatorward of the main oval. Tomás et al. (2004) investigated electron pitch angle distributions measured by Galileo and identified a persistent, sharp transition between inner, trapped (maximum fluxes field-perpendicular) and outer, bidirectional populations at 10–17 R_J in the equatorial plane. They suggest that this transition could be caused by whistler waves scattering the electrons into a more field-aligned distribution, which then precipitate into the ionosphere to produce a relatively discrete auroral arc observed equatorward of the main oval (Grodent et al. 2003a). Transient, diffuse equatorward emissions of varying spatial extent have also been identified and related to injections of hotter plasma from larger radial distances, either via wave scattering, or field-aligned currents at the edges of the high pressure injected cloud (e.g. Mauk et al. 2002).

In conclusion, some high latitude auroral features have been suggested to be signatures of an open field region or its boundary, including magnetopause reconnection events. A polar cap-like region has been detected in situ at high latitudes and in the magnetotail, but its extent is not well constrained. The extent and replenishment of Jupiter's open field lines, which represent the transfer of plasma and momentum with the solar wind, are not well understood.

6.2 Open-closed boundaries in Saturn's magnetosphere

The efficiency of reconnection between Saturn's planetary field and the interplanetary magnetic field, which creates the open field region, has been questioned because of the supposed low efficiency of reconnection at the magnetopause in the high plasma beta regime (Scurry and Russell 1991; Masters et al. 2012), although this has been contradicted by observations at the Earth (Grocott et al. 2009). However, in situ measurements of the magnetopause have shown evidence for reconnection, from changes in the component of the magnetic field normal to the magnetopause, and/or the detection of heated or mixed plasma populations (Huddleston et al. 1997; McAndrews et al. 2008; Lai et al. 2012; Badman et al. 2013). These latter studies have concluded that reconnection is able to proceed at a sufficient rate at different locations across the magnetopause to produce a persistent open flux region at Saturn.

6.2.1 Characteristics of the open field region

6.2.1.1 In situ measurements As at Jupiter, the observations made by in situ spacecraft have provided evidence of an open field region in Saturn's magnetosphere. Ness et al. (1981) identified a tail lobe from Voyager-1 magnetic field data with a diameter of 80 R_S and likened it to the terrestrial magnetotail. The high latitude orbits made by Cassini have since provided a wealth of in situ measurements of the lobe and polar cap structure. For example, a decrease in electron flux by several orders of magnitude was observed by Cassini as it passed from the dayside magnetosphere to the higher latitudes over the southern polar cap (Bunce et al. 2008). This was interpreted as a crossing from closed to open field lines. Gurnett et al. (2010a) identified a plasma density boundary at high latitudes in Saturn's magnetosphere using Langmuir Probe measurements of electron density. They also related the decrease in density to the appearance of auroral hiss (broadband whistler mode waves observed at frequencies below the plasma frequency). Examination of the high energy ($\sim$ 200 keV) electron data indicated an upward electron anisotropy, suggesting that no electrons were returning from magnetic mirror points in the opposite hemisphere and hence that the high latitude field lines were open. An example of these measurements is shown in Figure 34.

6.2.1.2 Auroral observations The auroral field-aligned currents in Saturn's high latitude magnetosphere are also identified in Figure 34 as perturbations in the azimuthal (B_ϕ) component. These field aligned currents are responsible for Saturn's main auroral emission and lie close to the boundary between open and closed field lines, driven by the flow shear between anti-sunward open and outer magnetosphere flux tubes, and the sub-corotating middle and inner magnetospheric flux tubes (Cowley et al. 2004b,2004a; Bunce et al. 2008). The auroral oval maps to the outer magnetosphere, beyond the ring current, with the poleward boundary of the aurora mapping to the vicinity of the magnetopause on the dayside (Carbary et al. 2008; Belenkaya et al. 2011).

The auroral oval is therefore observed to change its size and power in response to solar wind conditions as open flux is created and destroyed (Clarke et al. 2005, 2009; Crary et al. 2005; Bunce et al. 2005; Badman et al. 2005). A selection of images acquired by HST demonstrating the variability of the southern UV aurorae is shown in Figure 35. Badman et al. (2006) showed from these images that the southern auroral oval varies in position from 2–20° co-latitude. If the poleward boundary of the auroral oval is used as a proxy for the open-closed boundary (this is likely to be an upper limit

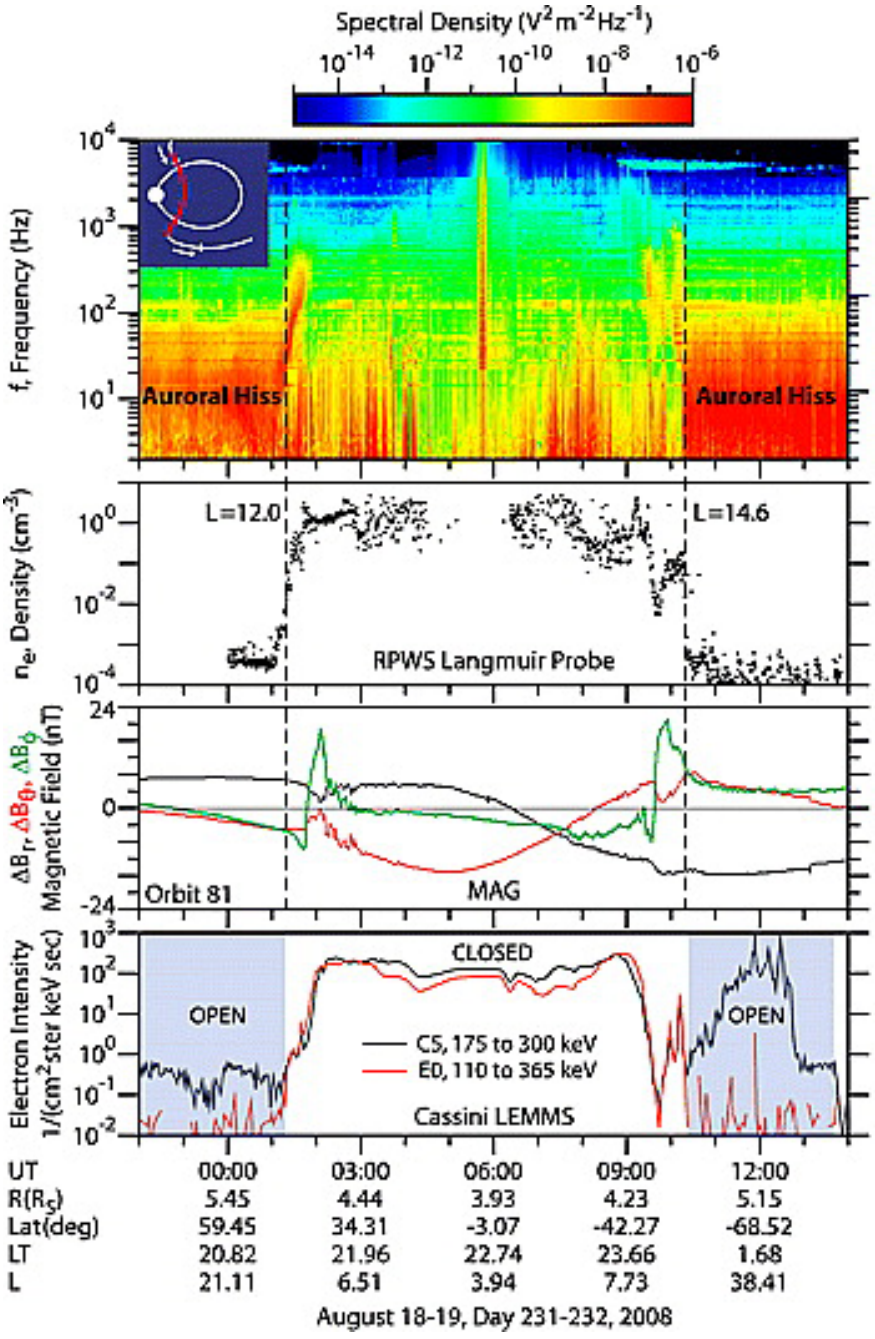

Fig. 34 A multi-plot comparison of (top) the electric field spectrum of auroral hiss, (top middle) the electron density from the Langmuir probe, (bottom middle) three magnetic field components from the magnetometer (MAG), and (bottom) the electron flux from the MIMI-LEMMS energetic electron detector. From Gurnett et al. (2010a).

following the discussion above), the amount of open flux threading the high latitude polar cap is estimated to be 15–50 GWb (Badman et al. 2005, 2014).

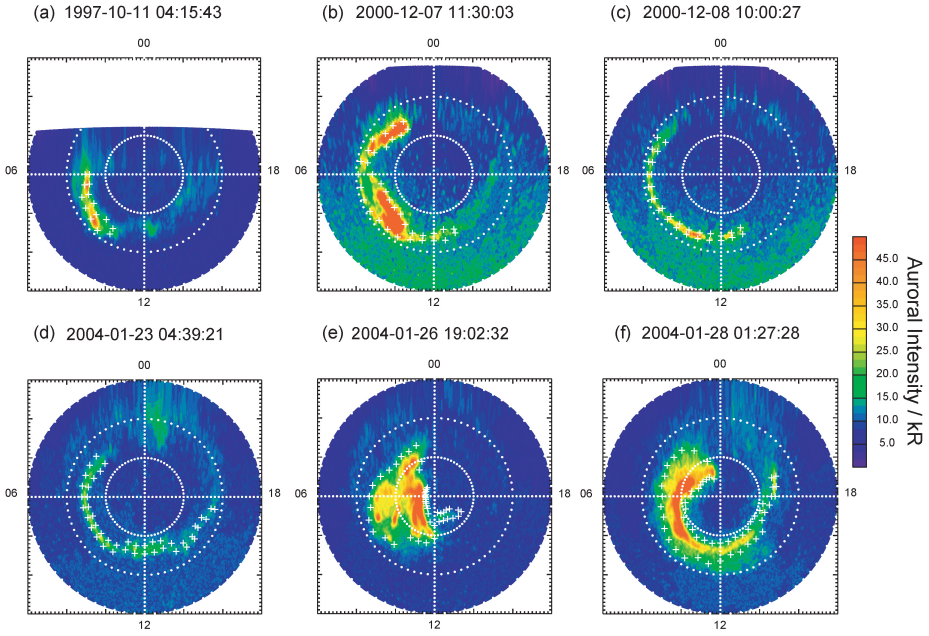

Fig. 35 Selection of six UV images of Saturn's southern aurora obtained during the interval 11 October 1997 to 30 January 2004, with the date and start time of each image shown at the top of each plot. The images are projected onto a polar grid from the pole to 30° co-latitude, viewed as though looking through the planet onto the southern pole. Noon is at the bottom of each plot, and dawn to the left, as indicated. The UV auroral intensity is plotted according to the colour scale shown on the right-hand side of the figure. The white crosses mark the poleward and equatorward boundaries of the auroral emissions. From Badman et al. (2006).

6.2.2 Auroral signatures of reconnection at the OCB

Several localised auroral features have been identified and related to reconnection processes close to the open-closed field line boundary. Gérard et al. (2004) identified an auroral spot poleward of the noon main auroral arc and suggested it was the signature of precipitation in the magnetospheric cusps. Bunce et al. (2005) modelled the ionospheric response to flow vortices produced by magnetopause reconnection events under different IMF conditions including auroral field aligned currents and related emission intensities. If plasma conditions are favourable then under northward IMF, reconnection is expected to proceed at the sub-solar magnetopause, resulting in anti-sunward ionospheric flows and currents close to the open-closed boundary (main oval), the opening of dayside magnetic field lines and subsequent expansion of the dayside auroral oval to lower latitudes. Conversely, high-latitude lobe reconnection would occur under prolonged southward IMF and result in reversed vortical flows and currents poleward of the open-closed boundary in the ionosphere. Sub-solar reconnection is therefore related

to the intensification of the main auroral arc in the noon region, while high-latitude reconnection is related to localised auroral emission poleward of the main oval (Bunce et al. 2005; Gérard et al. 2005).

Using high-sensitivity Cassini instruments, the signatures of transient magnetopause reconnection events have been identified in the noon and post-noon sectors. These appear as bifurcations of the main auroral arc that have been observed to travel poleward while the end connected to the main oval sub-corotates (Radioti et al. 2011a; Badman et al. 2012a, 2013). Similar dusk sector features have been shown to be non-conjugate with their appearance in each hemisphere related to the direction of the IMF; specifically, they will be favoured in the northern hemisphere for $B_Y < 0$ and in the southern hemisphere for $B_Y > 0$ because of the different sense of the associated field aligned current patterns and the source plasma populations (Meredith et al. 2013).

The signatures of nightside reconnection events have also been identified. Broad infilling of the polar cap region has been interpreted as a large tail reconnection event in response to a solar wind compression of the magnetosphere (Cowley et al. 2005; Badman et al. 2005; Stallard et al. 2012b). Smaller-scale UV spots and blobs have been attributed to tail energisation events, likely driven by reconnection (Mitchell et al. 2009a; Jackman et al. 2013), but it has not yet been possible to conclude whether they are associated with reconfiguration of stretched, closed field lines (the Vasyliunas cycle) or the closure of open lobe field lines.

6.2.3 Interpretation and differences from magnetodisk processes

While the above discussion has concentrated on the solar wind-related emissions in the vicinity of the open-closed field line boundary, the auroral signatures of internally-driven processes have also been detected at Saturn. A relatively broad mid-latitude auroral oval has been observed in ground-based measurements of H_3^+ emission, with the peak emission at 62°N and 58°S (Stallard et al. 2008; Stallard et al. 2010). Stallard et al. (2010) suggest that this corresponds to the location where plasma flow initially departs from rigid corotation at radial distances of 3–4 R_S in the magnetosphere (Wilson et al. 2009), and invoke a system of corotation-enforcement currents flowing between the ionosphere and inner magnetosphere. The small radial distance of this corotation-breakdown region is somewhat unexpected, given that the region of maximum ion formation is further out, closer to ~ 6 R_S (Sittler et al. 2008).

A similar feature was observed in HST UV images but the emission is very faint compared to the main oval (1.7 kR) such that it can only be observed on the nightside when the tilt angle is large so that the emission is limb-brightened (Grodent et al. 2005). Grodent et al. (2010) suggested that this emission could be driven by precipitation of keV electrons identified in the magnetosphere at 4–11 R_S. They demonstrated that these electrons, scattered by whistler waves into the loss cone, would have sufficient energy flux to produce the level of UV emission observed, such that the field-aligned currents suggested by Stallard et al. (2010) are not required. One further possible generation mechanism is the precipitation of hot protons from the ring current (e.g. Mitchell et al. 2009a). Interestingly, simultaneous observations of the UV and IR emissions have revealed instances of an equatorward arc at 70°S present at all wavelengths (Lamy et al. 2013), and present only in H and H_2, but not H_3^+ (Melin et al. 2011) (see also Section 3.4.2).

More localised diffuse emission features have been identified in the dayside UV aurora by Radioti et al. (2013b), who related them to ENA emissions in the same local

time sectors of the magnetosphere. They suggested that both the auroral and ENA emissions are the signatures of injections of hot plasma in the magnetosphere although the origin of the injections is unclear.

In addition to these diffuse auroral features, the auroral footprint of Enceladus has been observed in a small number of the UVIS images (Pryor et al. 2011). The reason for its variable intensity is most likely to be the time-variability of the cryogenic plume activity on the moon affecting the local plasma conditions. So far the Enceladus auroral footprint has only been identified in the UV.

In conclusion, while Saturn's auroral emissions vary strongly with the solar wind interaction, their precise relationship to the open-closed boundary, as revealed by different instrumentation, is not yet determined. Monitoring the size and shape of the auroral emissions provides a valuable tool for describing the the extent to which the solar wind and interplanetary magnetic field are controlling Saturn's magnetosphere, relative to magnetospheric dynamics.

7 Future observations and outstanding issues

Much of our understanding of auroral processes at the giant planets has come from dedicated ground- and space-based telescope observing campaigns. Long-term sequences of observations are also provided by high inclination views of the polar regions by orbiters. In 2016 there will be the opportunity for simultaneous polar observations of two different environments with the NASA polar orbiter Juno at Jupiter, and Cassini's high inclination orbits at Saturn. These types of observation are valuable for imaging both hemispheres independent of the planet's season (when one hemisphere is preferentially observed from the Earth), and for obtaining a good view of the nightside aurora, which is difficult to observe from the Earth. These orbits also provide invaluable simultaneous in situ detections of auroral plasma and currents with imaging or spectra of the conjugate aurora.

Unfortunately, beyond late 2017 there will be no orbital spacecraft at any of the giant planets until 2030 when the European Space Agency (ESA) Juice mission arrives at Jupiter. Secondly, with the ageing HST facing retirement within the not too distant future, there will be no facilities capable of observing in the ultraviolet, with no replacement yet in the pipeline. These facts mean, by necessity, that we are entering an era where ground-based infrared observations of H_3^+ will be the main tool with which to study the magnetosphere-ionosphere-thermosphere interaction at the gas giants. This is not to say, of course, that this upcoming era is entirely bleak – ground-based telescopes are getting larger, with much improved instrumentation, with many facilities developing the capability of removing the influence of the Earth's atmosphere via adaptive optics (AO). The planetary observing capabilities of the James Webb Space Telescope, scheduled for launch in 2018, are under investigation. The limitation of infrared observations, however, remains the long lifetime of H_3^+, which precludes the study of short term auroral variability observed in the UV. Ongoing and future observations of Jupiter's radio emissions will be provided by the Low Frequency Array (LOFAR), Nançay Decametric Array (NDA) and Stereo spacecraft.

The outstanding questions for different scientific targets are given at the end of each section above. A common idea is for coordinated observations at different wavelengths,

and with in situ measurements of solar wind or magnetospheric field and plasma conditions. Coordinated observations are required to study the full thermosphere-ionosphere-magnetosphere coupled system, including Io (or Enceladus at Saturn) activity and solar wind conditions. Observations on different timescales are also required. For Io-related variations at Jupiter, the observing interval should cover several months. To study the solar wind variation, the observing interval should be at least one week to resolve the time scale for magnetospheric compression and the following expansion phase. The observable parameters required are Io's volcano activity, the Io torus, the IR and UV aurora, radio and X-ray emissions, and the solar wind (ideally in-situ near the planet or at least propagated from near-Earth measurements). Since solar wind-driven variation causes compression of the magnetosphere followed by expansion, and different response processes should occur in each phase, the temporal variation is important. At Saturn, combined studies using Cassini remote-multi-wavelength and in-situ observations are an ongoing approach (See Section 3.4). A coordinated observation campaign at Jupiter was carried out in early 2014 when EUV spectral observations of the Io torus and Jupiter's polar region were taken by the JAXA Sprint-A/Hisaki mission. The results of such campaigns will provide significant advances in our understanding of the relative contributions of solar wind and magnetodisk driving processes at the giant planets.

Acknowledgements The authors acknowledge the support of EUROPLANET RI project (Grant agreement no.: 228319) funded by EU; and also the support of the International Space Science Institute (Bern). SVB was supported by a Royal Astronomical Society Research Fellowship. MG was partially supported by the Science and Technology Facilities Council (STFC) through the Consolidated Grant to Imperial College London.

References

N. Achilleos, S. Miller, J. Tennyson, A.D. Aylward, I. Müller-Wodarg, D. Rees, JIM: A time-dependent, three-dimensional model of Jupiter's thermosphere and ionosphere. J. Geophys. Res. **103**, 20089–20112 (1998). doi:10.1029/98JE00947

M.H. Acuña, K.W. Behannon, J.E.P. Connerney, Jupiter's Magnetic Field and Magnetosphere, in *Physics of the Jovian Magnetosphere*, ed. by A.J. Dessler, 1983, pp. 1–50

J.M. Ajello, W. Pryor, L. Esposito, I. Stewart, W. McClintock, J. Gustin, D. Grodent, J.-C. Gérard, J.T. Clarke, The Cassini Campaign observations of the Jupiter aurora by the Ultraviolet Imaging Spectrograph and the Space Telescope Imaging Spectrograph. Icarus **178**, 327–345 (2005). doi:10.1016/j.icarus.2005.01.023

D.J. Andrews, A.J. Coates, S.W.H. Cowley, M.K. Dougherty, L. Lamy, G. Provan, P. Zarka, Magnetospheric period oscillations at Saturn: Comparison of equatorial and high-latitude magnetic field periods with north and south Saturn kilometric radiation periods. J. Geophys. Res. **115**, 12252 (2010). doi:10.1029/2010JA015666

D.J. Andrews, B. Cecconi, S.W.H. Cowley, M.K. Dougherty, L. Lamy, P. G., P. Zarka, Planetary period oscillations in Saturn's magnetosphere: Evidence in magnetic field phase data for rotational modulation of Saturn kilometric radiation emissions. J. Geophys. Res. **116** (2011). doi:10.1029/2011JA016636

O.V. Arkhypov, H.O. Rucker, Amalthea's modulation of Jovian decametric radio emission. A&A **467**, 353–358 (2007). doi:10.1051/0004-6361:20066505

S.V. Badman, S.W.H. Cowley, Significance of Dungey-cycle flows in Jupiter's and Saturn's magnetospheres, and their identification on closed equatorial field lines. Ann. Geophys. **25**, 941–951 (2007). doi:10.5194/angeo-25-941-2007

S.V. Badman, E.J. Bunce, J.T. Clarke, S.W.H. Cowley, J.-C. Gérard, D. Grodent, S.E. Milan, Open flux estimates in Saturn's magnetosphere during the January 2004 Cassini-HST campaign, and implications for reconnection rates. J. Geophys. Res. **110** (2005). doi:10.1029/2005JA011240

S.V. Badman, S.W.H. Cowley, J.-C. Gérard, D. Grodent, A statistical analysis of the location and width of Saturn's southern auroras. Ann. Geophys. **24**(12), 3533–3545 (2006)
S.V. Badman, S.W.H. Cowley, L. Lamy, B. Cecconi, P. Zarka, Relationship between solar wind corotating interaction regions and the phasing and intensity of Saturn kilometric radiation bursts. Ann. Geophysicae **26**(12), 3641–3651 (2008)
S.V. Badman, C. Tao, A. Grocott, S. Kasahara, H. Melin, R.H. Brown, K.H. Baines, M. Fujimoto, T. Stallard, Cassini VIMS observations of latitudinal and hemispheric variations in Saturn's infrared auroral intensity. Icarus **216**, 367–375 (2011a). doi:10.1016/j.icarus.2011.09.031
S.V. Badman, N. Achilleos, K.H. Baines, R.H. Brown, E.J. Bunce, M.K. Dougherty, H. Melin, J.D. Nichols, T. Stallard, Location of Saturn's northern infrared aurora determined from Cassini VIMS images. Geophys. Res. Lett. **38**(2011b). doi:10.1029/2010GL046193
S.V. Badman, N. Achilleos, C.S. Arridge, K.H. Baines, R.H. Brown, E.J. Bunce, A.J. Coates, S.W.H. Cowley, M.K. Dougherty, M. Fujimoto, G. Hospodarsky, S. Kasahara, T. Kimura, H. Melin, D.G. Mitchell, T. Stallard, C. Tao, Cassini observations of ion and electron beams at Saturn and their relationship to infrared auroral arcs. J. Geophys. Res. **117**(2012a). doi:10.1029/2011JA017222
S.V. Badman, D.J. Andrews, S.W.H. Cowley, L. Lamy, G. Provan, C. Tao, S. Kasahara, T. Kimura, M. Fujimoto, H. Melin, T. Stallard, R.H. Brown, K.H. Baines, Rotational modulation and local time dependence of Saturn's infrared H_3^+ auroral intensity. J. Geophys. Res. **117**(A9), 09228 (2012b)
S.V. Badman, A. Masters, H. Hasegawa, M. Fujimoto, A. Radioti, D. Grodent, N. Sergis, M.K. Dougherty, A.J. Coates, Bursty magnetic reconnection at Saturn's magnetopause. Geophys. Res. Lett. **40**, 1027–1031 (2013). doi:10.1002/grl.50199
S.V. Badman, C.M. Jackman, J.D. Nichols, J.-C. Gérard, Open flux in Saturn's magnetosphere. Icarus **231**, 137–145 (2014). doi:10.1016/j.icarus.2013.12.004
F. Bagenal, P.A. Delamere, Flow of mass and energy in the magnetospheres of Jupiter and Saturn. J. Geophys. Res. **116**, 5209 (2011). doi:10.1029/2010JA016294
F. Bagenal, T.E. Dowling, W.B. McKinnon, *Jupiter* (Cambridge Univ. Press, ???, 2004)
S.J. Bame, B.L. Barraclough, W.C. Feldman, G.R. Gisler, J.T. Gosling, D.J. McComas, J.L. Phillips, M.F. Thomsen, B.E. Goldstein, M. Neugebauer, Jupiter's Magnetosphere: Plasma Description from the Ulysses Flyby. Science **257**, 1539–1543 (1992). doi:10.1126/science.257.5076.1539
R.L. Baron, T. Owen, J.E.P. Connerney, T. Satoh, J. Harrington, Solar Wind Control of Jupiter's H_3^+ Auroras. Icarus **120**, 437–442 (1996). doi:10.1006/icar.1996.0063
C.H. Barrow, Jupiter's decametric radio emission and solar activity. Planet. Space. Sci. **26**, 1193–1199 (1978). doi:10.1016/0032-0633(78)90059-4
C.H. Barrow, Association of corotating magnetic sector structure with Jupiter's decameter-wave radio emission. J. Geophys. Res. **84**, 5366–5372 (1979). doi:10.1029/JA084iA09p05366
C.H. Barrow, Latitudinal beaming and local time effects in the decametre-wave radiation from Jupiter observed at the Earth and from Voyager. Astron. Astrophys. **101**, 142–149 (1981)
D. Barrow, K.I. Matcheva, Impact of atmospheric gravity waves on the jovian ionosphere. Icarus **211**, 609–622 (2011). doi:10.1016/j.icarus.2010.10.017
D.J. Barrow, K.I. Matcheva, Modeling the effect of atmospheric gravity waves on Saturn's ionosphere. Icarus **224**(1), 32–42 (2013). doi:10.1016/j.icarus.2013.01.027
E.S. Belenkaya, S.W.H. Cowley, J.D. Nichols, M.S. Blokhina, V.V. Kalegaev, Magnetospheric mapping of the dayside UV auroral oval at Saturn using simultaneous HST images, Cassini IMF data, and a global magnetic field model. Ann. Geophys. **29**, 1233–1246 (2011). doi:10.5194/angeo-29-1233-2011
R.F. Benson, W. Calvert, Isis 1 observations at the source of auroral kilometric radiation. Geophys. Res. Lett. **6**, 479–482 (1979). doi:10.1029/GL006i006p00479
A. Bhardwaj, G.R. Gladstone, Auroral emissions of the giant planets. Rev. Geophys. **38**, 295–354 (2000). doi:10.1029/1998RG000046
A. Bhardwaj, R.F. Elsner, J.H. Waite Jr., G.R. Gladstone, T.E. Cravens, P.G. Ford, Chandra Observation of an X-Ray Flare at Saturn: Evidence of Direct Solar Control on Saturn's Disk X-Ray Emissions. Astrophys. J. Lett. **624**, 121–124 (2005a). doi:10.1086/430521
A. Bhardwaj, G. Branduardi-Raymont, R.F. Elsner, G.R. Gladstone, G. Ramsay, P. Rodriguez, R. Soria, J.H. Waite, T.E. Cravens, Solar control on Jupiter's equatorial X-ray emis-

sions: 26-29 November 2003 XMM-Newton observation. Geophys. Res. Lett. **32**, 3 (2005b). doi:10.1029/2004GL021497

A. Bhardwaj, R.F. Elsner, J.H. Waite Jr., G.R. Gladstone, T.E. Cravens, P.G. Ford, The Discovery of Oxygen Kα X-Ray Emission from the Rings of Saturn. Astrophys. J. Lett. **627**, 73–76 (2005c). doi:10.1086/431933

A. Boischot, Y. Leblanc, A. Lecacheux, B.M. Pedersen, M.L. Kaiser, Arc structure in Saturn's radio dynamic spectra. Nature **292**, 727 (1981). doi:10.1038/292727a0

B. Bonfond, D. Grodent, J.-C. Gérard, A. Radioti, J. Saur, S. Jacobsen, UV Io footprint leading spot: A key feature for understanding the UV Io footprint multiplicity? Geophys. Res. Lett. **35**(5) (2008). doi:10.1029/2007GL032418

B. Bonfond, M.F. Vogt, J.-C. Gérard, D. Grodent, A. Radioti, V. Coumans, Quasi-periodic polar flares at Jupiter: A signature of pulsed dayside reconnections? Geophys. Res. Lett. **38**, 2104 (2011). doi:10.1029/2010GL045981

B. Bonfond, D. Grodent, J.-C. Gérard, T. Stallard, J.T. Clarke, M. Yoneda, A. Radioti, J. Gustin, Auroral evidence of Io's control over the magnetosphere of Jupiter. Geophys. Res. Lett. **39** (2012). doi:doi:10.1029/2011GL050253

B. Bonfond, S. Hess, F. Bagenal, J.-C. Gérard, D. Grodent, A. Radioti, J. Gustin, J.T. Clarke, The multiple spots of the Ganymede auroral footprint. Geophys. Res. Lett. **40**, 4977–4981 (2013). doi:10.1002/grl.50989

S.W. Bougher, J.H. Waite, T. Majeed, G.R. Gladstone, Jupiter Thermospheric General Circulation Model (JTGCM): Global structure and dynamics driven by auroral and Joule heating. J. Geophys. Res. **110**, 4008 (2005). doi:10.1029/2003JE002230

G. Branduardi-Raymont, A. Bhardwaj, R.F. Elsner, G.R. Gladstone, G. Ramsay, P. Rodriguez, R. Soria, J.H. Waite Jr., T.E. Cravens, A study of Jupiter's aurorae with XMM-Newton. Astron. Astrophys. **463**, 761–774 (2007a). doi:10.1051/0004-6361:20066406

G. Branduardi-Raymont, A. Bhardwaj, R.F. Elsner, G.R. Gladstone, G. Ramsay, P. Rodriguez, R. Soria, J.H. Waite, T.E. Cravens, Latest results on Jovian disk X-rays from XMM-Newton. Planet. Space. Sci. **55**, 1126–1134 (2007b). doi:10.1016/j.pss.2006.11.017

G. Branduardi-Raymont, R.F. Elsner, M. Galand, D. Grodent, T.E. Cravens, P. Ford, G.R. Gladstone, J.H. Waite, Spectral morphology of the X-ray emission from Jupiter's aurorae. J. Geophys. Res. **113**, 2202 (2008). doi:10.1029/2007JA012600

G. Branduardi-Raymont, A. Bhardwaj, R.F. Elsner, P. Rodriguez, X-rays from Saturn: a study with XMM-Newton and Chandra over the years 2002-05. Astron. Astrophys. **510**, 73 (2010). doi:10.1051/0004-6361/200913110

G. Branduardi-Raymont, P.G. Ford, K.C. Hansen, L. Lamy, A. Masters, B. Cecconi, A.J. Coates, M.K. Dougherty, G.R. Gladstone, P. Zarka, Search for Saturn's X-ray aurorae at the arrival of a solar wind shock. J. Geophys. Res. **118** (2013). doi:doi:10.1002/jgra.50112

R.H. Brown, K.H. Baines, G. Bellucci, J.P. Bibring, B.J. Buratti, F. Capaccioni, P. Cerroni, R.N. Clark, A. Coradini, D.P. Cruikshank, P. Drossart, V. Formisano, R. Jaumann, Y. Langevin, D.L. Matson, T.B. McCord, V. Mennella, E. Miller, R.M. Nelson, P.D. Nicholson, B. Sicardy, C. Sotin, The Cassini Visual and Infrared Mapping Spectrometer (VIMS) investigation. Space Sci. Rev. **115**(1-4), 111–168 (2004). doi:10.1007/s11214-004-1453-x

E.J. Bunce, S.W.H. Cowley, S.E. Milan, Interplanetary magnetic field control of Saturn's polar cusp aurora. Ann. Geophys. **23**, 1405–1431 (2005). doi:10.5194/angeo-23-1405-2005

E.J. Bunce, S.W.H. Cowley, J.A. Wild, Azimuthal magnetic fields in Saturn's magnetosphere: effects associated with plasma sub-corotation and the magnetopause-tail current system. Ann. Geophys. **21**, 1709–1722 (2003). doi:10.5194/angeo-21-1709-2003

E.J. Bunce, S.W.H. Cowley, T.K. Yeoman, Jovian cusp processes: Implications for the polar aurora. J. Geophys. Res. **109**, 9 (2004). doi:10.1029/2003JA010280

E.J. Bunce, S.W.H. Cowley, D.M. Wright, A.J. Coates, M.K. Dougherty, N. Krupp, W.S. Kurth, A.M. Rymer, In situ observations of a solar wind compression-induced hot plasma injection in Saturn's tail. Geophys. Res. Lett. **322**, 20–04 (2005). doi:10.1029/2005GL022888

E.J. Bunce, C.S. Arridge, J.T. Clarke, A.J. Coates, S.W.H. Cowley, M.K. Dougherty, J.-C. Gérard, D. Grodent, K.C. Hansen, J.D. Nichols, D.J. Southwood, D.L. Talboys, Origin of Saturn's aurora: Simultaneous observations by Cassini and the Hubble Space Telescope. J. Geophys. Res. **113** (2008). doi:10.1029/2008JA013257

B.F. Burke, K.L. Franklin, Observations of a Variable Radio Source Associated with the Planet Jupiter. J. Geophys. Res. **60**, 213–217 (1955). doi:10.1029/JZ060i002p00213

J.F. Carbary, The morphology of Saturn's ultraviolet aurora. J. Geophys. Res. **117** (2012).

doi:10.1029/2012JA017670
J.F. Carbary, Longitude dependences of Saturn's ultraviolet aurora. Geophys. Res. Lett. **40**(10), 1902–1906 (2013). doi:10.1002/grl.50430
J.F. Carbary, D.G. Mitchell, P. Brandt, E.C. Roelof, S.M. Krimigis, Statistical morphology of ENA emissions at Saturn. J. Geophys. Res. **113**, 5210 (2008). doi:10.1029/2007JA012873
J.A. Carter, S. Sembay, A.M. Read, A high charge state coronal mass ejection seen through solar wind charge exchange emission as detected by XMM-Newton. MNRAS **402**, 867–878 (2010). doi:10.1111/j.1365-2966.2009.15985.x
B. Cecconi, Goniopolarimetric Techniques for Low-frequency Radio Astronomy in Space, in *Observing Photons in Space*, vol. 9, 2010, pp. 263–277
B. Cecconi, L. Lamy, P. Zarka, R. Prangé, W.S. Kurth, P. Louarn, Goniopolarimetric study of the revolution 29 perikrone using the Cassini Radio and Plasma Wave Science instrument high-frequency radio receiver. J. Geophys. Res. **114**, 3215 (2009). doi:10.1029/2008JA013830
B. Cecconi, S. Hess, A. Hérique, M.R. Santovito, D. Santos-Costa, P. Zarka, G. Alberti, D. Blankenship, J.-L. Bougeret, L. Bruzzone, W. Kofman, Natural radio emission of Jupiter as interferences for radar investigations of the icy satellites of Jupiter. Planet. Space. Sci. **61**, 32–45 (2012). doi:10.1016/j.pss.2011.06.012
J.-Y. Chaufray, T.K. Greathouse, G.R. Gladstone, J.H. Waite, J.-P. Maillard, T. Majeed, S.W. Bougher, E. Lellouch, P. Drossart, Spectro-imaging observations of Jupiter's 2 μm auroral emission. II: Thermospheric winds. Icarus **211**, 1233–1241 (2011). doi:10.1016/j.icarus.2010.11.021
J.T. Clarke, J. Ajello, G. Ballester, L. Ben Jaffel, J. Connerney, J.-C. Gérard, G.R. Gladstone, D. Grodent, W. Pryor, J. Trauger, J.H. Waite, Ultraviolet emissions from the magnetic footprints of Io, Ganymede and Europa on Jupiter. Nature **415**(6875), 997–1000 (2002)
J.T. Clarke, D. Grodent, S.W.H. Cowley, E.J. Bunce, P. Zarka, J.E.P. Connerney, T. Satoh, Jupiter's Aurora, in *Jupiter. The Planet, Satellites and Magnetosphere*, ed. by F. Bagenal, T.E. Dowling, W.B. McKinnon, 2004, pp. 639–670
J.T. Clarke, J.-C. Gérard, D. Grodent, S. Wannawichian, J. Gustin, J. Connerney, F. Crary, M. Dougherty, W. Kurth, S.W.H. Cowley, E.J. Bunce, T. Hill, J. Kim, Morphological differences between Saturn's ultraviolet aurorae and those of Earth and Jupiter. Nature **433**(7027), 717–719 (2005). doi:10.1038/nature03331
J.T. Clarke, J. Nichols, J.-C. Gerard, D. Grodent, K.C. Hansen, W. Kurth, G.R. Gladstone, J. Duval, S. Wannawichian, E. Bunce, S.W.H. Cowley, F. Crary, M. Dougherty, L. Lamy, D. Mitchell, W. Pryor, K. Retherford, T. Stallard, B. Zieger, P. Zarka, B. Cecconi, Response of Jupiter's and Saturn's auroral activity to the solar wind. J. Geophys. Res. **114** (2009). doi:10.1029/2008JA013694
J.E.P. Connerney, J.H. Waite, New model of Saturn's ionosphere with an influx of water from the rings. Nature **312**(5990), 136–138 (1984)
J.E.P. Connerney, R. Baron, T. Satoh, T. Owen, Images of Excited H_3^+ at the Foot of the Io Flux Tube in Jupiter's Atmosphere. Science **262**, 1035–1038 (1993). doi:10.1126/science.262.5136.1035
J.E.P. Connerney, M.H. Acuña, N.F. Ness, T. Satoh, New models of Jupiter's magnetic field constrained by the Io flux tube footprint. J. Geophys. Res. **103**, 11929–11940 (1998). doi:10.1029/97JA03726
S.W.H. Cowley, E.J. Bunce, Origin of the main auroral oval in Jupiter's coupled magnetosphere-ionosphere system. Planet. Space. Sci. **49**, 1067–1088 (2001). doi:10.1016/S0032-0633(00)00167-7
S.W.H. Cowley, E.J. Bunce, J.M. O'Rourke, A simple quantitative model of plasma flows and currents in Saturn's polar ionosphere. J. Geophys. Res. **109**(2004a). doi:10.1029/2003JA010375
S.W.H. Cowley, E.J. Bunce, R. Prange, Saturn's polar ionospheric flows and their relation to the main auroral oval. Ann. Geophysicae **22**(4), 1379–1394 (2004b)
S.W.H. Cowley, A. Balogh, M.K. Dougherty, T.M. Edwards, R.J. Forsyth, R.J. Hynds, K. Staines, Ulysses observations of anti-sunward flow on Jovian polar cap field lines. Planet. Space. Sci. **41**, 987–998 (1993). doi:10.1016/0032-0633(93)90103-9
S.W.H. Cowley, E.J. Bunce, T.S. Stallard, S. Miller, Jupiter's polar ionospheric flows: Theoretical interpretation. Geophys. Res. Lett. **30**, 1220 (2003). doi:10.1029/2002GL016030
S.W.H. Cowley, S.V. Badman, E.J. Bunce, J.T. Clarke, J.-C. Gérard, D. Grodent, C.M. Jackman, S.E. Milan, T.K. Yeoman, Reconnection in a rotation-dominated magneto-

sphere and its relation to Saturn's auroral dynamics. J. Geophys. Res. **110**(A2) (2005). doi:10.1029/2004JA010796

S.W.H. Cowley, C.S. Arridge, E.J. Bunce, J.T. Clarke, A.J. Coates, M.K. Dougherty, J.-C. Gérard, D. Grodent, J.D. Nichols, D.L. Talboys, Auroral current systems in Saturn's magnetosphere: Comparison of theoretical models with Cassini and HST observations. Ann. Geophysicae **26**(9), 2613–2630 (2008)

F.J. Crary, On the generation of an electron beam by Io. J. Geophys. Res. **102**, 37–50 (1997). doi:10.1029/96JA02409

F. Crary, J. Clarke, M. Dougherty, P. Hanlon, K. Hansen, J. Steinberg, B. Barraclough, A. Coates, J. Gerard, D. Grodent, W. Kurth, D. Mitchell, A. Rymer, D. Young, Solar wind dynamic pressure and electric field as the main factors controlling Saturn's aurorae. Nature **433**(7027), 720–722 (2005). doi:DOI 10.1038/nature03333

T.E. Cravens, Vibrationally excited molecular hydrogen in the upper atmosphere of Jupiter. J. Geophys. Res. **92**, 11083–11100 (1987). doi:10.1029/JA092iA10p11083

T.E. Cravens, Comet Hyakutake x-ray source: Charge transfer of solar wind heavy ions. Geophys. Res. Lett. **24**, 105–108 (1997). doi:10.1029/96GL03780

T.E. Cravens, Heliospheric X-ray Emission Associated with Charge Transfer of the Solar Wind with Interstellar Neutrals. Astrophys. J. Lett. **532**, 153–156 (2000). doi:10.1086/312574

T.E. Cravens, N. Ozak, Auroral Ion Precipitation and Acceleration at the Outer Planets. Washington DC American Geophysical Union Geophysical Monograph Series **197**, 287–294 (2012). doi:10.1029/2011GM001159

T.E. Cravens, E. Howell, J.H. Waite, G.R. Gladstone, Auroral oxygen precipitation at Jupiter. J. Geophys. Res. **100**, 17153–17162 (1995). doi:10.1029/95JA00970

T.E. Cravens, J.H. Waite, T.I. Gombosi, N. Lugaz, G.R. Gladstone, B.H. Mauk, R.J. MacDowall, Implications of Jovian X-ray emission for magnetosphere-ionosphere coupling. J. Geophys. Res. **108**, 1465 (2003). doi:10.1029/2003JA010050

A. Dalgarno, M. Yan, W. Liu, Electron Energy Deposition in a Gas Mixture of Atomic and Molecular Hydrogen and Helium. Astrophys. J. Supp. Ser. **125**, 237–256 (1999). doi:10.1086/313267

P.A. Delamere, F. Bagenal, Solar wind interaction with Jupiter's magnetosphere. J. Geophys. Res. **115**, 10201 (2010). doi:10.1029/2010JA015347

G.T. Delory, R.E. Ergun, C.W. Carlson, L. Muschietti, C.C. Chaston, W. Peria, J.P. McFadden, R. Strangeway, FAST observations of electron distributions within AKR source regions. Geophys. Res. Lett. **25**, 2069–2072 (1998). doi:10.1029/98GL00705

K. Dennerl, X-rays from Venus observed with Chandra. Planet. Space. Sci. **56**, 1414–1423 (2008). doi:10.1016/j.pss.2008.03.008

K. Dennerl, 2009, High Resolution X-ray Spectroscopy of Comets with Xmm-newton/rgs. `http://www.mssl.ucl.ac.uk/\\texttildelowgbr/workshop3/papers/comets_mssl_2009_kd.pdf`

K. Dennerl, Charge Transfer Reactions. Space Sci. Rev. **157**, 57–91 (2010). doi:10.1007/s11214-010-9720-5

K. Dennerl, C.M. Lisse, A. Bhardwaj, V. Burwitz, J. Englhauser, H. Gunell, M. Holmström, F. Jansen, V. Kharchenko, P.M. Rodríguez-Pascual, First observation of Mars with XMM-Newton. High resolution X-ray spectroscopy with RGS. Astron. Astrophys. **451**, 709–722 (2006). doi:10.1051/0004-6361:20054253

K. Dennerl, C.M. Lisse, A. Bhardwaj, D.J. Christian, S.J. Wolk, D. Bodewits, T.H. Zurbuchen, M. Combi, S. Lepri, Solar system X-rays from charge exchange processes. Astron. Nachr. **333**, 324 (2012). doi:10.1002/asna.201211663

M.D. Desch, Radio emission signature of Saturn immersions in Jupiter's magnetic tail. J. Geophys. Res. **88**, 6904–6910 (1983). doi:10.1029/JA088iA09p06904

M.D. Desch, M.L. Kaiser, Voyager measurement of the rotation period of Saturn's magnetic field. Geophys. Res. Lett. **8**, 253–256 (1981). doi:10.1029/GL008i003p00253

M.D. Desch, H.O. Rucker, The relationship between Saturn kilometric radiation and the solar wind. J. Geophys. Res. **88**, 8999–9006 (1983). doi:10.1029/JA088iA11p08999

M.D. Desch, H.O. Rucker, Saturn radio emission and the solar wind - Voyager-2 studies. Adv. Space Res. **5**, 333–336 (1985). doi:10.1016/0273-1177(85)90159-0

M. Desroche, F. Bagenal, P.A. Delamere, N. Erkaev, Conditions at the magnetopause of Saturn and implications for the solar wind interaction. J. Geophys. Res. **118**, 3087–3095 (2013). doi:10.1002/jgra.50294

A.J. Dessler, *Physics of the Jovian Magnetosphere* (Cambridge Univ. Press, Cambridge, UK,

1983)
M.K. Dougherty, L.W. Esposito, S.M. Krimigis, *Saturn from Cassini-huygens* (Springer, ???, 2009). doi:10.1007/978-1-4020-9217-6
M.K. Dougherty, K.K. Khurana, F.M. Neubauer, C.T. Russell, J. Saur, J.S. Leisner, M.E. Burton, Identification of a dynamic atmosphere at Enceladus with the Cassini magnetometer. Science **311**(5766), 1406–1409 (2006). doi:10.1126/science.1120985. http://www.sciencemag.org/content/311/5766/1406.abstract
P. Drossart, J.P. Maillard, J. Caldwell, S.J. Kim, J.K.G. Watson, W.A. Majewski, J. Tennyson, S. Miller, S.K. Atreya, J.T. Clarke, J.H. Waite, R. Wagener, Detection of H_3^+ on Jupiter. Nature **340**, 539–541 (1989)
J.W. Dungey, The Structure of the Exosphere or Adventures in Velocity Space, in *Geophysics, The Earth's Environment*, ed. by C. De Witt, J. Hieblot, L. Le Beau, 1963, p. 503
U.A. Dyudina, A.P. Ingersoll, S.P. Ewald, C.C. Porco, G. Fischer, W.S. Kurth, R.A. West, Detection of visible lightning on Saturn. Geophys. Res. Lett. **37**, 9205 (2010). doi:10.1029/2010GL043188
R.F. Elsner, G.R. Gladstone, J.H. Waite, F.J. Crary, R.R. Howell, R.E. Johnson, P.G. Ford, A.E. Metzger, K.C. Hurley, E.D. Feigelson, G.P. Garmire, A. Bhardwaj, D.C. Grodent, T. Majeed, A.F. Tennant, M.C. Weisskopf, Discovery of Soft X-Ray Emission from Io, Europa, and the Io Plasma Torus. Astrophys. J. **572**, 1077–1082 (2002). doi:10.1086/340434
R.F. Elsner, N. Lugaz, J.H. Waite, T.E. Cravens, G.R. Gladstone, P. Ford, D. Grodent, A. Bhardwaj, R.J. MacDowall, M.D. Desch, T. Majeed, Simultaneous Chandra X ray, Hubble Space Telescope ultraviolet, and Ulysses radio observations of Jupiter's aurora. J. Geophys. Res. **110**, 1207 (2005). doi:10.1029/2004JA010717
R.E. Ergun, C.W. Carlson, J.P. McFadden, G.T. Delory, R.J. Strangeway, P.L. Pritchett, Electron-Cyclotron Maser Driven by Charged-Particle Acceleration from Magnetic Field-aligned Electric Fields. Astrophys. J. **538**, 456–466 (2000). doi:10.1086/309094
Y. Ezoe, K. Ishikawa, T. Ohashi, Y. Miyoshi, N. Terada, Y. Uchiyama, H. Negoro, Discovery of Diffuse Hard X-Ray Emission Around Jupiter with Suzaku. Astrophys. J. Lett. **709**, 178–182 (2010). doi:10.1088/2041-8205/709/2/L178
W.M. Farrell, M.L. Kaiser, M.D. Desch, A model of the lightning discharge at Jupiter. Geophys. Res. Lett. **26**, 2601–2604 (1999). doi:10.1029/1999GL900527
G. Fischer, M.D. Desch, P. Zarka, M.L. Kaiser, D.A. Gurnett, W.S. Kurth, W. Macher, H.O. Rucker, A. Lecacheux, W.M. Farrell, B. Cecconi, Saturn lightning recorded by Cassini/RPWS in 2004. Icarus **183**, 135–152 (2006). doi:10.1016/j.icarus.2006.02.010
G. Fischer, W.S. Kurth, U.A. Dyudina, M.L. Kaiser, P. Zarka, A. Lecacheux, A.P. Ingersoll, D.A. Gurnett, Analysis of a giant lightning storm on Saturn. Icarus **190**, 528–544 (2007). doi:10.1016/j.icarus.2007.04.002
G. Fischer, D.A. Gurnett, W.S. Kurth, F. Akalin, P. Zarka, U.A. Dyudina, W.M. Farrell, M.L. Kaiser, Atmospheric Electricity at Saturn. Space Sci. Rev. **137**, 271–285 (2008). doi:10.1007/s11214-008-9370-z
G. Fischer, D.A. Gurnett, P. Zarka, L. Moore, U.A. Dyudina, Peak electron densities in Saturn's ionosphere derived from the low-frequency cutoff of Saturn lightning. J. Geophys. Res. **116**, 4315 (2011). doi:10.1029/2010JA016187
B.L. Fleshman, P.A. Delamere, F. Bagenal, T. Cassidy, The roles of charge exchange and dissociation in spreading Saturn's neutral clouds. J. Geophys. Res. **117**, 5007 (2012). doi:10.1029/2011JE003996
D. Flower, *Molecular Collisions in the Interstellar Medium* (Cambridge Univ. Press, Cambridge, UK, 1990)
J.L. Fox, M.I. Galand, R.E. Johnson, Energy Deposition in Planetary Atmospheres by Charged Particles and Solar Photons. Space Sci. Rev. **139**, 3–62 (2008). doi:10.1007/s11214-008-9403-7
K. Fukazawa, T. Ogino, R.J. Walker, A simulation study of dynamics in the distant Jovian magnetotail. J. Geophys. Res. **115** (2010). doi:10.1029/2009JA015228
M. Galand, S. Chakrabarti, Auroral Processes in the Solar System. Washington DC American Geophysical Union Geophysical Monograph Series **130**, 55 (2002)
M. Galand, S. Chakrabarti, Proton aurora observed from the ground. J. Atmos. Terr. Phys. **68**, 1488–1501 (2006). doi:10.1016/j.jastp.2005.04.013
M. Galand, D. Lummerzheim, Contribution of proton precipitation to space-based auroral FUV observations. J. Geophys. Res. **109**, 3307 (2004). doi:10.1029/2003JA010321
M. Galand, L. Moore, B. Charnay, I. Müller-Wodarg, M. Mendillo, Solar primary and secondary

ionization at Saturn. J. Geophys. Res. **114**, 6313 (2009). doi:10.1029/2008JA013981
M. Galand, L. Moore, I. Müller-Wodarg, M. Mendillo, S. Miller, Response of Saturn's auroral ionosphere to electron precipitation: Electron density, electron temperature, and electrical conductivity. J. Geophys. Res. **116**, 9306 (2011). doi:10.1029/2010JA016412
P.H.M. Galopeau, A. Lecacheux, Variations of Saturn's radio rotation period measured at kilometer wavelengths. J. Geophys. Res. **105**, 13089–13102 (2000). doi:10.1029/1999JA005089
P.H.M. Galopeau, P. Zarka, D.L. Quéau, Source location of Saturn's kilometric radiation: The Kelvin-Helmholtz instability hypothesis. J. Geophys. Res. **1002**, 26397–26410 (1995). doi:10.1029/95JE02132
N. Gehrels, E.C. Stone, Energetic oxygen and sulfur ions in the Jovian magnetosphere and their contribution to the auroral excitation. J. Geophys. Res. **88**, 5537–5550 (1983). doi:10.1029/JA088iA07p05537
F. Genova, P. Zarka, C.H. Barrow, Voyager and Nancay observations of the Jovian radio-emission at different frequencies - Solar wind effect and source extent. Astron. Astrophys. **182**, 159–162 (1987)
J.-C. Gérard, V. Singh, A model of energy deposition of energetic electrons and EUV emission in the Jovian and Saturnian atmospheres and implications. J. Geophys. Res. **87**, 4525–4532 (1982). doi:10.1029/JA087iA06p04525
J.-C. Gérard, J. Gustin, D. Grodent, P. Delamere, J.T. Clarke, Excitation of the FUV Io tail on Jupiter: Characterization of the electron precipitation. J. Geophys. Res. **107**, 1394 (2002). doi:10.1029/2002JA009410
J.-C. Gérard, J. Gustin, D. Grodent, J.T. Clarke, A. Grard, Spectral observations of transient features in the FUV Jovian polar aurora. J. Geophys. Res. **108**, 1319 (2003). doi:10.1029/2003JA009901
J.-C. Gérard, D. Grodent, J. Gustin, A. Saglam, J.T. Clarke, J.T. Trauger, Characteristics of Saturn's FUV aurora observed with the Space Telescope Imaging Spectrograph. J. Geophys. Res. **109**(A9) (2004). doi:10.1029/2004JA010513
J.-C. Gérard, E.J. Bunce, D. Grodent, S.W.H. Cowley, J.T. Clarke, S.V. Badman, Signature of Saturn's auroral cusp: Simultaneous Hubble Space Telescope FUV observations and upstream solar wind monitoring. J. Geophys. Res. **110** (2005). doi:10.1029/2005JA011094
J.-C. Gérard, B. Bonfond, J. Gustin, D. Grodent, J.T. Clarke, D. Bisikalo, V. Shematovich, Altitude of Saturn's aurora and its implications for the characteristic energy of precipitated electrons. Geophys. Res. Lett. **36** (2009). doi:10.1029/2008GL036554
J.-C. Gérard, J. Gustin, W.R. Pryor, D. Grodent, B. Bonfond, A. Radioti, G.R. Gladstone, J.T. Clarke, J.D. Nichols, Remote sensing of the energy of auroral electrons in Saturn's atmosphere: Hubble and Cassini spectral observations . Icarus **223**(1) (2013). doi:10.1016/j.icarus.2012.11.033 10.1016/j.icarus.2012.11.033 10.1016/j.icarus.2012.11.033
G.R. Gladstone, J.H. Waite, D. Grodent, W.S. Lewis, F.J. Crary, R.F. Elsner, M.C. Weisskopf, T. Majeed, J.-M. Jahn, A. Bhardwaj, J.T. Clarke, D.T. Young, M.K. Dougherty, S.A. Espinosa, T.E. Cravens, A pulsating auroral X-ray hot spot on Jupiter. Nature **415**, 1000–1003 (2002)
T.I. Gombosi, T.P. Armstrong, C.S. Arridge, K.K. Khurana, S.M. Krimigis, N. Krupp, A.M. Persoon, M.F. Thomsen, Saturn's Magnetospheric Configuration, in *Saturn from Cassini-Huygens*, ed. by M.K. Dougherty, L.W. Esposito, S.M. Krimigis (Springer, Dordrecht Heidelberg London New York, 2009), pp. 203–255
A. Grocott, S.V. Badman, S.W.H. Cowley, S.E. Milan, J.D. Nichols, T.K. Yeoman, Magnetosonic Mach number dependence of the efficiency of reconnection between planetary and interplanetary magnetic fields. J. Geophys. Res. **114** (2009). doi:10.1029/2009JA014330
D. Grodent, J.H. Waite Jr., J.-C. Gérard, A self-consistent model of the Jovian auroral thermal structure. J. Geophys. Res. **106**, 12933–12952 (2001). doi:10.1029/2000JA900129
D. Grodent, J.T. Clarke, J. Kim, J.H. Waite, S.W.H. Cowley, Jupiter's main auroral oval observed with HST-STIS. J. Geophys. Res. **108**, 1389 (2003a). doi:10.1029/2003JA009921
D. Grodent, J.T. Clarke, J.H. Waite, S.W.H. Cowley, J.-C. Gérard, J. Kim, Jupiter's polar auroral emissions. J. Geophys. Res. **108**, 1366 (2003b). doi:10.1029/2003JA010017
D. Grodent, J.-C. Gérard, J.T. Clarke, G.R. Gladstone, J.H. Waite, A possible auroral signature of a magnetotail reconnection process on Jupiter. J. Geophys. Res. **109**, 5201 (2004). doi:10.1029/2003JA010341
D. Grodent, J.-C. Gérard, S.W.H. Cowley, E.J. Bunce, J.T.. Clarke, Variable morphology of Saturn's southern ultraviolet aurora. J. Geophys. Res. **110** (2005). doi:10.1029/2004JA010983

D. Grodent, B. Bonfond, J.-C. GéRard, A. Radioti, J. Gustin, J.T. Clarke, J. Nichols, J.E.P. Connerney, Auroral evidence of a localized magnetic anomaly in Jupiter's northern hemisphere. J. Geophys. Res. **113**, 9201 (2008). doi:10.1029/2008JA013185

D. Grodent, A. Radioti, B. Bonfond, J.-C. Gérard, On the origin of Saturn's outer auroral emission. J. Geophys. Res. **115**, 8219 (2010). doi:10.1029/2009JA014901

D.A. Gurnett, W.S. Kurth, F.L. Scarf, The structure of the Jovian magnetotail from plasma wave observations. Geophys. Res. Lett. **7**, 53–56 (1980). doi:10.1029/GL007i001p00053

D.A. Gurnett, W.S. Kurth, J.D. Menietti, A.M. Persoon, An unusual rotationally modulated attenuation band in the Jovian hectometric radio emission spectrum. Geophys. Res. Lett. **25**, 1841–1844 (1998). doi:10.1029/98GL01400

D.A. Gurnett, W.S. Kurth, G.B. Hospodarsky, A.M. Persoon, P. Zarka, A. Lecacheux, S.J. Bolton, M.D. Desch, W.M. Farrell, M.L. Kaiser, H.-P. Ladreiter, H.O. Rucker, P. Galopeau, P. Louarn, D.T. Young, W.R. Pryor, M.K. Dougherty, Control of Jupiter's radio emission and aurorae by the solar wind. Nature **415**, 985–987 (2002)

D.A. Gurnett, W.S. Kurth, G.B. Hospodarsky, A.M. Persoon, T.F. Averkamp, B. Cecconi, A. Lecacheux, P. Zarka, P. Canu, N. Cornilleau-Wehrlin, P. Galopeau, A. Roux, C. Harvey, P. Louarn, R. Bostrom, G. Gustafsson, J.-E. Wahlund, M.D. Desch, W.M. Farrell, M.L. Kaiser, K. Goetz, P.J. Kellogg, G. Fischer, H.-P. Ladreiter, H. Rucker, H. Alleyne, A. Pedersen, Radio and Plasma Wave Observations at Saturn from Cassini's Approach and First Orbit. Science **307**, 1255–1259 (2005). doi:10.1126/science.1105356

D.A. Gurnett, A. Lecacheux, W.S. Kurth, A.M. Persoon, J.B. Groene, L. Lamy, P. Zarka, J.F. Carbary, Discovery of a north-south asymmetry in Saturn's radio rotation period. Geophys. Res. Lett. **36**, 16102 (2009). doi:10.1029/2009GL039621

D.A. Gurnett, A.M. Persoon, A.J. Kopf, W.S. Kurth, M.W. Morooka, J.-E. Wahlund, K.K. Khurana, M.K. Dougherty, D.G. Mitchell, S.M. Krimigis, N. Krupp, A plasmapause-like density boundary at high latitudes in Saturn's magnetosphere. Geophys. Res. Lett. **37**, 16806 (2010a). doi:10.1029/2010GL044466

D.A. Gurnett, J.B. Groene, A.M. Persoon, J.D. Menietti, S.-Y. Ye, W.S. Kurth, R.J. MacDowall, A. Lecacheux, The reversal of the rotational modulation rates of the north and south components of Saturn kilometric radiation near equinox. Geophys. Res. Lett. **37**, 24101 (2010b). doi:10.1029/2010GL045796

J. Gustin, J.-C. Gérard, D. Grodent, S.W.H. Cowley, J.T. Clarke, A. Grard, Energy-flux relationship in the FUV Jovian aurora deduced from HST-STIS spectral observations. J. Geophys. Res. **109**, 10205 (2004a). doi:10.1029/2003JA010365

J. Gustin, P.D. Feldman, J.-C. Gérard, D. Grodent, A. Vidal-Madjar, L. Ben Jaffel, J.-M. Desert, H.W. Moos, D.J. Sahnow, H.A. Weaver, B.C. Wolven, J.M. Ajello, J.H. Waite, E. Roueff, H. Abgrall, Jovian auroral spectroscopy with FUSE: analysis of self-absorption and implications for electron precipitation. Icarus **171**, 336–355 (2004b). doi:10.1016/j.icarus.2004.06.005

J. Gustin, J.-C. Gérard, G.R. Gladstone, D. Grodent, J.T. Clarke, Characteristics of Jovian morning bright FUV aurora from Hubble Space Telescope/Space Telescope Imaging Spectrograph imaging and spectral observations. J. Geophys. Res. **111**, 9220 (2006). doi:10.1029/2006JA011730

J. Gustin, J.-C. Gérard, W.R. Pryor, P.D. Feldman, D. Grodent, G. Holsclaw, Characteristics of Saturn's polar atmosphere and auroral electrons derived from HST/STIS, FUSE and Cassini/UVIS spectra. Icarus **200**(1), 176–187 (2009). doi:10.1016/j.icarus.2008.11.013

J. Gustin, B. Bonfond, D. Grodent, J.-C. Gérard, Conversion from HST ACS and STIS auroral counts into brightness, precipitated power, and radiated power for H_2 giant planets. J. Geophys. Res. **117**, 7316 (2012). doi:10.1029/2012JA017607

J. Gustin, J.-C. Gérard, D. Grodent, G.R. Gladstone, J.T. Clarke, W.R. Pryor, V. Dols, B. Bonfond, A. Radioti, L. Lamy, J.M. Ajello, Effects of methane on giant planet's UV emissions and implications for the auroral characteristics. J. Molec. Spec. **291**, 108–117 (2013). doi:10.1016/j.jms.2013.03.010

C.J. Hansen, L. Esposito, A.I.F. Stewart, J. Colwell, A. Hendrix, W. Pryor, D. Shemansky, R. West, Enceladus' Water Vapor Plume. Science **311**, 1422–1425 (2006). doi:10.1126/science.1121254

W. Harris, J.T. Clarke, M.A. McGrath, G.E. Ballester, Analysis of Jovian Auroral H Ly-alpha Emission (1981-1991). Icarus **123**, 350–365 (1996). doi:10.1006/icar.1996.0164

S. Hess, B. Cecconi, P. Zarka, Modeling of Io-Jupiter decameter arcs, emission beaming and energy source. Geophys. Res. Lett. **35**, 13107 (2008). doi:10.1029/2008GL033656

S. Hess, F. Mottez, P. Zarka, Jovian S burst generation by Alfvén waves. J. Geophys. Res. **112**, 11212 (2007). doi:10.1029/2006JA012191
S. Hess, F. Mottez, P. Zarka, Effect of electric potential structures on Jovian S-burst morphology. Geophys. Res. Lett. **36** (2009). doi:10.1029/2009GL039084
S. Hess, P. Zarka, F. Mottez, Io Jupiter interaction, millisecond bursts and field-aligned potentials. Planet. Space. Sci. **55**, 89–99 (2007). doi:10.1016/j.pss.2006.05.016
S.L.G. Hess, B. Bonfond, P.A. Delamere, How could the Io footprint disappear? Planet. Space. Sci. **89**, 102–110 (2013). doi:10.1016/j.pss.2013.08.014
S.L.G. Hess, E. Echer, P. Zarka, Solar wind pressure effects on Jupiter decametric radio emissions independent of Io. Planet. Space. Sci. **70**, 114–125 (2012). doi:10.1016/j.pss.2012.05.011
S.L.G. Hess, A. Petin, P. Zarka, B. Bonfond, B. Cecconi, Lead angles and emitting electron energies of Io-controlled decameter radio arcs. Planet. Space. Sci. **58**(10), 1188–1198 (2010). doi:10.1016/j.pss.2010.04.011
S.L.G. Hess, P.A. Delamere, F. Bagenal, N.M. Schneider, A.J. Steffl, Longitudinal modulation of hot electrons in the Io plasma torus. J. Geophys. Res. **116**(2011a). doi:10.1029/2011JA016918
S.L.G. Hess, B. Bonfond, P. Zarka, D. Grodent, Model of the Jovian magnetic field topology constrained by the Io auroral emissions. J. Geophys. Res. **116**, 5217 (2011b). doi:10.1029/2010JA016262
S.L.G. Hess, E. Echer, P. Zarka, L. Lamy, P. Delamere, Multi-instrument study of the Jovian radio emissions triggered by solar wind shocks and inferred magnetospheric subcorotation rates. Planet. Space. Sci. (submitted)
S. Hess, P. Zarka, F. Mottez, V.B. Ryabov, Electric potential jumps in the Io-Jupiter flux tube. Planet. Space. Sci. **57**(1), 23–33 (2009). doi:10.1016/j.pss.2008.10.006
M.E. Hill, D.K. Haggerty, R.L. McNutt, C.P. Paranicas, Energetic particle evidence for magnetic filaments in Jupiter's magnetotail. J. Geophys. Res. **114** (2009). doi:10.1029/2009JA014374
T.W. Hill, Inertial limit on corotation. J. Geophys. Res. **84**, 6554–6558 (1979). doi:10.1029/JA084iA11p06554
T.W. Hill, The Jovian auroral oval. J. Geophys. Res. **106**, 8101–8108 (2001). doi:10.1029/2000JA000302
T.W. Hill, V.M. Vasyliūnas, Jovian auroral signature of Io's corotational wake. J. Geophys. Res. **107**, 1464 (2002). doi:10.1029/2002JA009514
Y. Hiraki, C. Tao, Parameterization of ionization rate by auroral electron precipitation in Jupiter. Ann. Geophys. **26**, 77–86 (2008). doi:10.5194/angeo-26-77-2008
M. Horanyi, T.E. Cravens, J.H. Waite Jr., The precipitation of energetic heavy ions into the upper atmosphere of Jupiter. J. Geophys. Res. **93**, 7251–7271 (1988). doi:10.1029/JA093iA07p07251
T.S. Huang, T.W. Hill, Corotation lag of the Jovian atmosphere, ionosphere, and magnetosphere. J. Geophys. Res. **94**, 3761–3765 (1989). doi:10.1029/JA094iA04p03761
D.E. Huddleston, C.T. Russell, G. Le, A. Szabo, Magnetopause structure and the role of reconnection at the outer planets. J. Geophys. Res. **102**(A11), 24289–24302 (1997)
D.L. Huestis, Hydrogen collisions in planetary atmospheres, ionospheres, and magnetospheres. Planet. Space. Sci. **56**, 1733–1743 (2008). doi:10.1016/j.pss.2008.07.012
Y. Hui, D.R. Schultz, V.A. Kharchenko, P.C. Stancil, T.E. Cravens, C.M. Lisse, A. Dalgarno, The Ion-induced Charge-exchange X-ray Emission of the Jovian Auroras: Magnetospheric or Solar Wind Origin? Astrophys. J. **702**, 158–162 (2009). doi:10.1088/0004-637X/702/2/L158
Y. Hui, D.R. Schultz, V.A. Kharchenko, A. Bhardwaj, G. Branduardi-Raymont, P.C. Stancil, T.E. Cravens, C.M. Lisse, A. Dalgarno, Comparative analysis and variability of the Jovian X-ray spectra detected by the Chandra and XMM-Newton observatories. J. Geophys. Res. **115**, 7102 (2010a). doi:10.1029/2009JA014854
Y. Hui, T.E. Cravens, N. Ozak, D.R. Schultz, What can be learned from the absence of auroral X-ray emission from Saturn? J. Geophys. Res. **115**, 10239 (2010b). doi:10.1029/2010JA015639
K. Imai, L. Wang, T.D. Carr, Modeling Jupiter's decametric modulation lanes. J. Geophys. Res. **102**, 7127–7136 (1997). doi:10.1029/96JA03960
A.P. Ingersoll, A.R. Vasavada, B. Little, C.D. Anger, S.J. Bolton, C. Alexander, K.P. Klaasen, W.K. Tobiska, Imaging Jupiter's Aurora at Visible Wavelengths. Icarus **135**, 251–264

(1998). doi:10.1006/icar.1998.5971
M. Ishimoto, M.R. Torr, Energetic He(+) precipitation in a mid-latitude aurora. J. Geophys. Res. **92**, 3284–3292 (1987). doi:10.1029/JA092iA04p03284
C.M. Jackman, J.A. Slavin, S.W.H. Cowley, Cassini observations of plasmoid structure and dynamics: Implications for the role of magnetic reconnection in magnetospheric circulation at Saturn. J. Geophys. Res. **116** (2011). doi:10.1029/2011JA016682
C.M. Jackman, L. Lamy, M.P. Freeman, P. Zarka, B. Cecconi, W.S. Kurth, S.W.H. Cowley, M.K. Dougherty, On the character and distribution of lower-frequency radio emissions at Saturn and their relationship to substorm-like events. J. Geophys. Res. **114**, 8211 (2009). doi:10.1029/2008JA013997
C.M. Jackman, C.S. Arridge, J.A. Slavin, S.E. Milan, L. Lamy, M.K. Dougherty, A.J. Coates, In situ observations of the effect of a solar wind compression on Saturn's magnetotail. J. Geophys. Res. **115**, 10240 (2010). doi:10.1029/2010JA015312
C.M. Jackman, N. Achilleos, S.W.H. Cowley, E.J. Bunce, A. Radioti, D. Grodent, S.V. Badman, M.K. Dougherty, W. Pryor, Auroral counterpart of magnetic field dipolarizations in Saturn's tail. Planet. Space. Sci. **82**, 34–42 (2013)
S.P. Joy, M.G. Kivelson, R.J. Walker, K.K. Khurana, C.T. Russell, T. Ogino, Probabilistic models of the Jovian magnetopause and bow shock locations. J. Geophys. Res. **107**, 1309 (2002). doi:10.1029/2001JA009146
S. Jurac, J.D. Richardson, A self-consistent model of plasma and neutrals at Saturn: Neutral cloud morphology. J. Geophys. Res. **110**, 9220 (2005). doi:10.1029/2004JA010635
M.L. Kaiser, M.D. Desch, J.E.P. Connerney, Saturn's ionosphere - Inferred electron densities. J. Geophys. Res. **89**, 2371–2376 (1984). doi:10.1029/JA089iA04p02371
M.L. Kaiser, M.D. Desch, A. Lecacheux, Saturnian kilometric radiation - Statistical properties and beam geometry. Nature **292**, 731–733 (1981). doi:10.1038/292731a0
M.L. Kaiser, M.D. Desch, J.W. Warwick, J.B. Pearce, Voyager detection of nonthermal radio emission from Saturn. Science **209**, 1238–1240 (1980). doi:10.1126/science.209.4462.1238
M.L. Kaiser, M.D. Desch, W.S. Kurth, A. Lecacheux, F. Genova, B.M. Pedersen, D.R. Evans, Saturn as a Radio Source, in *Saturn*, ed. by T. Gehrels, M.S. Matthews, 1984, pp. 378–415
S. Kasahara, E.A. Kronberg, N. Krupp, T. Kimura, C. Tao, S.V. Badman, A. Retinò, M. Fujimoto, Magnetic reconnection in the Jovian tail: X-line evolution and consequent plasma sheet structures. J. Geophys. Res. **116**, 11219 (2011). doi:10.1029/2011JA016892
V. Kharchenko, W. Liu, A. Dalgarno, X ray and EUV emission spectra of oxygen ions precipitating into the Jovian atmosphere. J. Geophys. Res. **103**, 26687–26698 (1998). doi:10.1029/98JA02395
V. Kharchenko, A. Dalgarno, D.R. Schultz, P.C. Stancil, Ion emission spectra in the Jovian X-ray aurora. Geophys. Res. Lett. **33**, 11105 (2006). doi:10.1029/2006GL026039
V. Kharchenko, A. Bhardwaj, A. Dalgarno, D.R. Schultz, P.C. Stancil, Modeling spectra of the north and south Jovian X-ray auroras. J. Geophys. Res. **113**, 8229 (2008). doi:10.1029/2008JA013062
K.K. Khurana, M.G. Kivelson, V.M. Vasyliunas, N. Krupp, J. Woch, A. Lagg, B.H. Mauk, W.S. Kurth, The Configuration of Jupiter's Magnetosphere, in *Jupiter. The Planet, Satellites and Magnetosphere*, ed. by F. Bagenal, T.E. Dowling, W.B. McKinnon, 2004, pp. 593–616
Y.H. Kim, J.L. Fox, The Jovian ionospheric E region. Geophys. Res. Lett. **18**, 123–126 (1991). doi:10.1029/90GL02587
Y.H. Kim, J.L. Fox, The chemistry of hydrocarbon ions in the Jovian ionosphere. Icarus **112**, 310–325 (1994). doi:10.1006/icar.1994.1186
Y.H. Kim, J.L. Fox, H.S. Porter, Densities and vibrational distribution of H(3+) in the Jovian auroral ionosphere. J. Geophys. Res. **97**, 6093–6101 (1992). doi:10.1029/92JE00454
Y.H. Kim, W.D. Pesnell, J.M. Grebowsky, J.L. Fox, Meteoric Ions in the Ionosphere of Jupiter. Icarus **150**, 261–278 (2001). doi:10.1006/icar.2001.6590
T. Kimura, F. Tsuchiya, H. Misawa, A. Morioka, H. Nozawa, M. Fujimoto, Periodicity analysis of Jovian quasi-periodic radio bursts based on Lomb-Scargle periodograms. J. Geophys. Res. **116**, 3204 (2011). doi:10.1029/2010JA016076
T. Kimura, L. Lamy, C. Tao, S.V. Badman, S. Kasahara, B. Cecconi, P. Zarka, A. Morioka, Y. Miyoshi, D. Maruno, Y. Kasaba, M. Fujimoto, Long-term modulations of Saturn's Auroral Radio Emissions by the Solar Wind and the Solar Ultraviolet flux. J. Geophys. Res. **submitted** (2013)
M.G. Kivelson, Moon-magnetosphere interactions: a tutorial. Adv. Space Res. **33**, 2061 (2004). doi:10.1016/j.asr.2003.08.042

A.J. Kliore, I.R. Patel, G.F. Lindal, D.N. Sweetnam, H.B. Hotz, J.H. Waite, T. McDonough, Structure of the ionosphere and atmosphere of Saturn from Pioneer 11 Saturn radio occultation. J. Geophys. Res. **85**, 5857–5870 (1980). doi:10.1029/JA085iA11p05857

A.J. Kliore, A.F. Nagy, E.A. Marouf, A. Anabtawi, E. Barbinis, D.U. Fleischman, D.S. Kahan, Midlatitude and high-latitude electron density profiles in the ionosphere of Saturn obtained by Cassini radio occultation observations. J. Geophys. Res. **114**, 4315 (2009). doi:10.1029/2008JA013900

S. Knight, Parallel electric fields. Planet. Space. Sci. **21**, 741–750 (1973). doi:10.1016/0032-0633(73)90093-7

P.S. Krstić, Inelastic Processes from Vibrationally Excited States in Slow H. Phys. Rev. A **66** (2002)

N. Krupp, J. Woch, A. Lagg, B. Wilken, S. Livi, D.J. Williams, Energetic particle bursts in the predawn Jovian magnetotail. Geophys. Res. Lett. **25**, 1249–1252 (1998). doi:10.1029/98GL00863

N. Krupp, A. Lagg, S. Livi, B. Wilken, J. Woch, E.C. Roelof, D.J. Williams, Global flows of energetic ions in Jupiter's equatorial plane: First-order approximation. J. Geophys. Res. **106**, 26017–26032 (2001). doi:10.1029/2000JA900138

W.S. Kurth, D.A. Gurnett, J.T. Clarke, P. Zarka, M.D. Desch, M.L. Kaiser, B. Cecconi, A. Lecacheux, W.M. Farrell, P. Galopeau, J.-C. Gérard, D. Grodent, R. Prangé, M.K. Dougherty, F.J. Crary, An Earth-like correspondence between Saturn's auroral features and radio emission. Nature **433**, 722–725 (2005). doi:10.1038/nature03334

W.S. Kurth, E.J. Bunce, J.T. Clarke, F.J. Crary, D.C. Grodent, A.P. Ingersoll, U.A. Dyudina, L. Lamy, D.G. Mitchell, A.M. Persoon, W.R. Pryor, J. Saur, T. Stallard, Auroral Processes, in *Saturn from Cassini-Huygens*, ed. by Dougherty, M. K., Esposito, L. W., & Krimigis, S. M. (Springer, Dordrecht Heidelberg London New York, 2009)

H.P. Ladreiter, P. Zarka, A. Lacacheux, Direction finding study of Jovian hectometric and broadband kilometric radio emissions: Evidence for their auroral origin. Planet. Space. Sci. **42**, 919–931 (1994). doi:10.1016/0032-0633(94)90052-3

H.R. Lai, H.Y. Wei, C.T. Russell, C.S. Arridge, M.K. Dougherty, Reconnection at the magnetopause of Saturn: Perspective from FTE occurrence and magnetosphere size. J. Geophys. Res. **117** (2012). doi:10.1029/2011JA017263

H.A. Lam, N. Achilleos, S. Miller, J. Tennyson, L.M. Trafton, T.R. Geballe, G. Ballester, A Baseline Spectroscopic Study of the Infrared Auroras of Jupiter. Icarus **127** (1997). doi:10.1006/icar.1997.5698

L. Lamy, Variability of Southern and Northern Periodicities of Saturn Kilometric Radiation, in *Planetary Radio Emissions*, ed. by H.O. Rucker (Austrian Acad. Sci. Press, Vienna, 2011), pp. 39–50. doi:doi:10.1553/PRE7s39

L. Lamy, P. Zarka, B. Cecconi, S. Hess, R. Prangé, Modeling of Saturn kilometric radiation arcs and equatorial shadow zone. J. Geophys. Res. **113**, 10213 (2008a). doi:10.1029/2008JA013464

L. Lamy, P. Zarka, B. Cecconi, R. Prangé, W.S. Kurth, D.A. Gurnett, Saturn kilometric radiation: Average and statistical properties. J. Geophys. Res. **113**, 7201 (2008b). doi:10.1029/2007JA012900

L. Lamy, B. Cecconi, R. Prangé, P. Zarka, J.D. Nichols, J.T. Clarke, An auroral oval at the footprint of Saturn's kilometric radio sources, colocated with the UV aurorae. J. Geophys. Res. **114**, 10212 (2009). doi:10.1029/2009JA014401

L. Lamy, P. Schippers, P. Zarka, B. Cecconi, C.S. Arridge, M.K. Dougherty, P. Louarn, N. André, W.S. Kurth, R.L. Mutel, D.A. Gurnett, A.J. Coates, Properties of Saturn kilometric radiation measured within its source region. Geophys. Res. Lett. **37**, 12104 (2010). doi:10.1029/2010GL043415

L. Lamy, B. Cecconi, P. Zarka, P. Canu, P. Schippers, W.S. Kurth, R.L. Mutel, D.A. Gurnett, D. Menietti, P. Louarn, Emission and propagation of Saturn kilometric radiation: Magnetoionic modes, beaming pattern, and polarization state. J. Geophys. Res. **116**, 4212 (2011). doi:10.1029/2010JA016195

L. Lamy, R. Prangé, K.C. Hansen, J.T. Clarke, P. Zarka, B. Cecconi, J. Aboudarham, N. André, G. Branduardi-Raymont, R. Gladstone, M. Barthélémy, N. Achilleos, P. Guio, M.K. Dougherty, H. Melin, S.W.H. Cowley, T.S. Stallard, J.D. Nichols, G. Ballester, Earth-based detection of Uranus' aurorae. Geophys. Res. Lett. **39**, 7105 (2012). doi:10.1029/2012GL051312

L. Lamy, R. Prangé, W. Pryor, J. Gustin, S.V. Badman, H. Melin, T. Stallard, D.G. Mitchell,

P.C. Brandt, Multi-spectral simultaneous diagnosis of Saturn's aurorae throughout a planetary rotation. J. Geophys. Res. **118**, 1–27 (2013). doi:10.1002/jgra.50404

L.J. Lanzerotti, T.P. Armstrong, R.E. Gold, K.A. Anderson, S.M. Krimigis, R.P. Lin, M. Pick, E.C. Roelof, E.T. Sarris, G.M. Simnett, The hot plasma environment at Jupiter - ULYSSES results. Science **257**, 1518–1524 (1992). doi:10.1126/science.257.5076.1518

G.F. Lindal, D.N. Sweetnam, V.R. Eshleman, The atmosphere of Saturn - an analysis of the Voyager radio occultation measurements. Astron. J. **90**, 1136–1146 (1985)

T.A. Livengood, H.W. Moos, Jupiter's north and south polar aurorae with IUE data. Geophys. Res. Lett. **17**, 2265–2268 (1990). doi:10.1029/GL017i012p02265

D.A. Lorentzen, Latitudinal and longitudinal dispersion of energetic auroral protons. Ann. Geophys. **18**, 81–89 (2000). doi:10.1007/s00585-000-0081-3

P. Louarn, D. Le Quéau, Generation of the Auroral Kilometric Radiation in plasma cavities-II. The cyclotron maser instability in small size sources. Planet. Space. Sci. **44**, 211–224 (1996). doi:10.1016/0032-0633(95)00122-0

P. Louarn, A. Roux, S. Perraut, W. Kurth, D. Gurnett, A study of the large-scale dynamics of the Jovian magnetosphere using the Galileo Plasma Wave Experiment. Geophys. Res. Lett. **25**, 2905–2908 (1998). doi:10.1029/98GL01774

R.J. MacDowall, M.L. Kaiser, M.D. Desch, W.M. Farrell, R.A. Hess, R.G. Stone, Quasiperiodic Jovian Radio bursts: observations from the Ulysses Radio and Plasma Wave Experiment. Planet. Space. Sci. **41**, 1059–1072 (1993). doi:10.1016/0032-0633(93)90109-F

T. Majeed, J.C. McConnell, The upper ionospheres of Jupiter and Saturn. Planet. Space. Sci. **39**, 1715–1732 (1991). doi:10.1016/0032-0633(91)90031-5

A. Masters, J.P. Eastwood, M. Swisdak, M.F. Thomsen, C.T. Russell, N. Sergis, F.J. Crary, M.K. Dougherty, A.J. Coates, S.M. Krimigis, The importance of plasma β conditions for magnetic reconnection at Saturn's magnetopause. Geophys. Res. Lett. **39** (2012). doi:10.1029/2012GL051372

K.I. Matcheva, D.J. Barrow, Small-scale variability in Saturn's lower ionosphere. Icarus **221**, 525–543 (2012). doi:10.1016/j.icarus.2012.08.022

B.H. Mauk, J.T. Clarke, D. Grodent, J.H. Waite, C.P. Paranicas, D.J. Williams, Transient aurora on Jupiter from injections of magnetospheric electrons. Nature **415**, 1003–1005 (2002)

B.H. Mauk, D.C. Hamilton, T.W. Hill, G.B. Hospodarsky, R.E. Johnson, C. Paranicas, E. Roussos, C.T. Russell, D.E. Shemansky, E.C. Sittler, R.M. Thorne, Fundamental Plasma Processes in Saturn's Magnetosphere, in *Saturn from Cassini-Huygens*, ed. by Dougherty, M. K., Esposito, L. W., & Krimigis, S. M., 2009. Chap. Fundamental plasma processes in Saturn's magnetosphere. doi:10.1007/978-1-4020-9217-6

H.J. McAndrews, C.J. Owen, M.F. Thomsen, B. Lavraud, A.J. Coates, M.K. Dougherty, D.T. Young, Evidence for reconnection at Saturn's magnetopause. J. Geophys. Res. **113**(A4) (2008). doi:10.1029/2007JA012581

D.J. McComas, F. Bagenal, Jupiter: A fundamentally different magnetospheric interaction with the solar wind. Geophys. Res. Lett. **34** (2007). doi:10.1029/2007GL031078

J.C. McConnell, J.B. Holberg, G.R. Smith, B.R. Sandel, D.E. Shemansky, A.L. Broadfoot, A new look at the ionosphere of Jupiter in light of the UVS occultation results. Planet. Space. Sci. **30**, 151–167 (1982). doi:10.1016/0032-0633(82)90086-1

M.B. McElroy, The Ionospheres of the Major Planets. Space Sci. Rev. **14**, 460–473 (1973). doi:10.1007/BF00214756

H. Melin, S. Miller, T. Stallard, D. Grodent, Non-LTE effects on H_3^+ emission in the jovian upper atmosphere. Icarus **178**, 97–103 (2005). doi:10.1016/j.icarus.2005.04.016

H. Melin, T. Stallard, S. Miller, J. Gustin, G. M., S.V. Badman, W.R. Pryor, J. O'Donoghue, R.H. Brown, K.H. Baines, Simultaneous Cassini VIMS and UVIS observations of Saturn's southern aurora: comparing emissions from H, H_2 and H_3^+ at a high spatial resolution. Geophys. Res. Lett. **38** (2011). doi:10.1029/2011GL048457

H. Melin, S. Miller, T. Stallard, L.M. Trafton, T.R. Geballe, Variability in the H_3^+ emission of Saturn: Consequences for ionisation rates and temperature. Icarus **186**(1), 234–241 (2007). doi:10.1016/j.icarus.2006.08.014

H. Menager, M. Barthélemy, J. Lilensten, H Lyman α line in Jovian aurorae: electron transport and radiative transfer coupled modelling. A&A **509**, 56 (2010). doi:10.1051/0004-6361/200912952

J.D. Menietti, D.A. Gurnett, G.B. Hospodarsky, C.A. Higgins, W.S. Kurth, P. Zarka, Modeling radio emission attenuation lanes observed by the Galileo and Cassini spacecraft. Planet.

Space. Sci. **51**, 533–540 (2003). doi:10.1016/S0032-0633(03)00078-3

J.D. Menietti, R.L. Mutel, P. Schippers, S.-Y. Ye, D.A. Gurnett, L. Lamy, Analysis of Saturn kilometric radiation near a source center. J. Geophys. Res. **116**, 12222 (2011). doi:10.1029/2011JA017056

C.J. Meredith, S.W.H. Cowley, K.C. Hansen, J.D. Nichols, T.K. Yeoman, Simultaneous conjugate observations of small-scale structures in Saturn's dayside ultraviolet auroras – implications for physical origins. J. Geophys. Res. **in press** (2013)

A.E. Metzger, D.A. Gilman, J.L. Luthey, K.C. Hurley, H.W. Schnopper, F.D. Seward, J.D. Sullivan, The detection of X rays from Jupiter. J. Geophys. Res. **88**, 7731–7741 (1983). doi:10.1029/JA088iA10p07731

S. Miller, A. Aylward, G. Millward, Giant Planet Ionospheres and Thermospheres: The Importance of Ion-Neutral Coupling. Space Sci. Rev. **116**, 319–343 (2005). doi:10.1007/s11214-005-1960-4

S. Miller, R.D. Joseph, J. Tennyson, Infrared emissions of H_3^+ in the atmosphere of Jupiter in the 2.1 and 4.0 micron region. Astrophys. J. Lett. **360**, 55–58 (1990). doi:10.1086/185811

S. Miller, T. Stallard, H. Melin, J. Tennyson, H_3^+ cooling in planetary atmospheres. Faraday Discussions **147**, 283 (2010). doi:10.1039/c004152c

G. Millward, S. Miller, T. Stallard, A.D. Aylward, N. Achilleos, On the Dynamics of the Jovian Ionosphere and ThermosphereIII. The Modelling of Auroral Conductivity. Icarus **160**, 95–107 (2002). doi:10.1006/icar.2002.6951

G. Millward, S. Miller, T. Stallard, N. Achilleos, A.D. Aylward, On the dynamics of the jovian ionosphere and thermosphere. Icarus **173**, 200–211 (2005). doi:10.1016/j.icarus.2004.07.027

D.G. Mitchell, S.M. Krimigis, C. Paranicas, P.C. Brandt, J.F. Carbary, E.C. Roelof, W.S. Kurth, D.A. Gurnett, J.T. Clarke, J.D. Nichols, J.-C. Gérard, D.C. Grodent, M.K. Dougherty, W.R. Pryor, Recurrent energization of plasma in the midnight-to-dawn quadrant of Saturn's magnetosphere, and its relationship to auroral UV and radio emissions. Planet. Space. Sci. **57**, 1732–1742 (2009a). doi:10.1016/j.pss.2009.04.002

D.G. Mitchell, J.F. Carbary, S.W.H. Cowley, T.W. Hill, P. Zarka, The Dynamics of Saturn's Magnetosphere, in *Saturn from Cassini-Huygens*, ed. by Dougherty, M. K., Esposito, L. W., & Krimigis, S. M. (Springer, ???, 2009b). Chap. The dynamics of Saturn's magnetosphere. doi:10.1007/978-1-4020-9217-6

L.E. Moore, M. Mendillo, Are plasma depletions in Saturn's ionosphere a signature of time-dependent water input? Geophys. Res. Lett. **34**(12) (2007). doi:10.1029/2007GL029381

L.E. Moore, M. Mendillo, I.C.F. Müller-Wodarg, D.L. Murr, Modeling of global variations and ring shadowing in Saturn's ionosphere. Icarus **172**, 503–520 (2004). doi:10.1016/j.icarus.2004.07.007

L. Moore, A.F. Nagy, A.J. Kliore, I. Müller-Wodarg, J.D. Richardson, M. Mendillo, Cassini radio occultations of Saturn's ionosphere: Model comparisons using a constant water flux. Geophys. Res. Lett. **33**, 22202 (2006). doi:10.1029/2006GL027375

L. Moore, M. Galand, I. Müller-Wodarg, R. Yelle, M. Mendillo, Plasma temperatures in Saturn's ionosphere. J. Geophys. Res. **113**, 10306 (2008). doi:10.1029/2008JA013373

L. Moore, I. Müller-Wodarg, M. Galand, A. Kliore, M. Mendillo, Latitudinal variations in Saturn's ionosphere: Cassini measurements and model comparisons. J. Geophys. Res. **115**, 11317 (2010). doi:10.1029/2010JA015692

L. Moore, G. Fischer, I. Müller-Wodarg, M. Galand, M. Mendillo, Diurnal variation of electron density in Saturn's ionosphere: Model comparisons with Saturn Electrostatic Discharge (SED) observations. Icarus **221**, 508–516 (2012). doi:10.1016/j.icarus.2012.08.010

J.I. Moses, S.F. Bass, The effects of external material on the chemistry and structure of Saturn's ionosphere. J. Geophys. Res. **105**, 7013–7052 (2000). doi:10.1029/1999JE001172

F. Mottez, S. Hess, P. Zarka, Explanation of dominant oblique radio emission at Jupiter and comparison to the terrestrial case. Planet. Space. Sci. **58**, 1414–1422 (2010). doi:10.1016/j.pss.2010.05.012

I.C.F. Müller-Wodarg, M. Mendillo, R.V. Yelle, A.D. Aylward, A global circulation model of Saturn's thermosphere. Icarus **180**, 147–160 (2006). doi:10.1016/j.icarus.2005.09.002

I.C.F. Müller-Wodarg, L. Moore, G. M., M. Mendillo, Magnetosphere–atmosphere coupling at Saturn: 1 – Response of thermosphere and ionosphere to steady state polar forcing. Icarus **221**(2) (2012). doi:10.1016/j.icarus.2012.08.034

R.L. Mutel, J.D. Menietti, D.A. Gurnett, W. Kurth, P. Schippers, C. Lynch, L. Lamy, C. Arridge, B. Cecconi, CMI growth rates for Saturnian kilometric radiation. Geophys. Res. Lett.

37, 19105 (2010). doi:10.1029/2010GL044940

A.F. Nagy, A.J. Kliore, E. Marouf, R. French, M. Flasar, N.J. Rappaport, A. Anabtawi, S.W. Asmar, D. Johnston, E. Barbinis, G. Goltz, D. Fleischman, First results from the ionospheric radio occultations of Saturn by the Cassini spacecraft. J. Geophys. Res. **111**, 6310 (2006). doi:10.1029/2005JA011519

A.F. Nagy, A.J. Kliore, M. Mendillo, S. Miller, L. Moore, J.I. Moses, I. Müller-Wodarg, D.E. Shemansky, Upper Atmosphere and Ionosphere of Saturn, in *Saturn from Cassini-Huygens*, ed. by Dougherty, M. K., Esposito, L. W., & Krimigis, S. M., 2009

N.F. Ness, M.H. Acuna, R.P. Lepping, J.E.P. Connerney, K.W. Behannon, L.F. Burlaga, F.M. Neubauer, Magnetic field studies by Voyager 1 - Preliminary results at Saturn. Science **212**, 211–217 (1981). doi:10.1126/science.212.4491.211

F.M. Neubauer, Nonlinear standing Alfven wave current system at Io - Theory. J. Geophys. Res. **85**, 1171–1178 (1980). doi:10.1029/JA085iA03p01171

J. Nichols, S. Cowley, Magnetosphere-ionosphere coupling currents in Jupiter's middle magnetosphere: effect of precipitation-induced enhancement of the ionospheric Pedersen conductivity. Ann. Geophys. **22**, 1799–1827 (2004). doi:10.5194/angeo-22-1799-2004

J.D. Nichols, Magnetosphere-ionosphere coupling at Jupiter-like exoplanets with internal plasma sources: implications for detectability of auroral radio emissions. MNRAS **414**, 2125–2138 (2011). doi:10.1111/j.1365-2966.2011.18528.x

J.D. Nichols, S.W.H. Cowley, Magnetosphere-ionosphere coupling currents in Jupiter's middle magnetosphere: dependence on the effective ionospheric Pedersen conductivity and iogenic plasma mass outflow rate. Ann. Geophys. **21**, 1419–1441 (2003). doi:10.5194/angeo-21-1419-2003

J.D. Nichols, S.W.H. Cowley, L. Lamy, Dawn-dusk oscillation of Saturn's conjugate auroral ovals. Geophys. Res. Lett. **372**, 24102 (2010). doi:10.1029/2010GL045818

J.D. Nichols, J.T. Clarke, J.C. Gérard, D. Grodent, Observations of Jovian polar auroral filaments. Geophys. Res. Lett. **36**(2009a). doi:10.1029/2009GL037578

J.D. Nichols, J.T. Clarke, J.C. Gérard, D. Grodent, K.C. Hansen, Variation of different components of Jupiter's auroral emission. J. Geophys. Res. **114**, 6210 (2009b). doi:10.1029/2009JA014051

J.D. Nichols, B. Cecconi, J.T. Clarke, S.W.H. Cowley, J.-C. Gérard, A. Grocott, D. Grodent, L. Lamy, P. Zarka, Variation of Saturn's UV aurora with SKR phase. Geophys. Res. Lett. **37** (2010). doi:10.1029/2010GL044057

J. O'Donoghue, T.S. Stallard, H. Melin, G.H. Jones, S.W.H. Cowley, S. Miller, K.H. Baines, J.S.D. Blake, The domination of Saturn's low-latitude ionosphere by ring 'rain'. Nature **496**(7444), 193–195 (2013). ISBN 0028-0836. http://dx.doi.org/10.1038/nature12049

J. O'Donoghue, T.S. Stallard, H. Melin, S.W.H. Cowley, S.V. Badman, L. Moore, S. Miller, C. Tao, K.H. Baines, J.S.D. Blake, Conjugate observations of Saturn's northern and southern H_3^+ aurorae. Icarus **229**, 214–220 (2014). doi:10.1016/j.icarus.2013.11.009

N. Ozak, D.R. Schultz, T.E. Cravens, V. Kharchenko, Y.-W. Hui, Auroral X-ray emission at Jupiter: Depth effects. J. Geophys. Res. **115**, 11306 (2010). doi:10.1029/2010JA015635

L. Pallier, R. Prangé, More about the structure of the high latitude Jovian aurorae. Planet. Space. Sci. **49**, 1159–1173 (2001). doi:10.1016/S0032-0633(01)00023-X

L. Pallier, R. Prangé, Detection of the southern counterpart of the Jovian northern polar cusp: Shared properties. Geophys. Res. Lett. **31**, 6701 (2004). doi:10.1029/2003GL018041

M. Panchenko, H. Rucker, W. Farrell, Periodic bursts of Jovian non-Io decametric radio emission. Planet. Space. Sci. **77**, 3–11 (2013)

J.D. Patterson, T.P. Armstrong, C.M. Laird, D.L. Detrick, A.T. Weatherwax, Correlation of solar energetic protons and polar cap absorption. J. Geophys. Res. **106**, 149–164 (2001). doi:10.1029/2000JA002006

J.J. Perry, Y.H. Kim, J.L. Fox, H.S. Porter, Chemistry of the Jovian auroral ionosphere. J. Geophys. Res. **104**, 16541–16566 (1999). doi:10.1029/1999JE900022

R. Prangé, D. Rego, J.-C. Gerard, Auroral Lyman alpha and H2 bands from the giant planets. 2: Effect of the anisotropy of the precipitating particles on the interpretation of the 'color ratio'. J. Geophys. Res. **100**, 7513–7521 (1995). doi:10.1029/94JE03176

R. Prangé, D. Rego, D. Southwood, P. Zarka, S. Miller, W. Ip, Rapid energy dissipation and variability of the lo-Jupiter electrodynamic circuit. Nature **379**, 323–325 (1996). doi:10.1038/379323a0

R. Prangé, L. Pallier, K.C. Hansen, R. Howard, A. Vourlidas, R. Courtin, C. Parkinson, An

interplanetary shock traced by planetary auroral storms from the Sun to Saturn. Nature **432**, 78–81 (2004). doi:10.1038/nature02986

W.R. Pryor, A.M. Rymer, D.G. Mitchell, T.W. Hill, D.T. Young, J. Saur, G.H. Jones, S. Jacobsen, S.W.H. Cowley, B.H. Mauk, A.J. Coates, J. Gustin, D. Grodent, J.-C. Gérard, L. Lamy, J.D. Nichols, S.M. Krimigis, L.W. Esposito, M.K. Dougherty, A.J. Jouchoux, A.I.F. Stewart, W.E. McClintock, G.M. Holsclaw, J.M. Ajello, J.E. Colwell, A.R. Hendrix, F.J. Crary, J.T. Clarke, X. Zhou, The auroral footprint of Enceladus on Saturn. Nature **472**, 331–333 (2011). doi:10.1038/nature09928

A. Radioti, D. Grodent, J.-C. Gérard, B. Bonfond, J.T. Clarke, Auroral polar dawn spots: Signatures of internally driven reconnection processes at Jupiter's magnetotail. Geophys. Res. Lett. **35**, 3104 (2008a). doi:10.1029/2007GL032460

A. Radioti, J.-C. Gérard, D. Grodent, B. Bonfond, N. Krupp, J. Woch, Discontinuity in Jupiter's main auroral oval. J. Geophys. Res. **113**, 1215 (2008b). doi:10.1029/2007JA012610

A. Radioti, D. Grodent, J.-C. Gérard, E. Roussos, C. Paranicas, B. Bonfond, D.G. Mitchell, N. Krupp, S. Krimigis, J.T. Clarke, Transient auroral features at Saturn: Signatures of energetic particle injections in the magnetosphere. J. Geophys. Res. **114**, 3210 (2009). doi:10.1029/2008JA013632

A. Radioti, D. Grodent, J.-C. Gérard, S.E. Milan, B. Bonfond, J. Gustin, W.R. Pryor, Bifurcations of the main auroral ring at Saturn: ionospheric signatures of consecutive reconnection events at the magnetopause. J. Geophys. Res. **116**(2011a). doi:10.1029/2011JA016661

A. Radioti, D. Grodent, J.-C. Gérard, M.F. Vogt, M. Lystrup, B. Bonfond, Nightside reconnection at Jupiter: Auroral and magnetic field observations from 26 July 1998. J. Geophys. Res. **116**, 3221 (2011b). doi:10.1029/2010JA016200

A. Radioti, M. Lystrup, B. Bonfond, J.-C. Gérard, Jupiter's aurora in ultraviolet and infrared: Simultaneous observations with the Hubble Space Telescope and the NASA Infrared Telescope Facility. J. Geophys. Res. **118**(5), 2286–2295 (2013a). doi:10.1002/jgra.50245

A. Radioti, E. Roussos, D. Grodent, J.-C. Gérard, N. Krupp, D.G. Mitchell, J. Gustin, B. Bonfond, W. Pryor, Signatures of magnetospheric injections in Saturn's aurora. J. Geophys. Res. **118**, 1922–1933 (2013b). doi:10.1002/jgra.50161

L.C. Ray, S. Hess, Modelling the Io-related DAM emission by modifying the beaming angle. J. Geophys. Res. **113**, 11218 (2008). doi:10.1029/2008JA013669

L.C. Ray, R.E. Ergun, P.A. Delamere, F. Bagenal, Magnetosphere-ionosphere coupling at Jupiter: Effect of field-aligned potentials on angular momentum transport. J. Geophys. Res. **115**, 9211 (2010). doi:10.1029/2010JA015423

L.C. Ray, M. Galand, L.E. Moore, B.L. Fleshman, Characterizing the limitations to the coupling between Saturn's ionosphere and middle magnetosphere. J. Geophys. Res. **117**, 7210 (2012a). doi:10.1029/2012JA017735

L.C. Ray, R.E. Ergun, P.A. Delamere, F. Bagenal, Magnetosphere-ionosphere coupling at Jupiter: A parameter space study. Journal of Geophysical Research (Space Physics) **117**, 1205 (2012b). doi:10.1029/2011JA016899

J.C. Raymond, X-rays from charge transfer in astrophysics: Overview. Astron. Nachr. **333**, 290 (2012). doi:10.1002/asna.201211677

E. Raynaud, E. Lellouch, J.-P. Maillard, G.R. Gladstone, J.H. Waite, B. Bézard, P. Drossart, T. Fouchet, Spectro-imaging observations of Jupiter's 2-μm auroral emission. I. $H_3{}^+$ distribution and temperature. Icarus **171**, 133–152 (2004). doi:10.1016/j.icarus.2004.04.020

M.H. Rees, *Physics and Chemistry of the Upper Atmosphere* (Cambridge Univ. Press, ???, 1989)

D. Rego, R. Prangé, L. Ben Jaffel, Auroral Lyman α and H_2 bands from the giant planets 3. Lyman α spectral profile including charge exchange and radiative transfer effects and H_2 color ratios. J. Geophys. Res. **104**, 5939–5954 (1999). doi:10.1029/1998JE900048

D. Rego, R. Prange, J.-C. Gerard, Auroral Lyman α and H_2 bands from the giant planets: 1. Excitation by proton precipitation in the Jovian atmosphere. J. Geophys. Res. **99**, 17075–17094 (1994). doi:10.1029/93JE03432

D. Rego, S. Miller, N. Achilleos, R. Prangé, R.D. Joseph, Latitudinal Profiles of the Jovian IR Emissions of H_3^+ at 4 μm with the NASA Infrared Telescope Facility: Energy Inputs and Thermal Balance. Icarus **147**, 366–385 (2000). doi:10.1006/icar.2000.6444

M.J. Reiner, J. Fainberg, R.G. Stone, Source characteristics of Jovian hectometric radio emissions. J. Geophys. Res. **98**, 18767–18777 (1993a). doi:10.1029/93JE01779

M.J. Reiner, J. Fainberg, R.G. Stone, M.L. Kaiser, M.D. Desch, R. Manning, P. Zarka, B.-M. Pedersen, Source characteristics of Jovian narrow-band kilometric radio emissions. J. Geophys. Res. **98**, 13163 (1993b). doi:10.1029/93JE00536

A. Roux, A. Hilgers, H. de Féraudy, D. Le Quéau, P. Louarn, S. Perraut, A. Bahnsen, M. Jespersen, E. Ungstrup, M. André, Auroral kilometric radiation sources - In situ and remote observations from Viking. J. Geophys. Res. **98**, 11657 (1993). doi:10.1029/92JA02309

H.O. Rucker, M. Panchenko, K.C. Hansen, U. Taubenschuss, M.Y. Boudjada, W.S. Kurth, M.K. Dougherty, J.T. Steinberg, P. Zarka, P.H.M. Galopeau, D.J. McComas, C.H. Barrow, Saturn kilometric radiation as a monitor for the solar wind? Adv. Space Res. **42**, 40–47 (2008). doi:10.1016/j.asr.2008.02.008

B.R. Sandel, D.E. Shemansky, A.L. Broadfoot, J.B. Holberg, G.R. Smith, J.C. McConnell, D.F. Strobel, S.K. Atreya, T.M. Donahue, H.W. Moos, D.M. Hunten, R.B. Pomphrey, S. Linick, Extreme ultraviolet observations from the Voyager 2 encounter with Saturn. Science **215**, 548–553 (1982). doi:10.1126/science.215.4532.548

T. Satoh, J.E.P. Connerney, Jupiter's H_3^+ Emissions Viewed in Corrected Jovimagnetic Coordinates. Icarus **141**, 236–252 (1999). doi:10.1006/icar.1999.6173

P. Schippers, C.S. Arridge, J.D. Menietti, D.A. Gurnett, L. Lamy, B. Cecconi, D.G. Mitchell, N. André, W.S. Kurth, S. Grimald, M.K. Dougherty, A.J. Coates, N. Krupp, D.T. Young, Auroral electron distributions within and close to the Saturn kilometric radiation source region. J. Geophys. Res. **116**, 05203 (2011). doi:10.1029/2011JA016461

L. Scurry, C.T. Russell, Proxy studies of energy transfer to the magnetosphere. J. Geophys. Res. **96**, 9541–9548 (1991). doi:10.1029/91JA00569

J.A. Simpson, J.D. Anglin, A. Balogh, J.R. Burrows, S.W.H. Cowley, P. Ferrando, B. Heber, R.J. Hynds, H. Kunow, R.G. Marsden, Energetic charged-particle phenomena in the Jovian magnetosphere - First results from the ULYSSES COSPIN collaboration. Science **257**, 1543–1550 (1992). doi:10.1126/science.257.5076.1543

R.P. Singhal, S.C. Chakravarty, A. Bhardwaj, B. Prasad, Energetic electron precipitation in Jupiter's upper atmosphere. J. Geophys. Res. **97**, 18245 (1992). doi:10.1029/92JE01894

E.C. Sittler, N. Andre, M. Blanc, M. Burger, R.E. Johnson, A. Coates, A. Rymer, D. Reisenfeld, M.F. Thomsen, A. Persoon, M. Dougherty, H.T. Smith, R.A. Baragiola, R.E. Hartle, D. Chornay, M.D. Shappirio, D. Simpson, D.J. McComas, D.T. Young, Ion and neutral sources and sinks within Saturn's inner magnetosphere: Cassini results. Planet. Space. Sci. **56**, 3–18 (2008). doi:10.1016/j.pss.2007.06.006

T.G. Slanger, T.E. Cravens, J. Crovisier, S. Miller, D.F. Strobel, Photoemission Phenomena in the Solar System. Space Sci. Rev. **139**, 267–310 (2008). doi:10.1007/s11214-008-9387-3

C.G.A. Smith, A.D. Aylward, Coupled rotational dynamics of Saturn's thermosphere and magnetosphere: a thermospheric modelling study. Ann. Geophys. **26**, 1007–1027 (2008). doi:10.5194/angeo-26-1007-2008

C.G.A. Smith, A.D. Aylward, Coupled rotational dynamics of Jupiter's thermosphere and magnetosphere. Ann. Geophys. **27**, 199–230 (2009). doi:10.5194/angeo-27-199-2009

C.G.A. Smith, S. Miller, A.D. Aylward, Magnetospheric energy inputs into the upper atmospheres of the giant planets. Ann. Geophys. **23**, 1943–1947 (2005). doi:10.5194/angeo-23-1943-2005

C.G.A. Smith, A.D. Aylward, G.H. Millward, S. Miller, L.E. Moore, An unexpected cooling effect in Saturn's upper atmosphere. Nature **445**, 399–401 (2007). doi:10.1038/nature05518

E.J. Smith, R.W. Fillius, J.H. Wolfe, Compression of Jupiter's magnetosphere by the solar wind. J. Geophys. Res. **83**, 4733–4742 (1978). doi:10.1029/JA083iA10p04733

H.T. Smith, R.E. Johnson, E.C. Sittler, M. Shappirio, D. Reisenfeld, O.J. Tucker, M. Burger, F.J. Crary, D.J. McComas, D.T. Young, Enceladus: The likely dominant nitrogen source in Saturn's magnetosphere. Icarus **188**, 356–366 (2007). doi:10.1016/j.icarus.2006.12.007

S.C. Solomon, Auroral electron transport using the Monte Carlo method. Geophys. Res. Lett. **20**, 185–188 (1993). doi:10.1029/93GL00081

S.C. Solomon, Auroral particle transport using Monte Carlo and hybrid methods. J. Geophys. Res. **106**, 107–116 (2001). doi:10.1029/2000JA002011

D.J. Southwood, M.G. Kivelson, The source of Saturn's periodic radio emission. J. Geophys. Res. **114**, 9201 (2009). doi:10.1029/2008JA013800

T.S. Stallard, S. Miller, S.W.H. Cowley, E.J. Bunce, Jupiter's polar ionospheric flows: Measured intensity and velocity variations poleward of the main auroral oval. Geophys. Res. Lett. **30**, 1221 (2003). doi:10.1029/2002GL016031

T.S. Stallard, H. Melin, S. Miller, S.V. Badman, R.H. Brown, K.H. Baines, Peak emission altitude of Saturn's H_3^+ aurora. Geophys. Res. Lett. **in press**(2012a). doi:10.1029/2012GL052806

T.S. Stallard, A. Masters, S. Miller, H. Melin, E.J. Bunce, C.S. Arridge, N. Achilleos, M.K. Dougherty, S.W.H. Cowley, Saturn's auroral/polar H_3^+ infrared emission: The effect of solar wind compression. J. Geophys. Res. **117**, 12302 (2012b). doi:10.1029/2012JA018201

T.S. Stallard, H. Melin, S. Miller, J. O'Donoghue, S.W.H. Cowley, S.V. Badman, A. Adriani, R.H. Brown, K.H. Baines, Temperature changes and energy inputs in giant planet atmospheres: what we are learning from H_3^+. Royal Soc. Phil. Trans. A **370**, 5213–5224 (2012c). doi:10.1098/rsta.2012.0028

T. Stallard, S. Miller, G.E. Ballester, D. Rego, R.D. Joseph, L.M. Trafton, The H_3^+ Latitudinal Profile of Saturn. Astrophys. J. Lett. **521**, 149–152 (1999). doi:10.1086/312189

T. Stallard, S. Miller, G. Millward, R.D. Joseph, On the Dynamics of the Jovian Ionosphere and Thermosphere. I. The Measurement of Ion Winds. Icarus **154**, 475–491 (2001). doi:10.1006/icar.2001.6681

T. Stallard, S. Miller, G. Millward, R.D. Joseph, On the Dynamics of the Jovian Ionosphere and Thermosphere. II. The Measurement of $H_3{}^+$ Vibrational Temperature, Column Density, and Total Emission. Icarus **156**, 498–514 (2002). doi:10.1006/icar.2001.6793

T. Stallard, C. Smith, S. Miller, H. Melin, M. Lystrup, A. Aylward, N. Achilleos, M.K. Dougherty, Saturn's auroral/polar H_3^+ infrared emission - II. A comparison with plasma flow models. Icarus **191**(2), 678–690 (2007a). doi:10.1016/j.icarus.2007.05.016

T. Stallard, S. Miller, H. Melin, M. Lystrup, M.K. Dougherty, N. Achilleos, Saturn's auroral/polar H_3^+ infrared emission I. General morphology and ion velocity structure. Icarus **189**(1), 1–13 (2007b). doi:10.1016/j.icarus.2006.12.027

T. Stallard, S. Miller, M. Lystrup, N. Achilleos, E.J. Bunce, C.S. Arridge, M.K. Dougherty, S.W.H. Cowley, S.V. Badman, D.L. Talboys, R.H. Brown, K.H. Baines, B.J. Buratti, R.N. Clark, C. Sotin, P.D. Nicholson, P. Drossart, Complex structure within Saturn's infrared aurora. Nature **456**(7219), 214–217 (2008). doi:10.1038/nature07440

T. Stallard, H. Melin, S.W.H. Cowley, S. Miller, M.B. Lystrup, Location and Magnetospheric Mapping of Saturn's Mid-latitude Infrared Auroral Oval. Astrophys. J. Lett. **722**, 85–89 (2010). doi:10.1088/2041-8205/722/1/L85

T. Stallard, S. Miller, H. Melin, M. Lystrup, S.W.H. Cowley, E.J. Bunce, N. Achilleos, M. Dougherty, Jovian-like aurorae on saturn. Nature **453**(7198), 1083–1085 (2008). doi:DOI 10.1038/nature07077

A.J. Steffl, P.A. Delamere, F. Bagenal, Cassini UVIS observations of the Io plasma torus. III. Observations of temporal and azimuthal variability. Icarus **180**, 124–140 (2006). doi:10.1016/j.icarus.2005.07.013

A.J. Steffl, P.A. Delamere, F. Bagenal, Cassini UVIS observations of the Io plasma torus. IV. Modeling temporal and azimuthal variability. Icarus **194**, 153–165 (2008). doi:10.1016/j.icarus.2007.09.019

R.G. Stone, B.M. Pedersen, C.C. Harvey, P. Canu, N. Cornilleau-Wehrlin, M.D. Desch, C. de Villedary, J. Fainberg, W.M. Farrell, K. Goetz, ULYSSES radio and plasma wave observations in the Jupiter environment. Science **257**, 1524–1531 (1992). doi:10.1126/science.257.5076.1524

C. Tao, S.V. Badman, M. Fujimoto, UV and IR auroral emission model for the outer planets: Jupiter and Saturn comparison. Icarus **213**, 581–592 (2011). doi:10.1016/j.icarus.2011.04.001

C. Tao, S.V. Badman, M. Fujimoto, Characteristic Time Scales of Uv and Ir Auroral Emissions at Jupiter and Saturn and Their Possible Observable Effects, in *Proc. of the 12th Symposium on Planetary Science* (TERRAPUB Japan, ???, 2013)

C. Tao, H. Fujiwara, Y. Kasaba, Neutral wind control of the Jovian magnetosphere-ionosphere current system. J. Geophys. Res. **114**, 8307 (2009). doi:10.1029/2008JA013966

C. Tao, H. Fujiwara, Y. Kasaba, Jovian magnetosphere-ionosphere current system characterized by diurnal variation of ionospheric conductance. Planet. Space. Sci. **58**, 351–364 (2010). doi:10.1016/j.pss.2009.10.005

C. Tao, S.V. Badman, T. Uno, M. Fujimoto, On the feasibility of characterising Jovian auroral electrons via H_3^+ infrared line emission analysis. Icarus **221**, 236–247 (2012). doi:10.1016/j.icarus.2012.07.015.

T. Terasawa, K. Maezawa, S. Machida, Solar wind effect on Jupiter's non-Io-related radio emission. Nature **273**, 131 (1978). doi:10.1038/273131a0

J.R. Thieman, M.L. Goldstein, Arcs in Saturn's radio spectra. Nature **292**, 728–731 (1981). doi:10.1038/292728a0

M.F. Thomsen, D.B. Reisenfeld, D.M. Delapp, R.L. Tokar, D.T. Young, F.J. Crary, E.C. Sittler, M.A. McGraw, J.D. Williams, Survey of ion plasma parameters in Saturn's magnetosphere. J. Geophys. Res. **115**, 10220 (2010). doi:10.1029/2010JA015267

A.T. Tomás, J. Woch, N. Krupp, A. Lagg, K.-H. Glassmeier, W.S. Kurth, Energetic electrons in the inner part of the Jovian magnetosphere and their relation to auroral emissions. J. Geophys. Res. **109**, 6203 (2004). doi:10.1029/2004JA010405

J.T. Trauger, J.T. Clarke, G.E. Ballester, R.W. Evans, C.J. Burrows, D. Crisp, J.S. Gallagher, R.E. Griffiths, J.J. Hester, J.G. Hoessel, J.A. Holtzman, J.E. Krist, J.R. Mould, R. Sahai, P.A. Scowen, K.R. Stapelfeldt, A.M. Watson, Saturn's hydrogen aurora: Wide field and planetary camera 2 imaging from the Hubble Space Telescope. J. Geophys. Res. **103**(E9), 20237–20244 (1998). doi:10.1029/98JE01324

R.A. Treumann, Planetary Radio Emission Mechanisms: a Tutorial, in *Radio astronomy at long wavelengths*, vol. 119, ed. by R.G. Stone, K.W. Weiler, M.L. Goldstein, J.-L. Bougeret (Washington DC American Geophysical Union Geophysical Monograph Series, ???, 2000)

R.A. Treumann, The electron-cyclotron maser for astrophysical application. Astron. Astrophys. Rev. **13**, 229–315 (2006). doi:10.1007/s00159-006-0001-y

A.R. Vasavada, A.H. Bouchez, A.P. Ingersoll, B. Little, C.D. Anger, Galileo SSI Team, Jupiter's visible aurora and Io footprint. J. Geophys. Res. **104**, 27133–27142 (1999). doi:10.1029/1999JE001055

V.M. Vasyliunas, Plasma Distribution and Flow, in *Physics of the Jovian Magnetosphere*, ed. by A.J. Dessler (Cambridge Univ. Press, ???, 1983), pp. 395–453

M.F. Vogt, M.G. Kivelson, K.K. Khurana, S.P. Joy, R.J. Walker, Reconnection and flows in the Jovian magnetotail as inferred from magnetometer observations. J. Geophys. Res. **115** (2010). doi:10.1029/2009JA015098

M.F. Vogt, M.G. Kivelson, K.K. Khurana, R.J. Walker, B. Bonfond, D. Grodent, A. Radioti, Improved mapping of Jupiter's auroral features to magnetospheric sources. J. Geophys. Res. **116**, 3220 (2011). doi:10.1029/2010JA016148

J.H. Waite Jr., The Ionosphere of Saturn, PhD thesis, Michigan Univ., Ann Arbor., 1981

J.H. Waite Jr., J.T. Clarke, T.E. Cravens, C.M. Hammond, The Jovian Aurora - Electron or ion precipitation? J. Geophys. Res. **93**, 7244–7250 (1988). doi:10.1029/JA093iA07p07244

J.H. Waite Jr., F. Bagenal, F. Seward, C. Na, G.R. Gladstone, T.E. Cravens, K.C. Hurley, J.T. Clarke, R. Elsner, S.A. Stern, ROSAT observations of the Jupiter aurora. J. Geophys. Res. **99**, 14799 (1994). doi:10.1029/94JA01005

J.H. Waite Jr., G.R. Gladstone, K. Franke, W.S. Lewis, A.C. Fabian, W.N. Brandt, C. Na, F. Haberl, J.T. Clarke, K.C. Hurley, M. Sommer, S. Bolton, ROSAT Observations of X-Ray Emissions from Jupiter During the Impact of Comet Shoemaker-Levy 9. Science **268**, 1598–1601 (1995). doi:10.1126/science.268.5217.1598

J.H. Waite Jr., W.S. Lewis, G.R. Gladstone, T.E. Cravens, A.N. Maurellis, P. Drossart, J.E.P. Connerney, S. Miller, H.A. Lam, Outer planet ionospheres - A review of recent research and a look toward the future. Adv. Space Res. **20**, 243 (1997). doi:10.1016/S0273-1177(97)00542-5

J.H. Waite, T.E. Cravens, J. Kozyra, A.F. Nagy, S.K. Atreya, R.H. Chen, Electron precipitation and related aeronomy of the Jovian thermosphere and ionosphere. J. Geophys. Res. **88**, 6143–6163 (1983). doi:10.1029/JA088iA08p06143

J.H. Waite, G.R. Gladstone, W.S. Lewis, P. Drossart, T.E. Cravens, A.N. Maurellis, B.H. Mauk, S. Miller, Equatorial X-ray emissions: Implications for Jupiter's high exospheric temperatures. Science **276**, 104–108 (1997). doi:10.1126/science.276.5309.104

J.H. Waite, G.R. Gladstone, W.S. Lewis, R. Goldstein, D.J. McComas, P. Riley, R.J. Walker, P. Robertson, S. Desai, J.T. Clarke, D.T. Young, An auroral flare at Jupiter. Nature **410**, 787–789 (2001)

R.J. Walker, C.T. Russell, Flux transfer events at the Jovian magnetopause. J. Geophys. Res. **90**, 7397–7404 (1985). doi:10.1029/JA090iA08p07397

J.W. Warwick, J.B. Pearce, D.R. Evans, T.D. Carr, J.J. Schauble, J.K. Alexander, M.L. Kaiser, M.D. Desch, M. Pedersen, A. Lecacheux, G. Daigne, A. Boischot, C.H. Barrow, Planetary radio astronomy observations from Voyager 1 near Saturn. Science **212**, 239–243 (1981). doi:10.1126/science.212.4491.239

J.W. Warwick, D.R. Evans, J.H. Romig, J.K. Alexander, M.D. Desch, M.L. Kaiser, M.G. Aubier, Y. Leblanc, A. Lecacheux, B.M. Pedersen, Planetary radio as-

tronomy observations from Voyager 2 near Saturn. Science **215**, 582–587 (1982). doi:10.1126/science.215.4532.582

R.J. Wilson, R.L. Tokar, M.G. Henderson, Thermal ion flow in Saturn's inner magnetosphere measured by the Cassini plasma spectrometer: A signature of the Enceladus torus? Geophys. Res. Lett. **36**, 23104 (2009). doi:10.1029/2009GL040225

J. Woch, N. Krupp, A. Lagg, B. Wilken, S. Livi, D.J. Williams, Quasi-periodic modulations of the Jovian magnetotail. Geophys. Res. Lett. **25**, 1253–1256 (1998). doi:10.1029/98GL00861

J. Woch, N. Krupp, A. Lagg, A. Tomás, The structure and dynamics of the Jovian energetic particle distribution. Adv. Space Res. **33**, 2030–2038 (2004). doi:10.1016/j.asr.2003.04.050

B.C. Wolven, P.D. Feldman, Self-absorption by vibrationally excited H_2 in the Astro-2 Hopkins Ultraviolet Telescope spectrum of the Jovian aurora. Geophys. Res. Lett. **25**, 1537–1540 (1998). doi:10.1029/98GL01063

C.S. Wu, Kinetic cyclotron and synchrotron maser instabilities - Radio emission processes by direct amplification of radiation. Space Sci. Rev. **41**, 215–298 (1985). doi:10.1007/BF00190653

C.S. Wu, L.C. Lee, A theory of the terrestrial kilometric radiation. Astrophys. J. **230**, 621–626 (1979). doi:10.1086/157120

R.V. Yelle, S. Miller, Jupiter's Thermosphere and Ionosphere, in *Jupiter. The Planet, Satellites and Magnetosphere*, ed. by F. Bagenal, T.E. Dowling, W.B. McKinnon, 2004, pp. 185–218

M. Yoneda, M. Kagitani, S. Okano, Short-term variability of Jupiter's extended sodium nebula. Icarus **204**(2), 589–596 (2009). doi:10.1016/j.icarus.2009.07.023

M. Yoneda, F. Tsuchiya, H. Misawa, B. Bonfond, C. Tao, M. Kagitani, S. Okano, Io's volcanism controls Jupiter's radio emissions. Geophys. Res. Lett. **40**(4), 671–675 (2013)

P. Zarka, On detection of radio bursts associated with Jovian and Saturnian lightning. Astron. Astrophys. **146**, 15–18 (1985)

P. Zarka, The auroral radio emissions from planetary magnetospheres - What do we know, what don't we know, what do we learn from them? Adv. Space Res. **12**, 99–115 (1992). doi:10.1016/0273-1177(92)90383-9

P. Zarka, Auroral radio emissions at the outer planets: Observations and theories. J. Geophys. Res. **103**, 20159–20194 (1998). doi:10.1029/98JE01323

P. Zarka, Radio and plasma waves at the outer planets. Adv. Space Res. **33**, 2045–2060 (2004). doi:10.1016/j.asr.2003.07.055

P. Zarka, Plasma interactions of exoplanets with their parent star and associated radio emissions. Planet. Space. Sci. **55**, 598–617 (2007). doi:10.1016/j.pss.2006.05.045

P. Zarka, F. Genova, Low-frequency Jovian emission and solar wind magnetic sector structure. Nature **306**, 767–768 (1983). doi:10.1038/306767a0

P. Zarka, T. Farges, B.P. Ryabov, M. Abada-Simon, L. Denis, A scenario for Jovian S-bursts. Geophys. Res. Lett. **23**, 125–128 (1996). doi:10.1029/95GL03780

P. Zarka, L. Lamy, B. Cecconi, R. Prangé, H.O. Rucker, Modulation of Saturn's radio clock by solar wind speed. Nature **450**, 265–267 (2007). doi:10.1038/nature06237

B. Zieger, K.C. Hansen, Statistical validation of a solar wind propagation model from 1 to 10 au. Journal of Geophysical Research-Space Physics **113**(A8) (2008). doi:DOI 10.1029/2008JA013046